APPLICATIONS OF SOLID-STATE NMR TO NEW MATERIALS

LYNDSEY KNIGHT, MChem

Thesis submitted to the University of Nottingham

for the degree of Doctor of Philosophy

JULY 2017

Abstract

The domain sizes of a range of diblock polymers have been measured using solid-state NMR spin diffusion experiments carried out under fast magic angle spinning (MAS). ^{1}H-^{1}H exchange spectra were acquired at a range of mixing times and the results displayed effects due to both intra-domain and inter-domain spin diffusion. By fitting the data to an initial rate approximation domain sizes and spin diffusion coefficients were calculated. Simulations were also carried out to determine the impact of T_1 relaxation during the experimental mixing time.

The spin diffusion coefficient of polystyrene has also been studied under a variety of different conditions. Increasing MAS rate caused a decrease in the spin diffusion coefficient and at the fastest spinning speeds the rate of spin diffusion was much reduced. Temperature changes were shown to have little effect on the spin diffusion coefficient. The incorporation of recoupling sequences into the experimental mixing time was also studied.

Solid-state NMR was also used to study a selection of hydroxyapatite nanoparticle/organic dispersant molecule composite materials with potential biomedical applications. ^{1}H-^{31}P correlation experiments were used to investigate the interaction between the dispersant molecules and the surface of hydroxyapatite nanoparticles. The spectra suggested that the dispersant molecules containing polylactic acid interacted with the surface of the nanoparticle via the polymer chain. Whereas dispersant molecules with an aliphatic chain appeared to interact with the particle via their head group. The results from DNP spectra, which selectively enhanced the surface regions, also supported this conclusion.

Acknowledgements

Firstly, I would like to thank my supervisor Dr Jeremy Titman for his constant support and guidance throughout my PhD. He has always been available to help with all the problems that I encountered during my studies (from practical issues to questions about underlying theory) and without him this work would not have been possible. I have enjoyed and benefited from the time I have spent in the solid-state NMR group at the University of Nottingham and I believe this is due, in no small part, to my supervisor.

I would also like to acknowledge the assistance of Dr Huw Williams the NMR facility manager at the University of Nottingham for help with many practical NMR problems and useful discussions. I am also grateful to Dr Subhradip Paul the DNP facility manager for his assistance in acquiring the DNP spectra.

I am grateful to the EPSRC for providing funding for this work and to the University of Nottingham for permitting me to study for a PhD.

A massive thank you is due to all the members of the solid-state NMR group at Nottingham, including both postgraduate students and undergraduate project students. These people are, Dr David Bennett, Dr Gregory Martin, Dr Habeeba Miah, Rosalie Cresswell, Marco Mais, Gavin Bell, Steven Ensinger, Edward Rayner, Emily Hetherington, Genevieve Hodgins and Martin Pringle. Each one of them helped to make the solid-state NMR group a great place to work.

I would like to acknowledge the contribution made by Gavin Bell, who first started work looking at solid-state NMR of diblock polymers. Special thanks

are also due to Dr Habeeba Miah for looking after me so very much when I first started my PhD, for all her help with IT issues, including teaching me how to use Matlab and for shamelessly encouraging all the arrowwords. I would also like to thank Rosalie Cresswell for maths assistance and cupcakes.

I also wish to thank all the people at Nottingham University who made my time there memorable. In particular, I am grateful to Susan Bamford and all the members of 'electrochemistry and friends' for all the coffee and the very interesting discussions.

I am also grateful for the help of my mother, Jacqueline Gregory and my husband, Gareth Wood for taking the time to proofread this thesis. Finally, and most importantly, I would like to thank all of my family and friends who have supported me and cared for me throughout my life.

Contents

Abstract i

Acknowledgements ii

1 Introduction 1

2 Theory 4

2.1 The Spin System 4

2.1.1 The Density Operator 6

2.2 NMR Hamiltonians 9

2.2.1 Zeeman Hamiltonian 10

2.2.2 Chemical Shift Hamiltonian 12

2.2.3 Dipolar Coupling Hamiltonian 16

2.2.4 Quadrupolar Hamiltonian 22

2.2.5 J-Coupling Hamiltonian 23

2.2.6 Radiofrequency Hamiltonian 23

2.3 The Density Operator at Thermal Equilibrium 25

2.4 The NMR Experiment 27

3 Solid-State NMR Methods 31

3.1 Magic Angle Spinning 31

3.2 Decoupling 34

3.3 Cross Polarisation 40
3.3.1 Lee-Goldburg Cross Polarisation 43
3.4 Recoupling Sequences 43
3.5 Dynamic Nuclear Polarisation 45

4 Spin Diffusion and Domain Sizes in Polymers 49
4.1 The Initial Rate Approximation 53
4.2 Domain Sizes of Diblock Polymers 56
4.2.1 Materials 56
4.2.2 Experimental Method 61
4.2.3 Results and Discussion 63
4.3 T_1 Relaxation in Spin Diffusion Experiments 73
4.3.1 Simulation of Spin Diffusion Profiles 77
4.3.2 Results from Simulated Diffusion Profiles 83
4.4 Conclusions 88

5 Spin Diffusion Coefficient of Polystyrene 89
5.1 Experimental Method 89
5.2 Temperature Calibration of the 1.3 mm Probe 91
5.3 Results and Discussion 97
5.4 Conclusions 109

6 Hydroxyapatite Nanoparticles 110
6.1 Materials 111
6.2 Experimental Set-up 115
6.3 Results and Discussion 116
6.4 DNP Experiments 127
6.4.1 Experimental Method 128
6.4.2 Results 129

6.5 Conclusions 135

7 Summary and Outlook **137**

Bibliography **142**

Appendix A **152**

Appendix B **160**

List of Figures

2.1 A selection of simulated ^{207}Pb CSA patterns. 14

2.2 The polar angles θ and ϕ show the orientation of the B_0 field in the principal axis frame of the chemical shift tensor. 15

2.3 The angles θ and ϕ describe the orientation of the internuclear vector between spins I and S, separated by distance r, with respect to the B_0 field 17

2.4 NMR transitions for dipolar coupled spins. 19

2.5 Pake pattern produced by simulating the heteronuclear dipolar coupling between a ^{13}C and a ^{1}H nucleus in a powder sample. . 20

3.1 In a Magic Angle Spinning experiment the sample is spun rapidly around an axis inclined at $\theta_R = 54.74°$ away from the B_0 field. 32

3.2 Pulse sequence using DUMBO-1 to correlate a high resolution dimension with a MAS dimension. 37

3.3 ^{1}H-^{1}H spectrum of an hydroxyapatite/polylactic acid composite nanomaterial correlating a MAS dimension with a high resolution DUMBO-1 dimenison. Unscaled. 39

3.4 ^{1}H-^{1}H spectra of an hydroxyapatite/polylactic acid composite nanomaterial correlating a MAS dimension with a high resolution DUMBO-1 dimenison. Scaled. 39

3.5 The pulse sequence for a CP experiment used to transfer polarisation from a proton nucleus to a heteronucleus (X). 41

3.6 Structure of the DNP polarising agent AMUPol. 47

3.7 Energy level diagrams showing how polarisation transfer can be achieved using the cross effect. 48

4.1 TEM images of PMMA-b-PS samples 1A and 1F. 58

4.2 Morphologies observed in the diblock polymers. 58

4.3 TEM images of PMMA-b-PBzMA sample 2B. 60

4.4 Phase diagrams constructed on the basis of TEM images for the PMMA-b-PBzMA polymers (left) and PMMA-b-PS samples (right). 60

4.5 ^{1}H-^{1}H spin diffusion spectra of sample 1B recorded with mixing times of 0.0025 s (top), 0.025 s (centre) and 0.2 s (bottom). . . . 64

4.6 ^{1}H NMR spectrum of sample 1B with four fitted mixed Gaussian/Lorentzian peaks. 65

4.7 Decay of intensity of the diagonal aromatic peak of sample 1B with increasing mixing time. 66

4.8 Decay of intensity of the diagonal methoxy peak of sample 1B with increasing mixing time. 66

4.9 ^{1}H-^{1}H spin diffusion spectra of sample 2B recorded with mixing times of 0.0025 s (top), 0.025 s (centre) and 0.2 s (bottom). . . . 70

4.10 Decay of intensity of the diagonal aromatic peak of sample 2B with increasing mixing time 71

4.11 Decay of intensity of the diagonal aromatic peak of sample 2F with increasing mixing time. 72

4.12 Diagram showing the transfer of magnetisation in a one dimensional sheet with a magnetisation gradient 78

4.13 Diagram illustrating the operation of the simulation. 81

4.14 Simulated diffusion profiles for a lamellar PMMA-b-PS diblock polymer with the magnetisation starting in the PS domain. . . . 84

4.15 Simulated diffusion profiles for a lamellar PMMA-b-PS diblock polymer with the magnetisation starting in the PMMA domain. 84

4.16 Experimental data showing the intensity build-up of the cross-peak of sample 1A and four simulated fits. 87

4.17 Experimental data showing the intensity build-up of the cross-peak of sample 1E and five simulated fits. 87

5.1 Static spectrum of lead nitrate recorded with the VT gas temperature set to 288 K and the simulated fit to the spectrum . . 94

5.2 Plot showing the variation of the chemical shift of lead nitrate with changing temperature. 94

5.3 MAS spectra of lead nitrate recorded with increasing spinning speed at a constant VT gas temperature of 298 K. 95

5.4 Plot of the actual sample temperature with increasing MAS rate when the VT gas temperature was set to 298 K 95

5.5 Plot of the spectrometer VT gas temperature against the actual sample temperature 96

5.6 ^{1}H-^{1}H spin diffusion spectra of polystyrene recorded with mixing times of 0.002 s (left) and 0.02 s (right) 97

5.7 Diffusion profiles of the polystyrene cross peak intensity with increasing mixing time for a range of MAS rates. 98

5.8 Plot of the polystyrene spin diffusion coefficient with increasing MAS rate. 98

5.9 A single repeating unit of polystyrene 102

5.10 Spin diffusion coefficient of polystyrene. 104

5.11 Plot of the polystyrene spin diffusion coefficient recorded at 60 kHz MAS with increasing sample temperature 104

5.12 The build-up of polystyrene cross peak intensity with increasing mixing time obtained from spectra recorded using RFDR (blue), the $SR6_6^2$ sequence (cyan) and without recoupling (red). 108

5.13 Plot of the polystyrene spin diffusion coefficient with increasing MAS rate. 108

6.1 Structures of the dispersant molecules used to coat the surface of the nanoparticles. 112

6.2 SEM image of the uncoated HAp nanoparticles. 113

6.3 Pulse sequence used to acquire the ^{1}H-^{31}P correlation spectra. . 116

6.4 ^{1}H spectrum of the HAp nanoparticles. 118

6.5 ^{1}H-^{31}P correlation spectrum of the HAp nanoparticles. 119

6.6 ^{1}H-^{31}P correlation spectrum of HAp/[PLA]-[COONa]. 121

6.7 ^{1}H-^{31}P correlation spectrum of HAp/[PLA]-[$C_6H_9O_4$]. 121

6.8 ^{1}H-^{31}P correlation spectrum of HAp/[$C_{12}H_{23}$]-[$C_2H_3(COOH)_2$]. . 123

6.9 ^{1}H-^{31}P correlation spectrum of HAp/[$C_{11}H_{23}$]-[$C_7H_9O_5$]. 123

6.10 Diagram displaying the possible modes of binding of the dispersant molecule to the surface hydroxyapatite nanoparticle 124

6.11 ^{1}H-^{31}P correlation spectrum of HAp/[PLA_{ex}]-[$C_6H_9O_4$]. 126

6.12 ^{1}H spectrum of HAp/[PLA_{ex}]-[$C_6H_9O_4$]. 126

6.13 Pulse sequence used to acquire the DNP enhanced ^{1}H-^{31}P correlation spectra. 129

6.14 ^{1}H spectra of the HAp/[PLA]-[$C_6H_9O_4$] sample recorded with the microwaves off (blue) and the microwaves on (red) 131

6.15 ^{31}P spectra of the HAp/[PLA]-[$C_6H_9O_4$] sample recorded with the microwaves off (blue) and the microwaves on (red) 131

6.16 DNP correlation spectrum of HAp/[PLA]-[$C_6H_9O_4$]. 133

6.17 DNP correlation spectrum of HAp/[$C_{12}H_{23}$]-[$C_2H_3(COOH)_2$]. . . 133

List of Tables

4.1 Data supplied for PMMA-b-PS polymers. 57

4.2 Data supplied for PMMA-b-PBzMA polymers. 57

4.3 Characteristic distances of polymer repeating units. 62

4.4 Table showing the diffusion coefficients and domain sizes of all the PMMA-b-PS diblock polymers. 68

4.5 Table showing the domain sizes of all the PMMA-b-PBzMA diblock polymers. 68

4.6 PMMA-b-PS domain sizes calculated using the decay of the PS aromatic peak, the PMMA methoxy peak and the average of these two results. 75

4.7 Domain sizes obtained through back-correction of the decay of the PMMA methoxy peak and the PS aromatic peak using a sample average T_1 value. 76

4.8 Domain sizes obtained through back-correction of the decay of the PMMA methoxy peak and the PS aromatic peak using the T_1 values of the homopolymers. 76

5.1 Table showing isotropic shift, CSA and asymmetry obtained from fits to the static spectra of lead nitrate recorded at different temperatures. 93

5.2 Table showing the proton-proton distances in a repeating unit of polystyrene 102
5.3 Table of the proton second moments and proton linewidths . . . 103
5.4 Table showing the calculated spin diffusion coefficients of polystyrene at different MAS rates. 106

6.1 Properties of the different dispersant molecules used to coat the surface of the HAp nanoparticles 113
6.2 Table showing the approximate weight of the polymer as a % of the total weight of the sample. 114

Chapter 1

Introduction

Nuclear Magnetic Resonance (NMR) is an analytical technique, frequently applied to study matter across a wide range of fields including physics, chemistry, biochemistry and medicine. The magnetic properties of certain nuclei are exploited during the course of an NMR experiment in order to interrogate the sample's molecular structure. When placed in an external magnetic field these magnetically active nuclei generate a bulk polarisation, which can be manipulated using radiofrequency (rf) pulses. After application of rf irradiation, the subsequent return of the bulk polarisation to its equilibrium state can be measured and analysed to reveal information about the local environment of the nuclei under study.

The first reported NMR experiments were carried out in the late 1940s by Purcell, Torrey and Pound[1] and concurrently and independently by Bloch, Hansen and Packard[2]. Purcell and co-workers studied the absorption of rf irradiation by a solid sample of paraffin, whereas Bloch et al. recorded an NMR signal from a sample of liquid water. In recognition of their efforts Bloch and Purcell were awarded the 1952 Nobel prize in physics.

Over the sixty years since its discovery the field of NMR spectroscopy underwent vast expansion, with some of the key milestones including the introduction of Fourier Transform NMR[3] and the development of multidimensional NMR experiments[4]. In particular, solution-state NMR developed rapidly, becoming a standard analytical tool used for structural elucidation of organic molecules. A comprehensive review of the development of NMR spectroscopy can be found in the Encyclopedia of Magnetic Resonance, Volume 1[5].

In spite of the fact that one of the initial NMR experiments was carried out on a block of paraffin, solid-state NMR was actually much slower to gain prominence than its solution-state counterpart. This was primarily due to the presence of various anisotropic interactions (which vary in strength depending on the molecular orientation). In solution rapid molecular tumbling averages these interactions to a single value, typically resulting in NMR spectra with narrow, well-resolved peaks. Alternatively, in solids, little averaging takes place as molecular motion is usually restricted and spectra recorded without the use of additional experimental techniques tend to be broad and featureless.

One of principal experimental breakthroughs in the field of solid-state NMR was the invention of Magic Angle Spinning (MAS) in the late 1950s[6;7], which can be used to mitigate some of the effects of these anisotropic interactions. Subsequently, many successful experiments have been developed to study a diverse range of solid materials with examples including proteins, ionic conductors, hydrogen storage materials, polymers and catalysts. The application of solid-state NMR is critical if the samples are not available in a suitable solution-state form, are intended for use in the solid-state or have properties of interest in the solid phase. Solid-state NMR can also be used to access alternative information to solution-state studies because the previously mentioned

anisotropic interactions may be exploited and analysed during the course of appropriately designed experiments. In this thesis the application of solid-state NMR to study a variety of new materials is described.

Chapter 2 contains a brief description of the theory underpinning the basic NMR experiment and describes some of the nuclear spin interactions of most relevance to the work carried out in this thesis. Some essential solid-state NMR techniques used to acquire the experimental results are described in detail in Chapter 3. This chapter also introduces the technique of dynamic nuclear polarisation (DNP) which can be used to enhance signal intensity in NMR spectra.

Chapter 4 describes the use of spin diffusion NMR experiments with fast MAS to extract spin diffusion coefficients and measure the domain sizes of a range of diblock polymers. Simulation of the spin diffusion process for a lamellar system was also carried out. Following on from this work, Chapter 5 involves a detailed investigation into the rate of spin diffusion using a sample of polystyrene (PS). Variation of the PS spin diffusion coefficient at different MAS rates, temperatures and under application of different recoupling sequences was studied.

Chapter 6 details the investigations carried out on a range of hydroxyapatite nanoparticle composite materials with different surface bound short chain dispersant molecules. The mode of attachment of the polymer to the hydroxyapatite surface was studied using proton-phosphorous heteronuclear correlation spectroscopy. Further insight into changes occurring at the surface of the samples was also gained by use of DNP.

Chapter 2

Theory

This chapter intends to provide an introduction to some of the theoretical aspects of NMR that relate to this work. For further details of the theory and application of NMR a variety of textbooks may be consulted[8–10].

2.1 The Spin System

All NMR active nuclei have spin angular momentum (defined by the quantum number - I) and an associated magnetic moment (μ). These two properties of the nucleus are related by a constant of proportionality, known as the magnetogyric ratio (γ), which may be positive or negative depending on the relative alignment of the magnetic moment and the spin angular momentum.

$$\mu = \gamma I. \tag{2.1}$$

According to quantum mechanics, a nucleus with spin quantum number I possesses 2I+1 eigenstates of spin angular momentum, defined by a second quantum number (m_I), taking values from -I to +I. The wavefunction for such a nucleus can be written as a superposition of these states. For example, a

$I = \frac{1}{2}$ nucleus has two eigenstates $|I, m_I >= |\frac{1}{2}, \frac{1}{2} >$ and $|\frac{1}{2}, -\frac{1}{2} >$, otherwise written as $|\alpha >$ and $|\beta >$. The general form of the wavefunction describing this spin state can therefore be written as

$$|\Psi >= c_\alpha|\alpha > + c_\beta|\beta > . \tag{2.2}$$

The superposition coefficients, c_α and c_β, are complex numbers that relate to the probability of the system occupying that state. It is possible to express the wavefunction given above and its complex conjugate ($< \Psi|$) as a column and a row vector

$$|\Psi >= \begin{pmatrix} c_\alpha \\ \\ c_\beta \end{pmatrix} \qquad \text{and} \qquad < \Psi| = \begin{pmatrix} c_\alpha^* & c_\beta^* \end{pmatrix}. \tag{2.3}$$

The result of an NMR measurement depends on what happens to the nuclear spins over the course of that experiment. So, if we wish to understand and predict the outcome of NMR experiments, we need a method of tracking the time evolution of the nuclear spins. The time dependent Schrodinger equation, (given in Equation 2.4), is used to describe how the quantum state of a physical system evolves in time. $\hat{H}$ is the Hamiltonian operator that corresponds to the total energy of the system and $\hbar$ is the reduced Planck constant.

$$i\hbar\frac{\delta|\Psi(t) >}{\delta t} = \hat{H}|\Psi(t) > \tag{2.4}$$

Theoretically, it should be possible to use the Schrodinger equation to calculate the evolution of each individual spin in the sample and sum all the separate contributions in order to calculate the expected outcome. However, given the considerable quantity of nuclear spins present within a normal NMR sample this is not a very practical approach to the problem.

2.1.1 The Density Operator

The density operator method provides a solution to this issue by using a matrix (the density matrix) to represent the ensemble averaged state of the entire spin system. The formation of this matrix is based on the quantum mechanical approach to calculating an expectation value of an observable. The expectation value ($< \hat{Q} >$) is given as

$$< \hat{Q} > = < \Psi | \hat{Q} | \Psi > \tag{2.5}$$

where $\hat{Q}$ is the operator that corresponds to the observable, Q. Matrix representations of operators used in the theory of NMR are frequently formed using the eigenstates $|I, m_I >$ of spin angular momentum as the basis set. In this basis each element, $Q_{m'_I m_I}$, of the matrix $\hat{Q}$ is obtained from evaluation of $< I, m'_I | \hat{Q} | I, m_I >$.

Therefore, for an I= $\frac{1}{2}$ nucleus the expectation value can be calculated as

$$< \hat{Q} > = \begin{pmatrix} c^*_\alpha & c^*_\beta \end{pmatrix} \begin{pmatrix} \hat{Q}_{\alpha\alpha} & \hat{Q}_{\alpha\beta} \\ \hat{Q}_{\beta\alpha} & \hat{Q}_{\beta\beta} \end{pmatrix} \begin{pmatrix} c_\alpha \\ c_\beta \end{pmatrix} \tag{2.6}$$

$$< \hat{Q} > = c^*_\alpha c_\alpha \hat{Q}_{\alpha\alpha} + c^*_\alpha c_\beta \hat{Q}_{\alpha\beta} + c_\beta c^*_\alpha \hat{Q}_{\beta\alpha} + c_\beta c^*_\beta \hat{Q}_{\beta\beta}. \tag{2.7}$$

Equation 2.7 involves the products of the superposition coefficients. An alternative method of obtaining these coefficients involves forming the matrix of $|\Psi >< \Psi|$.

$$|\Psi >< \Psi| = \begin{pmatrix} c_\alpha \\ c_\beta \end{pmatrix} \begin{pmatrix} c^*_\alpha & c^*_\beta \end{pmatrix} = \begin{pmatrix} c_\alpha c^*_\alpha & c_\alpha c^*_\beta \\ c_\beta c^*_\alpha & c_\beta c^*_\beta \end{pmatrix} \tag{2.8}$$

The expectation value may then be obtained from $|\Psi >< \Psi|$ using the following

equation.

$$< \hat{Q} > = Tr\Big(|\Psi >< \Psi|\hat{Q}\Big) \tag{2.9}$$

This equation defines the expectation value of a system consisting of a single nucleus. However, a similar equation can be used to predict the expectation value of a large number (**N**) of nuclear spins

$$< \hat{Q} >= Tr\Big(\big(\sum_{n}^{N} |\Psi_n >< \Psi_n|\big)\hat{Q}\Big). \tag{2.10}$$

A density operator $\hat{\rho}$ may then be defined as

$$\hat{\rho} = \mathbf{N}^{-1} \sum_{n}^{N} |\Psi_n >< \Psi_n| = \begin{pmatrix} \overline{c_\alpha c_\alpha^*} & \overline{c_\alpha c_\beta^*} \\ \overline{c_\beta c_\alpha^*} & \overline{c_\beta c_\beta^*} \end{pmatrix}, \tag{2.11}$$

where the overbar indicates an average. The diagonal elements of this matrix are the populations of the states and the off-diagonal elements are the coherences between them.

The result of any macroscopic observation can now be predicted using Equation 2.12 which involves the multiplication of a density matrix ($\hat{\rho}$), representing the state of the entire spin system, with the matrix representation of the operator for the observable that is being measured ($\hat{Q}$).

$$< \hat{Q} > = \mathbf{N} Tr(\hat{\rho}\hat{Q}) \tag{2.12}$$

The use of the density matrix as a convenient representation of the entire state of the spin system necessitates a method of tracking its time evolution. The time dependent Schrodinger equation (see Equation 2.4), which describes how the wavefunction evolves in time, can be adapted for use with the density

matrix. This results in the Louiville-von Neumann equation which is shown below*

$$\frac{\delta\hat{\rho}}{\delta t} = -i\hbar[\hat{H}(t), \hat{\rho}(t)] \tag{2.14}$$

Equation 2.15 shows the solution of Louiville-von Neumann in the case of a time-independent Hamiltonian operator

$$\hat{\rho}(t) = e^{-i\hat{H}t}\hat{\rho}(0)e^{i\hat{H}t}. \tag{2.15}$$

In the case of a time-dependent Hamiltonian this solution is re-written as

$$\hat{\rho}(t) = \hat{T}e^{-i\int_0^t \hat{H}(t').dt'}\hat{\rho}(0)e^{i\int_0^t \hat{H}(t').dt'}. \tag{2.16}$$

Where $\hat{T}$ is the Dyson time ordering operator that ensures that the Hamiltonians are applied in their correct time order. One way of dealing with the integral in Equation 2.16 is to approximate it as a product (see Equation 2.17). This approach is used in many solid-state NMR simulation programs such as SIMPSON[11] and it involves dividing the time-dependent Hamiltonian into very small time-intervals Δt over which the Hamiltonian is assumed to be time independent

$$e^{i\int_0^t \hat{H}(t').dt'} = \prod_{n=0}^{n=t/\Delta t} e^{i\hat{H}(t_n)\Delta t}. \tag{2.17}$$

Whichever solution to the Louiville-von Neumann equation is used two pieces of information are required in order to calculate the density matrix that represents the state of the system at a particular time $\hat{\rho}(t)$. Firstly, we need to know the initial state of the spin system and secondly we need to know the

*The commutator of two operators $\hat{A}$ and $\hat{B}$ is shown below

$$[\hat{A}, \hat{B}] = \hat{A}\hat{B} - \hat{B}\hat{A}. \tag{2.13}$$

If two operators commute $[\hat{A}, \hat{B}] = 0$.

Hamiltonian that is active during the time period that elapses between the initial and final states of the density matrix. The following section contains a description of the Hamiltonians for the various interactions that may affect the outcome of an NMR experiment and the subsequent section contains a description of how an appropriate starting point for the density matrix can be obtained.

2.2 NMR Hamiltonians

The Hamiltonian is the operator that corresponds to the total energy of the system and in a typical sample this would include the interactions between all of the nuclei and all of the electrons. This is a vast quantity of information that tends to result in impossibly large calculations. Fortunately, in NMR it is possible to make a simplification known as the spin Hamiltonian hypothesis which allows us to work with Hamiltonians that only describe the nuclear spin interactions. This is permissible because the interactions of the electrons evolve on a much faster timescale than the nuclear spin interactions. This means the nuclei only experience the time averaged contribution of these interactions and they can be incorporated into the nuclear spin Hamiltonians as constants.

All the Hamiltonians that describe the NMR interactions contain nuclear spin angular momentum operators. These are used to extract information about the nuclear spin angular momentum from the wavefunction. Three operators, $\hat{I}_x, \hat{I}_y$ and $\hat{I}_z$, are used to describe the spin angular momentum around the three Cartesian axes. The $\hat{I}_z$ operator has the following effect on the nuclear spin states.

$$\hat{I}_z|I, m_I >= m_I|I, m_I > \tag{2.18}$$

It can often be convenient to express the $\hat{I}_x$ and $\hat{I}_y$ in terms of a raising ($\hat{I}_+$)

and a lowering ($\hat{I}_-$) operator defined below.

$$\hat{I}_+ = \hat{I}_x + i\hat{I}_y \qquad \hat{I}_- = \hat{I}_x - i\hat{I}_y \tag{2.19}$$

The effect of the raising operator when applied to a nuclear spin state is to increase its m_I value by one whereas the lowering operator would decrease the m_I value of a state by one. Attempting to apply the raising operator to a spin state with the maximum m_I value or the lowering operator to a state with the minimum value would fail.

The total nuclear spin Hamiltonian can be represented as a sum of the Hamiltonians for the various interactions

$$\hat{H} = \hat{H}_Z + \hat{H}_{CS} + \hat{H}_{DD} + \hat{H}_Q + \hat{H}_J + \hat{H}_{RF}. \tag{2.20}$$

$\hat{H}_Z$ is the Hamiltonian for the Zeeman interaction, $\hat{H}_{CS}$ is the chemical shift Hamiltonian, $\hat{H}_{DD}$ is the Hamiltonian for the nuclear dipole-dipole interaction, $\hat{H}_Q$ is the Hamiltonian for the quadrupolar interaction, $\hat{H}_J$ is the Hamiltonian for indirect J-coupling and $\hat{H}_{RF}$ is the Hamiltonian describing the interaction of the nuclear spins with an applied radiofrequency field. These Hamiltonians will now be described in more detail.

2.2.1 Zeeman Hamiltonian

The Zeeman effect describes the interaction of the nuclear magnetic moment with a static, external magnetic field, which results in the splitting of the 2I+1 levels. The Hamiltonian for this interaction, assuming that the external

magnetic field is applied along the z axis, is shown below

$$\hat{H}_Z = -\hat{\mu}_z B_0 = -\gamma \hat{I}_z B_0 = \omega_0 \hat{I}_z. \tag{2.21}$$

The frequency ω_0 is known as the Larmor frequency ($\omega_0 = -\gamma B_0$). The energies of the Zeeman eigenstates in the presence of the magnetic field are given as $\omega_{m_I} = m_I \omega_0$. This result can be obtained by solving the time independent Schrodinger equation ($\hat{H}_Z|\Psi >= E|\Psi >$) using the Hamiltonian given above and Equation 2.18.

The Zeeman interaction is typically the dominant interaction in an NMR experiment (when working at high field in the absence of nuclei with very large quadrupolar moments). This allows us to make a further simplification to the other interaction Hamiltonians, called the secular approximation. The secular approximation involves splitting the Hamiltonian up into a part that commutes with the Zeeman Hamiltonian called the secular component and a part that does not commute, called the non-secular component.

$$\hat{H}_{int} = \hat{H}_{sec} + \hat{H}_{non-sec} \tag{2.22}$$

When the Zeeman interaction is large the non-secular component of the Hamiltonian can be discarded and only the effect of the secular component needs to be considered. In terms of the matrix representations of the Hamiltonians for the other interactions this signifies that all the off diagonal elements in the matrix can be ignored unless they connect degenerate or nearly degenerate states.

2.2.2 Chemical Shift Hamiltonian

The chemical shift arises due to differences in the electronic environment of the nuclear spins. The external magnetic field induces electronic currents in the sample which create a small local magnetic field, B_{ind}, that can subtract from (shield) or add to (deshield) the main magnetic field causing slight alterations to the nuclear Larmor frequency. The chemical shift, δ, describes the extent of deshielding caused by the presence of these small, local magnetic fields.

The Hamiltonian that describes this interaction is given below

$$\hat{H}_{CS} = -\mu B_{ind} = -\gamma \hat{I}_z B_{ind}. \tag{2.23}$$

The induced field depends linearly on the magnetic field according to

$$B_{ind} = \delta B_0. \tag{2.24}$$

A 3 x 3 chemical shift tensor is necessary to relate the induced field to the B_0 field as these may not be parallel

$$B_{ind} = \begin{pmatrix} \delta^L_{xx} & \delta^L_{xy} & \delta^L_{xz} \\ \delta^L_{yx} & \delta^L_{yy} & \delta^L_{yz} \\ \delta^L_{zx} & \delta^L_{zy} & \delta^L_{zz} \end{pmatrix} \begin{pmatrix} 0 \\ 0 \\ B_0 \end{pmatrix} = \begin{pmatrix} \delta^L_{xz} B_0 \\ \delta^L_{yz} B_0 \\ \delta^L_{zz} B_0 \end{pmatrix}. \tag{2.25}$$

δ^L is the chemical shift tensor relative to the laboratory frame. The element of the tensor δ^L_{mn} describes the field that is induced along the m axis if the external field is applied along the n axis. The external magnetic field is aligned along the z axis so only the δ^L_{xz}, δ^L_{yz} and δ^L_{zz} components contribute to B_{ind}.

The chemical shift Hamiltonian can then be written as

$$\hat{H}_{CS} = -\gamma \hat{I}_x \delta^L_{xz} B_0 - \gamma \hat{I}_y \delta^L_{yz} B_0 - \gamma \hat{I}_z \delta^L_{zz} B_0. \tag{2.26}$$

The first two terms in this equation do not commute with the Zeeman Hamiltonian and can be discarded in the secular approximation leaving the following Hamiltonian

$$\hat{H}_{CS} = -\gamma \hat{I}_z \delta^L_{zz} B_0. \tag{2.27}$$

The chemical shift alters the Larmor frequency of a nucleus according to the following equation,

$$\omega_0 = -\gamma B_0 (1 + \delta^L_{zz}). \tag{2.28}$$

The changes in the Larmor frequency are small in comparison to the Zeeman interaction and vary depending on the magnitude of the B_0 field. The chemical shift is therefore commonly expressed relative to a reference compound in parts per million,

$$\delta = \frac{\nu - \nu_{ref}}{\nu_{ref}}.10^6. \tag{2.29}$$

It is important to remember that the term δ^L_{zz} varies depending on the orientation of the molecule relative to the external magnetic field. In solution, rapid molecular tumbling occurs and the chemical shift is reduced to a single isotropic value δ_{iso} that represents an average of all the possible values (see Equation 2.31).

In solids, motion is restricted and this averaging process does not occur. For a single crystal the value that δ^L_{zz} takes will depend on how the crystal is orientated with respect to the magnetic field. By re-orientating the crystal all the possible values of δ^L_{zz} may be obtained.

A powder sample is made of many different crystallites that sample all the different orientations and all the possible values of δ_{zz}^{L} at once. This leads to a spectrum containing a broad powder pattern formed by superposition of all the resonance lines from all the different crystallite orientations. The discontinuities in the powder pattern coincide with the principal components of the chemical shift tensor. These components are obtained by rotating the chemical shift tensor in the laboratory frame, given in Equation 2.25, into a frame that describes the orientation of the crystallite (the principal axis frame (PAF)).

$$\delta^{PAF} = \begin{pmatrix} \delta_{XX}^{PAF} & 0 & 0 \\ 0 & \delta_{YY}^{PAF} & 0 \\ 0 & 0 & \delta_{ZZ}^{PAF} \end{pmatrix} \tag{2.30}$$

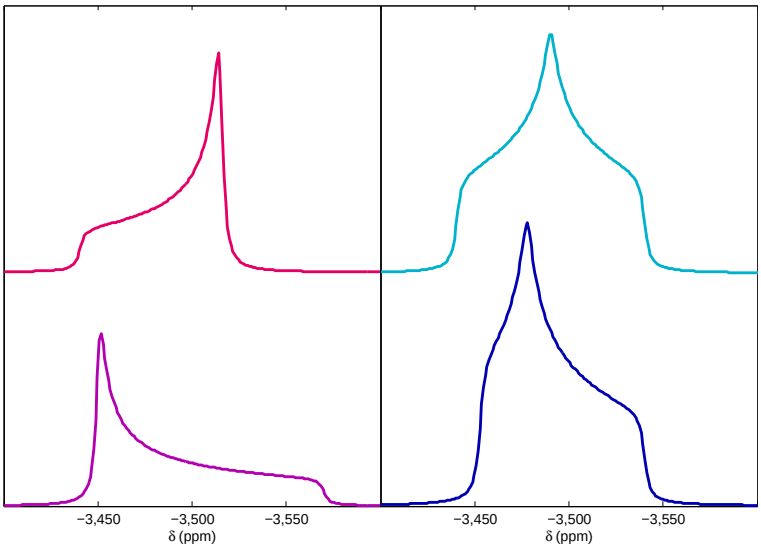


Figure 2.1: A selection of simulated ^{207}Pb CSA patterns. Top left: $\delta_{iso} = -3500$ ppm $\zeta = 50$ ppm and $\eta = 0$, bottom left: $\delta_{iso} = -3500$ ppm $\zeta = -80$ ppm and $\eta = 0$, top right: $\delta_{iso} = -3500$ ppm $\zeta = -50$ ppm and $\eta = 1$, bottom right: $\delta_{iso} = -3500$ ppm $\zeta = -50$ ppm and $\eta = 0.5$.

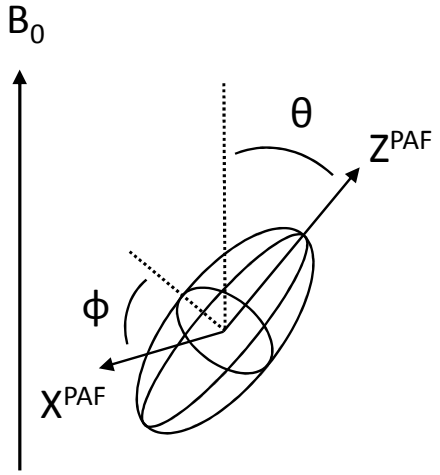


Figure 2.2: The polar angles θ and ϕ show the orientation of the B_0 field in the principal axis frame of the chemical shift tensor. The ellipse represents the chemical shift tensor.

In this frame the chemical shift tensor is diagonal and the principal components can be found on the diagonal. The shape of the powder pattern can be defined using three parameters, the isotropic chemical shift, δ_{iso}, the chemical shift anisotropy (CSA) ζ and the asymmetry, η. Figure 2.1 shows simulated powder patterns generated using different values of δ_{iso}, ζ and η, which are defined in the equations given below.

$$\delta_{iso} = \frac{1}{3}(\delta_{XX}^{PAF} + \delta_{YY}^{PAF} + \delta_{ZZ}^{PAF}), \tag{2.31}$$

$$\zeta = \delta_{ZZ}^{PAF} - \delta_{iso}, \tag{2.32}$$

$$\eta = \frac{\delta_{YY}^{PAF} - \delta_{XX}^{PAF}}{\zeta}. \tag{2.33}$$

The observed chemical shift is related to the chemical shift tensor via the following equation,

$$\delta = \delta_{iso} + \frac{1}{2}\zeta(3cos^2\theta - 1 + \eta sin^2\theta cos2\phi) \tag{2.34}$$

where θ and ϕ are polar angles that define the orientation of the B_0 field in the principal axis frame (see Figure 2.2).

2.2.3 Dipolar Coupling Hamiltonian

The dipolar interaction is a two spin interaction that occurs because the magnetic field produced by one magnetic moment affects the magnetic field produced by another magnetic moment. It is possible to write the Hamiltonian for this interaction using a dipolar coupling tensor D^L that describes how the magnetic field produced by spin S and experienced by spin I varies with the orientation of the internuclear vector with respect to the B_0 field.

$$\hat{H} = -2\hat{I}D^L\hat{S} \tag{2.35}$$

$\hat{I}$ is a vector containing the nuclear spin angular momentum operators, $\hat{I}_x$, $\hat{I}_y$ and $\hat{I}_z$, of nucleus I and $\hat{S}$ is the corresponding vector for spin S. Again it is possible to rotate the tensor describing the dipolar interaction in the laboratory frame D^L into its principal axis frame D^{PAF}, which is aligned with the internuclear vector

$$D^{PAF} = \begin{pmatrix} \text{-d/2} & 0 & 0 \\ 0 & \text{-d/2} & 0 \\ 0 & 0 & \text{d} \end{pmatrix}. \tag{2.36}$$

The dipolar coupling constant, d, is defined as

$$d = \hbar\left(\frac{\mu_0}{4\pi}\right)\frac{1}{r^3}\gamma_I\gamma_S, \tag{2.37}$$

where μ_0 is the vacuum permeability. It is easy to see that the matrix in Equation 2.36 is traceless and so the dipolar coupling does not have an isotropic component. This means that in solution, where the anisotropic interactions are averaged to zero due to rapid molecular tumbling, the effects of the dipolar in-

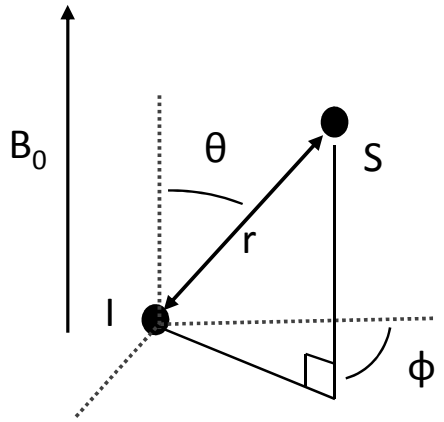


Figure 2.3: The angles θ and ϕ describe the orientation of the internuclear vector between spins I and S, separated by distance r, with respect to the B_0 field.

teraction are rarely observed. Conversely in solids, where motion is restricted, the anisotropic components of the dipolar interaction often have a significant influence on the appearance of the spectrum.

In order to understand the effect the dipolar couplings have on the spectrum we can re-write the Hamiltonian in Equation 2.35 as follows,

$$\hat{H} = -\hbar\left(\frac{\mu_0}{4\pi}\right)\gamma_I\gamma_S\left(\frac{\hat{I}\hat{S}}{r^3} - 3\frac{(\hat{I}r)(\hat{S}r)}{r^3}\right). \tag{2.38}$$

In terms of spherical polar co-ordinates, with the polar angles θ and ϕ defined according to Figure 2.3, this Hamiltonian becomes

$$\hat{H} = -d(A + B + C + D + E + F), \tag{2.39}$$

where:

$A = \hat{I}_z\hat{S}_z(3cos^2\theta - 1)$

$B = -\frac{1}{4}[\hat{I}_+\hat{S}_- + \hat{I}_-\hat{S}_+](3cos^2\theta - 1)$

$C = \frac{3}{2}[\hat{I}_z\hat{S}_+ + \hat{I}_+\hat{S}_z]sin\theta cos\theta e^{-i\phi}$

$D = \frac{3}{2}[\hat{I}_z\hat{S}_- + \hat{I}_-\hat{S}_z]sin\theta cos\theta e^{+i\phi}$

$E = \frac{3}{4}[\hat{I}_+\hat{S}_+]sin^2\theta e^{-2i\phi}$

$F = \frac{3}{4}[\hat{I}_-\hat{S}_-]sin^2\theta e^{+2i\phi}$.

For two dipolar coupled $I = \frac{1}{2}$ nuclei, with eigenstates defined as $|\alpha, \alpha >$, $|\alpha, \beta >$, $|\beta, \alpha >$ and $|\beta, \beta >$, these terms would appear in the matrix form of the dipolar Hamiltonian as follows,

$$\begin{pmatrix} A & C & C & E \\ D & A & B & C \\ D & B & A & C \\ F & D & D & A \end{pmatrix}.$$

Many of these terms do not commute with the Zeeman Hamiltonian so we can make the secular approximation and discard them.

In a heteronuclear spin pair the four Zeeman eigenstates ($|\alpha, \alpha >$, $|\alpha, \beta >$, $|\beta, \alpha >$ and $|\beta, \beta >$) will all have different energies because the two nuclei have different values of γ and hence different Larmor frequencies. In this case we can discard all of the off diagonal terms and only the A term will be present leaving the following Hamiltonian for the secular heteronuclear dipolar coupling,

$$\hat{H}_{dd\ hetero} = -d\hat{I}_z\hat{S}_z(3cos^2\theta - 1). \tag{2.40}$$

For a homonuclear spin pair the Zeeman splitting is the same size for both spins and this leads to eigenstates that have similar energies. For two coupled $I = \frac{1}{2}$ nuclei the $|\alpha, \beta >$ and $|\beta, \alpha >$ states will have the same energy under the Zeeman interaction. It is only the differences between the chemical shifts of the two nuclei that will cause a difference in the energy of these two eigenstates. Frequently, the magnitude of the dipolar coupling will exceed this chemical shift difference and in this situation the $|\alpha, \beta >$ and $|\beta, \alpha >$ eigenstates are considered to be fairly degenerate. This means that in the secular form of the

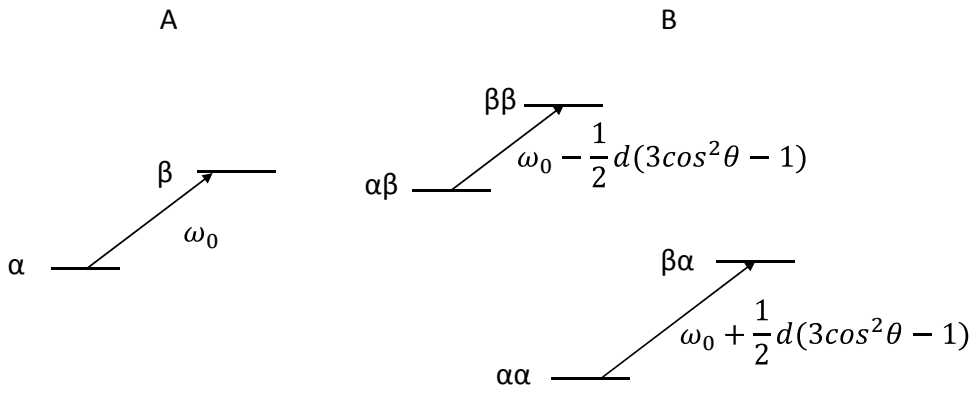


Figure 2.4: Figure A shows the Zeeman interaction of nucleus I which generates a single NMR transition of frequency ω_0. In figure B the spin states for nucleus I with a dipolar coupling to a second nucleus S are shown. The dipolar coupling to the nucleus S modifies the energies of the eigenstates leading to two transitions with slightly different frequencies.

Hamiltonian for a homonuclear dipolar coupled spin pair, given below, both the A and B term must be retained,

$$\hat{H}_{dd\ homo} = -d(3cos^2\theta - 1)[\hat{I}_z\hat{S}_z - \frac{1}{4}[\hat{I}_+\hat{S}_- + \hat{I}_-\hat{S}_+]]. \tag{2.41}$$

The difference between these two Hamiltonians results from the fact that the transverse components of one spin would only be expected to affect the frequency of the other spin if they both had similar Larmor frequencies.

The presence of a heteronuclear dipolar coupling results in the splitting of the corresponding peak in the NMR spectrum. This occurs because the Hamiltonian in Equation 2.40 modifies the energies of the Zeeman eigenstates by $-d(3cos^2\theta - 1)m_I m_S$. This alteration, that gives rise to two transitions with slightly different energies, is displayed schematically in Figure 2.4.

In the NMR spectrum of a single crystal with a heteronuclear dipolar coupling two lines would be observed whose separation would vary depending on the orientation of the crystal with respect to the main magnetic field. For a powder

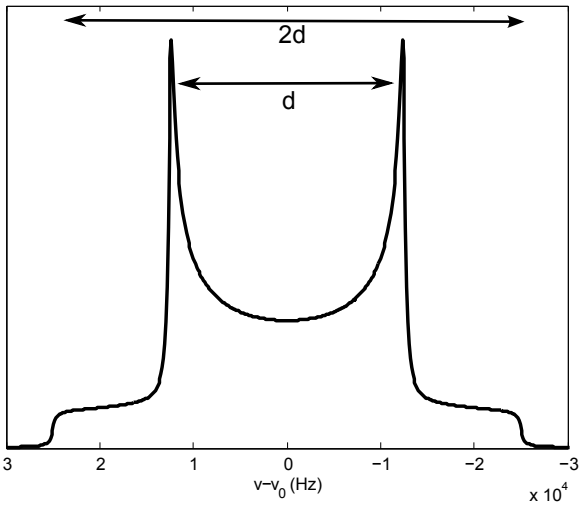


Figure 2.5: Pake pattern produced by simulating the heteronuclear dipolar coupling between a ^{13}C and a ^{1}H nucleus in a powder sample. The dipolar coupling constant d was set to 25 kHz.

sample, composed of many crystallites, all the possible orientations are present at once (and therefore all the possible separations of the two lines). This generates a powder lineshape known as a Pake pattern, which has two maxima separated by the dipolar coupling constant, d (see Figure 2.5).

The influence of the homonuclear dipolar couplings on the NMR spectra of solids is more complicated than for the heteronuclear dipolar couplings. In the case of a powder sample with a single isolated homonuclear dipolar coupling a Pake pattern similar to the heteronuclear case is produced. The principal difference is that the separation between the maxima in the homonuclear case is $\frac{3}{2}$d, not d as for the heteronuclear system.[†]

However, samples with a single isolated homonuclear dipolar coupling are fairly uncommon and many NMR samples contain a network of strong homonuclear

[†]This is due to the differences in the origin of the Pake pattern for the homonuclear case in comparison to the heteronuclear case. To obtain the associated transition frequencies for an homonuclear coupling it is necessary to find eigenstates that diagonalise the Hamiltonian (see the following discussion). There are two allowed NMR transitions between these new eigenstates which have transition frequencies, $\omega_{dd,homo} = \omega_0 \pm \frac{3}{4}d(3cos^2 - 1)$. In the case of a heteronuclear dipolar coupling the allowed transitions are, $\omega_{dd,hetero} = \omega_0 \pm \frac{1}{2}d(3cos^2 - 1)$ (see Figure 2.4). It is easy to see that these two equations differ by a factor of $\frac{3}{2}$ and so the splittings generated by the two different types of dipolar coupling will also differ by the same factor.

dipolar couplings (e.g. the protons in most organic solids). The retention of the B term in the Hamiltonian for the homonuclear dipolar coupling means that there are non-zero off diagonal elements connecting the $|\alpha, \beta >$ and $|\beta, \alpha >$ states. This signifies that these states are not eigenstates of this Hamiltonian. To obtain the NMR frequencies we must diagonalise the Hamiltonian by re-writing it using a different set of basis functions. An appropriate set of basis functions involve the states $|\alpha, \alpha >$ and $|\beta, \beta >$ and two other states that are linear combinations of $|\alpha, \beta >$ and $|\beta, \alpha >$ states.

In the case of a many spin system there will be many degenerate Zeeman eigenstates that are connected by the B term in the Hamiltonian which will lead to mixing of these states. The eigenfunctions of the system will consist of linear combinations of the degenerate Zeeman states. In this basis, the degeneracy is broken, leading to splitting of the previously degenerate energy levels and a correspondingly large number of allowed transitions. This produces extreme line-broadening in NMR spectra containing strongly dipolar coupled spin systems even before the effect of the orientation dependence of the dipolar interaction has been accounted for.

Two experimental consequences of the presence of a strongly dipolar network of spins are worthy of further comment. Firstly, the line broadening observed in strongly coupled spin systems is often so severe it precludes the extraction of most of the useful information from the spectrum. Application of Magic Angle Spinning (MAS), a technique commonly used in solid-state NMR to average anisotopic interactions (see Chapter 3), only generates reasonable resolution in the spectra of these samples at very fast spinning rates. Secondly, the presence of a strongly dipolar coupled network gives rise to polarisation transfer throughout the sample. The presence of off diagonal elements in the matrix

representation of the homonuclear dipolar Hamiltonian implies that the Zeeman states are mixed and that there is spontaneous interconversion between these states. What this amounts to is a continuous exchange of longitudinal magnetisation between the spins in a strongly dipolar coupled spin system. This is called spin diffusion and it forms the basis of the experiments carried out in Chapters 4 and 5.

2.2.4 Quadrupolar Hamiltonian

Nuclei with I $> \frac{1}{2}$ have a non-spherical distribution of electric charge. The quadrupolar Hamiltonian describes the interaction of the electric quadrupole moment of such a nucleus with the surrounding electric field gradients that are generated in the sample by the presence of the electrons

$$\hat{H}_Q = \frac{eQ}{2I(2I-1)}\hat{I}V(\theta)\hat{I}. \tag{2.42}$$

Where Q is the nuclear quadrupole moment, e is the charge of the electron and $V(\theta)$ is a cartesian tensor describing the electric field gradient at the nucleus for a given molecular orientation θ.

The quadrupolar interaction is often very large, particularly if the nucleus has a large value of Q and the electric field gradient is large due to the nucleus residing in a low symmetry environment. In this case, the quadrupolar interaction may approach the size of the Zeeman interaction and further simplifications to this Hamiltonian using the secular approximation cannot be made. Since no experiments on spins with I $> \frac{1}{2}$ were carried out in this work, this interaction will be discussed no further.

2.2.5 J-Coupling Hamiltonian

The J-coupling is sometimes referred to as the indirect coupling. It describes the effect that the magnetic field of one nucleus has on the magnetic field of another nucleus via the influence of the bonding electrons between the two spins. The Hamiltonian describing the interaction is given below

$$\hat{H}_J = 2\pi \hat{I}_1 J_{12} \hat{I}_2. \tag{2.43}$$

Where J_{12} is a tensor that describes the orientation dependence of this coupling. The factor of 2π is necessary in this equation because J couplings are usually quoted in units of Hz.

The J-coupling has an isotropic component that survives the motional averaging that occurs in solution and causes splitting patterns that are frequently observed in solution-state NMR spectra. These splittings are not usually observed in solid-state NMR spectra because the associated frequency difference is typically smaller than the spectral linewidth. The J-coupling also has an anisotropic component that is present in the solid-state but this is usually small and hard to separate from the much larger dipolar interaction which has the same form.

Due to the involvement of the electrons in the coupling mechanism this interaction can be used to identify bonds between nuclei. In contrast, the dipolar interaction can be used to identify nuclei that are close together in space.

2.2.6 Radiofrequency Hamiltonian

During the course of an NMR experiment the bulk magnetisation, generated by the sum of all the nuclear magnetic moments, is manipulated by the application

of radio-frequency (rf) irradiation to the sample. This applied field has a magnitude $2B_1$ and oscillates at the spectrometer reference frequency ω_{ref} with a phase ϕ_{rf}. This oscillating field can be depicted as the sum of two components that rotate in opposite directions in the transverse plane. Only the component that rotates in the same sense as the Larmor frequency will have an appreciable effect on the spin system. The Hamiltonian describing the effect of this resonant component of rf irradiation is given below.

$$\hat{H}_{RF} = \omega_1[cos(\omega_{ref}t + \phi_{rf})\hat{I}_x + sin(\omega_{ref}t + \phi_{rf})\hat{I}_y]. \tag{2.44}$$

Where the nutation frequency of the rf irradiation is defined as $\omega_1 = -\gamma B_1$. The time dependence present in Equation 2.44 complicates any calculations we may wish to carry out using this Hamiltonian. Fortunately, we can generate a time independent Hamiltonian for the application of the rf irradiation if we switch our point of view to an axis frame that rotates around the z axis at the frequency ω_{ref}. This rotating frame Hamiltonian for the rf irradiation is time independent and is displayed below

$$\hat{H}_{RF} = \omega_1(cos(\phi_{rf})\hat{I}_x + sin(\phi_{rf})\hat{I}_y). \tag{2.45}$$

The transformation into the rotating frame also affects the chemically shifted Larmor frequency of the nucleus (termed here ω_0). The rotating frame Hamiltonian including the effects of both the chemical shifted Larmor frequency and the rf irradiation is given below

$$\hat{H}_{RF+Z+CS} = \Delta\hat{I}_z + \omega_1(cos(\phi_{rf})\hat{I}_x + sin(\phi_{rf})\hat{I}_y). \tag{2.46}$$

where the offset Δ is defined as the difference between the chemically shifted Larmor frequency and the spectrometer reference frequency, $\omega_0 - \omega_{ref}$. Generally, we try and carry out NMR using on resonance rf irradiation so that $\omega_0 \approx \omega_{ref}$ and therefore $\Delta \approx 0$. If this is the case and we chose the phase of our applied rf irradiation to be 0 (an x pulse), the Hamiltonian in Equation 2.46 reduces to $\omega_1 \hat{I}_x$. This means that the bulk magnetisation will rotate around the x axis for the duration of the applied rf pulse at a frequency of ω_1.

2.3 The Density Operator at Thermal Equilibrium

To carry out any calculations using these Hamiltonians we need to determine an appropriate starting point for our density matrix. This state can be obtained by defining the density operator at thermal equilibrium which represents the state of the spin system after it has had sufficient time to fully equilibrate with its surroundings. The coherences of this density matrix would be set to zero as no magnetisation would be expected in the transverse plane. The populations of the Zeeman eigenstates would be assumed to obey the Boltzmann distribution. This is given as

$$\rho_{rr} = \frac{exp^{-\frac{\hbar\omega_r}{k_B T}}}{\sum_n exp^{-\frac{\hbar\omega_n}{k_B T}}}. \tag{2.47}$$

To simplify this equation a Boltzmann factor, $\mathbf{B}$, can be defined as,

$$\mathbf{B} = \frac{\hbar\gamma B_0}{k_B T}. \tag{2.48}$$

The value of $\mathbf{B}$ is small because the energy difference between the Zeeman eigenstates ($\hbar\omega_0$) is small in comparison to the thermal energy available at

room temperature (defined by k_BT). This means at room temperature there is only a small difference between the populations of the Zeeman states and so the available signal intensity in an NMR experiment is typically small in comparison to other forms of spectroscopy. The exponential factor present in the numerator of Equation 2.47 can be re-written as follows for both the $|\alpha>$ and $|\beta>$ state of an I = $\frac{1}{2}$ nucleus

$$exp\left(\frac{-\hbar\omega_\alpha}{k_BT}\right) = exp\left(\frac{1}{2}\mathbf{B}\right) \qquad \text{and} \qquad exp\left(\frac{-\hbar\omega_\beta}{k_BT}\right) = exp\left(-\frac{1}{2}\mathbf{B}\right). \quad (2.49)$$

Exponentials can be expanded using the following power series.

$$exp(x) = 1 + x + \frac{x^2}{2!} + \frac{x^3}{3!} + ... \quad (2.50)$$

If we apply this expansion to the exponentials in Equation 2.49, we can truncate it after the first term because the value of **B** is very small (at realistic temperatures). So the following approximations can be made,

$$exp\left(\frac{1}{2}\mathbf{B}\right) \approx 1 + \frac{1}{2}\mathbf{B} \qquad \text{and} \qquad exp\left(-\frac{1}{2}\mathbf{B}\right) \approx 1 - \frac{1}{2}\mathbf{B}. \quad (2.51)$$

The denominator of Equation 2.47 can be approximated as,

$$\sum_n exp^{-\frac{\hbar\omega_n}{k_BT}} \approx 1 + \frac{1}{2}\mathbf{B} + 1 - \frac{1}{2}\mathbf{B} = 2. \quad (2.52)$$

Using this we can now construct the matrix representation of our density operator for $I = \frac{1}{2}$ nuclei at thermal equilibrium as,

$$\hat{\rho_{eq}} = \begin{pmatrix} \frac{1}{2} + \frac{1}{4}\mathbf{B} & 0 \\ 0 & \frac{1}{2} - \frac{1}{4}\mathbf{B} \end{pmatrix} \quad (2.53)$$

This matrix can also be formed from the identity matrix, $\hat{1}$, and the matrix representation of the operator $\hat{I_z}$ in the Zeeman basis [‡].

$$\frac{1}{2}\hat{1} + \frac{1}{2}\hat{I_z}. \tag{2.55}$$

Only the $\hat{I_z}$ operator in this equation will be affected by the application of rf irradiation so it is common to write the equilibrium density operator as,

$$\hat{\rho_{eq}} = \hat{I_z}. \tag{2.56}$$

This can be used as an appropriate starting point of the density matrix in NMR calculations.

2.4 The NMR Experiment

We can use the density matrix approach outlined in Section 2.1 to determine what happens to our spin system during an NMR experiment. This will now be demonstrated using the simple example of a spin system of nuclei with $I = \frac{1}{2}$ that all have the same chemically shifted Larmor frequency and that do not experience any couplings to other nuclei.

At the start of the experiment we assume that the spin system has had sufficient time to reach its equilibrium state, which is represented by the equilibrium density operator, $\hat{\rho}_{eq} = \hat{I}_z$. The only Hamiltonian that acts on the spin system involves the chemical shift and Zeeman effects, which in the ro-

[‡]Matrix representations of some of the operators expressed in the Zeeman basis of a I= $\frac{1}{2}$ nucleus.

$$\hat{1} = \begin{pmatrix} 1 & 0 \\ 0 & 1 \end{pmatrix} \qquad \hat{I_z} = \begin{pmatrix} \frac{1}{2} & 0 \\ 0 & -\frac{1}{2} \end{pmatrix} \quad \hat{I_+} = \begin{pmatrix} 0 & 1 \\ 0 & 0 \end{pmatrix} \quad \hat{I_-} = \begin{pmatrix} 0 & 0 \\ 1 & 0 \end{pmatrix} \tag{2.54}$$

tating frame of reference may be written $\hat{H} = \Delta\hat{I}_z$. $\hat{H}$ and $\hat{\rho}_{eq}$ commute so the commutator in the Louiville-von Neumann Equation (see Equation 2.14) is zero which signifies that the density matrix does not change and that the spin system remains at equilibrium.

To perturb the system from its equilibrium state we have to apply rf irradiation. The Hamiltonian describing the application of rf irradiation is given in Section 2.2.6. Using Equation 2.15 this Hamiltonian can be applied to $\hat{\rho}_{eq}$ to calculate the density matrix just after the rf pulse has finished $\hat{\rho}(t)$. Assuming the radio frequency pulse is an on resonance x-pulse then we obtain the following result for $\hat{\rho}(t)$

$$\hat{\rho}(t) = exp(-i\omega_1\hat{I}_x t)\hat{I}_z exp(i\omega_1\hat{I}_x t). \tag{2.57}$$

The operators $\hat{I}_x$, $\hat{I}_y$ and $\hat{I}_z$ obey cyclic commutation rules[§] so this equation can be re-written as follows

$$\hat{\rho}_t = \hat{I}_z cos(\omega_1 t) - \hat{I}_y sin(\omega_1 t). \tag{2.59}$$

If the pulse has a flip angle of 90° ($\omega_1 t = \frac{\pi}{2}$) then $\hat{\rho}(t) = -\hat{I}_y$ and the magnetisation will become aligned in the transverse plane.

After the pulse the density matrix will then start to evolve under the influence of the Zeeman and chemical shift Hamiltonians so the state of the density matrix at some later time, t_2 is given by

$$\hat{\rho}(t_2) = exp(-i\Delta_1\hat{I}_z t)(-\hat{I}_y)exp(i\Delta\hat{I}_z t) \tag{2.60}$$

[§]If operators $\hat{X}$, $\hat{Y}$ and $\hat{Z}$ commute cyclically then $[\hat{X},\hat{Y}] = i\hat{Z}$ and then

$$exp(-i\theta\hat{X})\ \hat{Y}\ exp(i\theta\hat{X}) = \hat{Y}cos\theta + \hat{Z}sin\theta. \tag{2.58}$$

and therefore

$$\hat{\rho}(t_2) = -\hat{I}_y cos(\Delta t) + \hat{I}_x sin(\Delta t) \tag{2.61}$$

This predicts that the magnetisation will then rotate in the transverse plane. To determine the frequency and direction of this rotation we use the quadrature detection method. This involves representing the detected signal using a complex number obtained by combining the real component of the magnetisation detected along the x axis with the imaginary component that corresponds to the magnetisation detected in the y direction. This process corresponds to obtaining an expectation value of the $\hat{I}_+$ operator (see Equation 2.19) as shown below

$$\text{if} \quad \hat{\rho} = \begin{pmatrix} 0 & M^* \\ M & 0 \end{pmatrix} \qquad < I_+ >= tr(\hat{\rho}\hat{I}_+) = \begin{pmatrix} 0 & M^* \\ M & 0 \end{pmatrix} \begin{pmatrix} 0 & 1 \\ 0 & 0 \end{pmatrix} = M. \tag{2.62}$$

Therefore, in an NMR experiment it is the -1 quantum coherence of the density matrix that represents the detectable magnetisation.

The oscillating signal produced in a NMR experiment eventually decays to zero due to various relaxation processes, which return the system to its equilibrium state. Spin-lattice relaxation involves an exchange of energy between the system and the surroundings that restores the populations of the Zeeman eigenstates to their equilibrium values. This gradual return of magnetisation aligned with the main magnetic field along the z-axis is described in the following equation,

$$M_z = M_{eq}\Big(1 - exp\Big(\frac{t}{T_1}\Big)\Big). \tag{2.63}$$

where M_z represents the z magnetisation, M_{eq} is the equilibrium z magnetisation, t is the time given for relaxation to occur and T_1 is the spin-lattice

relaxation time constant. The T_1 value governs the rate at which the magnetisation returns to its equilibrium distribution. Standard NMR experiments, such as inversion-recovery and saturation-recovery experiments, can be used to measure the sample's T_1 value. Knowledge of the T_1 time constant is important because it limits the repetition rate of an NMR experiment. In principle a delay between subsequent scans of five times the T_1 should be used, allowing the magnetisation to fully return to equilibrium, producing quantitative spectra. However, in practice NMR experiments may be carried out with much shorter delays between scans in order to decrease the total acquisition time.

These results could have been produced using simpler methods such as the vector model description of the NMR experiment. However, the advantage of the density matrix approach stems from the fact it can easily be extended to describe much more complicated spin systems than the one described above. For example, it can be used to describe spin systems containing quadrupolar nuclei and spin systems that contain coupled spins, including those exhibiting strong coupling. In such systems the density matrix can support higher coherence orders which can be manipulated over the course of certain NMR experiments. It is not possible to interpret the results of these experiments using a vector model description of NMR.

Chapter 3

Solid-State NMR Methods

This chapter will outline some important solid-state NMR techniques that are relevant to the work carried out in this thesis.

3.1 Magic Angle Spinning

The samples analysed using solid-state NMR are frequently in powder form and consist of crystallites that display all possible molecular orientations. All of the interactions described in Chapter 2 are orientation dependent and so powder samples will generally produce spectra with a large spread of overlapping resonance frequencies which may obscure required information (e.g. the isotropic chemical shift). For this reason the field of solid-state NMR was slower to develop than its solution-state counterpart (the effects of anisotropic interactions in solution are usually absent due to rapid molecular tumbling).

Magic Angle Spinning (MAS), discovered by Andrew, Bradbury and Eaddes in 1958[7] and susbsequently and independently in 1959 by Lowe[6], is one of the most routinely used techniques in solid-state NMR. In a MAS experiment narrowing of spectral linewidths is achieved by spinning the sample rapidly

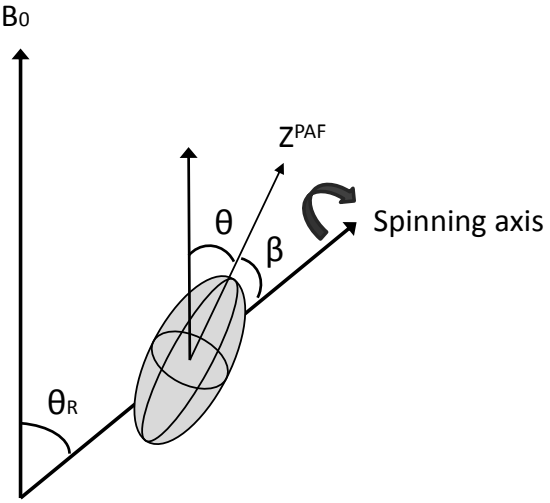


Figure 3.1: In a Magic Angle Spinning experiment the sample is spun rapidly around an axis inclined at $\theta_R = 54.74°$ away from the B_0 field. The grey ellipse represents an interaction tensor.

around an axis orientated at 54.74 ° (the magic angle) with respect to the applied magnetic field (B_0). This line narrowing arises because the molecular orientation dependence of many of the nuclear spin interactions described in Chapter 2 take the form $3cos^2\theta - 1$. The average orientation dependence of a nuclear spin interaction under sample spinning, around an axis inclined at an angle θ_R away from the magnetic field, can be given as

$$< 3cos^2\theta - 1 >= \frac{1}{2}(3cos^2\theta_R - 1)(3cos^2\beta - 1) \tag{3.1}$$

with the angle β defined as shown in Figure 3.1. If $\theta_R = 54.74°$ then $3cos^2\theta_R - 1 = 0$ and $< 3cos^2\theta - 1 >= 0$. So, providing that the sample spinning is sufficiently fast, then the anisotropic parts of the interactions are averaged and only the isotropic components remain.

What constitutes a sufficiently fast spinning speed depends on the interactions that need to be averaged. Nuclear spin interactions may be classified as either homogeneous or inhomogeneous on the basis of their behaviour under MAS[12]. Examples of inhomogeneous interactions include the CSA and isolated dipolar couplings. These interactions are averaged efficiently by sample spinning that

exceeds the frequency spread caused by the interaction. At lower MAS rates spinning sideband patterns are observed which consist of multiple sharp peaks separated by the spinning frequency.

Homogeneous interactions, exemplified by a network of strongly dipolar coupled spins, are much harder to average and much faster spinning speeds are required to obtain high resolution spectra. Slow spinning does little to improve the spectral resolution. Spinning sidebands separated by the rotor frequency are observed at intermediate spinning rates but these are typically much broader than those associated with inhomogeneous interactions. The difficulties in obtaining high resolution spectra of homonuclear dipolar coupled spin systems can be related to the phenomenon of spin diffusion (see Section 2.2.3 and Chapters 4 and 5). Broadly speaking, if MAS is to be used to average an interaction then the state of the system should be constant during one rotor period. The presence of homonuclear dipolar couplings mixes the Zeeman eigenstates meaning that they are no longer constant over the rotor period and so the interaction is difficult to average. Current research suggests that spinning rates greatly in excess of 100 kHz (faster than currently available) would be necessary to average the effects of a strongly dipolar coupled network of protons[13].

The presence of a network of dipolar-coupled spins can lead to line broadening in the spectra of other nuclei. For example a ^{13}C nucleus with a heteronuclear dipolar coupling to a proton which is part of a network of dipolar coupled protons may still show a broad linewidth even at fast spinning rates. This arises because the spin state of the proton in the heteronuclear coupling will vary during the rotor period due to its couplings to other protons and therefore the heteronuclear dipolar interaction between this proton and the carbon will

also be time dependent. Proton decoupling can be used to mitigate this effect.

3.2 Decoupling

Decoupling involves the use of rf irradiation to rotate the nuclear spin polarisation leading to the averaging of certain interactions. This contrasts with MAS which averages interactions using physical rotation of the sample. Decoupling sequences used in solid-state NMR can be divided into two types, heteronuclear decoupling and homonuclear decoupling.

Heteronuclear decoupling, mentioned briefly in the previous section, is typically used during the acquisition period of an NMR experiment. Spectral line broadening generated due to a heteronuclear dipolar coupling may persist even at fast MAS rates if one of the nuclei in the heteronuclear coupling is part of a network of dipolar coupled spins, as is commonly the case for protons. Decoupling removes the effects of heteronuclear dipolar couplings and the simplest method of achieving this is to apply continuous, high power, rf irradiation to the sample, on resonance for the nucleus being decoupled, for the duration of the acquisition time.

High power decoupling tends to work well at lower spinning rates. Synchronisation of the physical rotation of the sample and the rotation of the spin polarisation under applied rf tends to produce atypical effects and when the MAS rate approaches the nutation rate the decoupling efficiency drops. At higher spinning rates (>40 kHz MAS) the use of low power decoupling will often produce superior results.[14]

Other decoupling sequences have been developed that result in superior decoupling efficiency under MAS in comparison to continuous wave decoupling.

One of the earlier examples of such a sequence is two pulse phase modulation (TPPM), which involves application of a continuous train of pulses with a tip angle of slightly less than 180° with a phase alternation of $\pm\phi$, where ϕ is usually between 0-30°.[15] Alternative decoupling sequences have been proposed which display improved efficiency, such as SPINAL-64 and SWf-TPPM. These are both modifications of the basic TPPM sequence with SPINAL-64 employing a more complicated phase modulation while SWf-TPPM applies a frequency sweep by varying the decoupling sequence pulse lengths.[16;17]. Both SPINAL-64 and SWf-TPPM were used during acquisition of heteronuclear correlation spectra recorded in Chapter 6.

Homonuclear decoupling is used to suppress the effects of the dipolar interaction between like spins and is most commonly used in ^{1}H NMR where the network of dipolar coupled protons often leads to low resolution in spectra. Various sequences are available for decoupling proton homonuclear dipolar couplings, most of which were initially designed for use in the slow spinning regime where the cycle time of the applied decoupling pulse sequence is typically much less than the MAS rotor period. Many decoupling sequences can be applied in a windowed fashion allowing direct acquisition. This involves sampling the NMR signal during multiple delay periods separated by blocks of the decoupling pulse sequence. As the set-up of such experiments may be quite complex windowless decoupling can be used as an alternative. This involves continuous rf irradiation applied in the indirect dimension of a 2D experiment.

Lee-Goldburg decoupling is one of the earlier examples of a windowless homonuclear decoupling sequence. It involves the application of continuous off-resonance irradiation that results in the precession of magnetisation around an axis tilted at the magic angle[18] (in the case of on resonance irradiation the nuta-

tion axis is in the transverse plane). This is achieved experimentally by finding the proton nutation rate for on-resonance rf, ν_1, then switching the transmitter frequency (and therefore changing the offset) to $\Delta\nu = \nu_1/\sqrt{3}$ and subsequently reducing the applied proton rf irradiation to achieve a nutation frequency of $\sqrt{{\nu_1}^2 - \Delta\nu^2}$. This results in the precession of proton magnetisation about the magic angle which efficiently averages the spin part of the homonuclear dipolar Hamiltonian (providing that the applied rf field is sufficiently large). Modified versions of Lee-Goldburg decoupling, such as Frequency-Switching Lee-Goldburg (FSLG)[19] and Phase-Modulated Lee-Goldburg (PMLG)[20], are commonly used.

One complication of using rf fields to average the homonuclear dipolar interaction is that the rf irradiation also partially averages chemical shifts. This means that precessional frequencies of the nuclei are reduced by a scaling factor under application of the decoupling sequence. Therefore, the frequency scale obtained in an experiment carried out using decoupling should be corrected using the scaling factor prior to analysis. This scaling factor is sequence dependent and although it is possible to calculate theoretical scaling factors for each sequence, experimental determination of the scaling factor is usually recommended.

Due to the persistence of the proton homonuclear dipolar couplings at higher spinning speeds, improvements in spectral resolution can still be made by using decoupling at fast MAS. Some examples of decoupling sequences which operate well at intermediate and fast MAS rates include PMLG and the DUMBO (Decoupling Under Mind Boggling Optimisation) family of pulse sequences[20–28].

Unlike many other decoupling sequences which were originally designed by

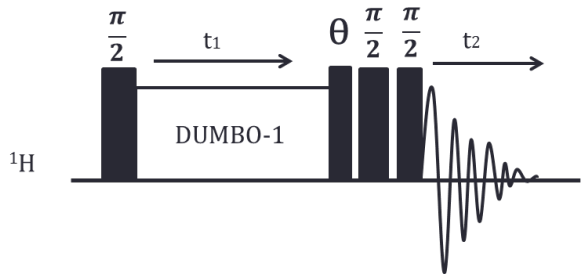


Figure 3.2: Pulse sequence using DUMBO-1 to correlate a high resolution dimension with a MAS dimension.

taking into account theoretical considerations the complicated phase modulation of the DUMBO decoupling sequence was obtained using a numerical optimisation procedure. A Fourier series was used to generate the shape of the DUMBO-1 pulse and the series coefficients were optimised in order to minimise the effect of dipolar couplings while maximising the scaling factor[25]. As is the case for many other homonuclear decoupling sequences the application of the DUMBO pulse sequence results in an effective rf field applied close to the magic angle (58° for the DUMBO-1 sequence). DUMBO can be applied in a windowed fashion for direct detection or as a windowless sequence in the indirect dimension. As windowless decoupling is usually easier to implement than windowed sequences DUMBO is often used as part of a two dimensional experiment that correlates the high resolution dimension with a MAS dimension. The relevant pulse sequence is displayed in Figure 3.2. The magic angle pulse has a tip angle of θ. Theoretically $\theta = 58°$, however experimental calibration of this angle is recommended[26].

Figures 3.3 and 3.4 show spectra of an hydroxyapatite/polylactic acid composite nanomaterial ([PLA_{ex}]-[$C_6H_9O_4$] - see Chapter 6) acquired using the pulse sequence displayed in Figure 3.2. The two prominent peaks in the spectra both originate from the polylactic acid (PLA) component of the material with the peak at ≈1 ppm in the direct dimension corresponding to the PLA

methyl protons and the peak at ≈5 ppm corresponding to the PLA methoxy protons. The protons in the PLA form part of dipolar coupled network and the ability of the DUMBO sequence to effectively average these dipolar couplings is demonstrated as the linewidths in the indirect dimension, acquired using DUMBO decoupling, are narrower than those in the direct dimensions acquired using MAS alone.

Spectra correlating a DUMBO-1 decoupled dimension with a MAS dimension can be used to calculate the experimental scaling factor. The only difference between the spectrum in Figure 3.3 and the spectrum in Figure 3.4 is in the indirect dimension. Figure 3.3 shows the frequencies obtained under the decoupling sequence while the spectrum in Figure 3.4 has been appropriately scaled so that the frequencies match those that would have been obtained without decoupling. The theoretical maximum scaling factor obtainable with DUMBO-1 is 0.52^{25} and the experimentally determined scaling factors were typically close to this value.

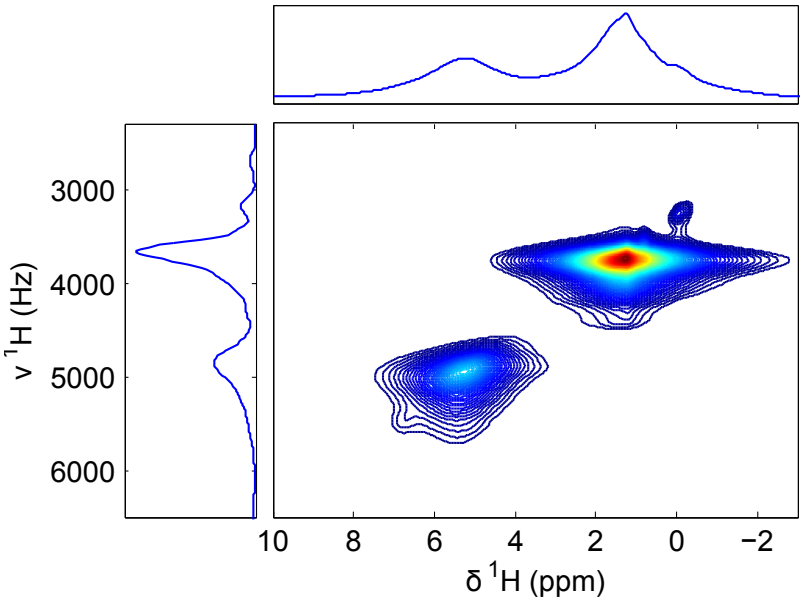


Figure 3.3: ^{1}H-^{1}H spectrum of an hydroxyapatite/polylactic acid composite nanomaterial correlating a MAS dimension with a high resolution DUMBO-1 dimenison. Spectrum not corrected for scaling of the proton frequency in the indirect dimension.

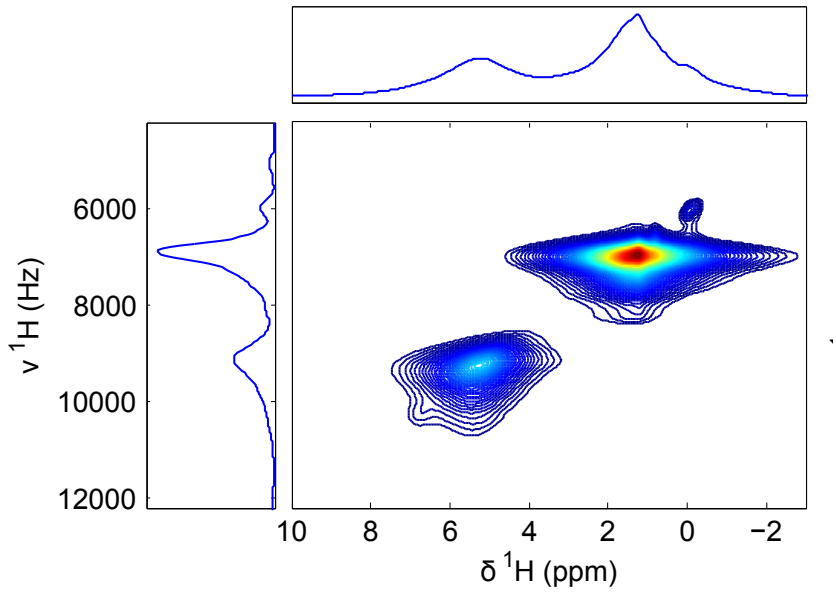


Figure 3.4: ^{1}H-^{1}H spectra of an hydroxyapatite/polylactic acid composite nanomaterial correlating a MAS dimension with a high resolution DUMBO-1 dimenison. Indirect dimension correctly scaled.

3.3 Cross Polarisation

Cross polarisation (CP) is a widely used technique in solid-state NMR that achieves polarisation transfer between two different types of nuclei which are coupled via a heteronuclear dipolar coupling[29;30]. It is most commonly used to transfer magnetisation from abundant nuclei with a high magnetogyric ratio (from here onwards we will refer to the proton nucleus as the starting point of the CP experiment) to dilute spins with a low magnetogyric ratio (e.g. ^{13}C). For nuclei with a low abundance the available signal intensity is typically a limiting factor in performing an NMR experiment.

Proton nuclei have a higher magnetogyric ratio than most other nuclei and so will have a higher equilibrium population difference (see Section 2.3). During a CP experiment this higher polarisation can be transferred (partially) to nuclei with a lower magnetogyric ratio. Additionally, proton nuclei usually have much shorter relaxation times than dilute spins. This means that CP experiments usually require much shorter relaxation delays and therefore can be carried out with much lower overall acquisition times in comparison to direct excitation experiments. CP steps are also frequently employed in multidimensional NMR experiments to reveal spatial proximity between different nuclei (as heteronuclear dipolar couplings are through space interactions).

The basic pulse sequence for CP is displayed in Figure 3.5. A 90° proton pulse is applied followed by application of continuous rf irradiation with a 90° phase shift with respect to the first pulse which spin-locks the proton magnetisation in the transverse plane. During this period of time, called the contact time, rf irradiation is also applied to the heteronucleus. To achieve the polarisation transfer the rf fields applied to the proton and the heteronucleus (X) must satisfy the Hartman-Hahn matching condition, $\omega_1^H = \omega_1^X$ [30]. Broadly

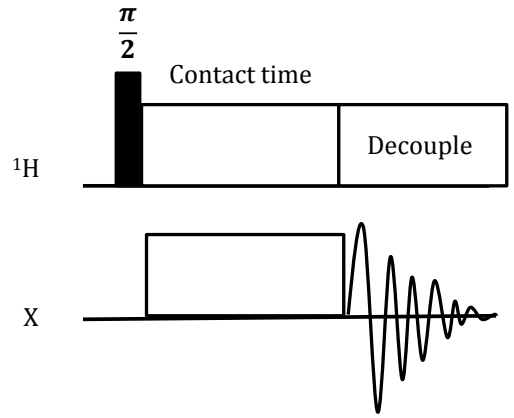


Figure 3.5: The pulse sequence for a CP experiment used to transfer polarisation from a proton nucleus to a heteronucleus (X).

speaking this transfer of magnetisation is possible because in the rotating frame the applied B_1 field provides the axis of quantisation for the nuclear spin states. Under the Hartmann-Hahn condition the energy gaps between these spin states are equal and so magnetisation transfer may occur. The rotating frame Hamiltonian for heteronuclear spin pair with rf irradiation applied to both spins along the x axis can be written as.

$$\hat{H} = -d(3cos^2\theta - 1)\hat{I}_z\hat{S}_z + \omega_I\hat{I}_x + \omega_S\hat{S}_x. \tag{3.2}$$

If we rotate the axis system we are using so that the z-axis is re-defined as being along the axis of the applied B_1 field we obtain the following Hamiltonian.

$$\hat{H}' = -d(3cos^2\theta - 1)\hat{I}_x\hat{S}_x + \omega_I\hat{I}_z + \omega_S\hat{S}_z. \tag{3.3}$$

The matrix representation of this Hamiltonian can be written as,

$$\hat{H}' = \frac{1}{2}\begin{pmatrix} \omega_I + \omega_S & 0 & 0 & \mathbf{d}/2 \\ 0 & \omega_I - \omega_S & \mathbf{d}/2 & 0 \\ 0 & \mathbf{d}/2 & \omega_S - \omega_I & 0 \\ \mathbf{d}/2 & 0 & 0 & -\omega_I - \omega_S \end{pmatrix} \tag{3.4}$$

where $\mathbf{d} = -d(3cos^2\theta - 1)$. At the Hartmann-Hahn condition $\omega_S = \omega_I$. Also during CP the rf irradiation applied during the contact time normally exceeds the strength of the dipolar coupling. If $\omega >> d$ then we can use the secular approximation to discard off-diagonal elements in the matrix elements that connect non-degenerate states (see Equation 2.22) . So the matrix representation of the Hamiltonian can be simplified as follows,

$$\hat{H}' = \frac{1}{2}\begin{pmatrix} 2\omega & 0 & 0 & 0 \\ 0 & 0 & \mathbf{d}/2 & 0 \\ 0 & \mathbf{d}/2 & 0 & 0 \\ 0 & 0 & 0 & -2\omega \end{pmatrix}. \tag{3.5}$$

As was discussed in the case of the homonuclear dipolar coupling (see Section 2.2.3), non-zero off-diagonal elements in the matrix representation of the Hamiltonian imply that the states are mixed and that magnetisation can be exchanged. So, during the contact time of a CP experiment magnetisation can be exchanged between two nuclei which are coupled by a heteronuclear dipolar coupling.

The application of MAS leads to complications in the CP experiment because the Hartmann-Hahn condition is modulated by the spinning frequency.[31] The CP matching condition under MAS is,

$$\omega_I \pm \omega_S = n\omega_r \qquad\qquad n = 0, 1, 2, 3... \tag{3.6}$$

At moderate MAS rates and above the matching profile is broken up into a series of sidebands and the most efficient CP is obtained under these sideband conditions (usually $n = 1$ or 2). Magnetisation transfer at the centreband

condition ($n = 0$) tends to be poor. The matching conditions under MAS are also narrower which makes it difficult to maintain efficient CP across the sample. The use of shaped pulses in the contact time, such as ramps, may help to alleviate some of these issues[32].

3.3.1 Lee-Goldburg Cross Polarisation

During the contact time of an ordinary CP experiment spin diffusion (see Section 2.2.3 and Chapters 4 and 5), between dipolar coupled protons, often takes place in addition to the magnetisation transfer within heteronuclear spin pairs. Therefore, the magnetisation transferred from a nearby proton to a heteronucleus may have contributions from more distant protons due to the effect of spin diffusion. Lee-Goldburg Cross Polarisation (LGCP) is a modified CP sequence that decouples the homonuclear dipolar couplings, using Lee-Goldburg decoupling (see Section 3.2), while transferring magnetisation via the heteronuclear dipolar couplings[18;33]. This prevents proton spin diffusion during the contact time and only magnetisation transfer between heteronuclear spin pairs takes place.[33]

3.4 Recoupling Sequences

While the use of MAS produces superior spectral resolution it also results in a loss of the information associated with the anisotropic components of interactions (which are averaged under MAS) and in some cases this information may be of interest. Recoupling sequences are pulse sequences which enable the selective re-introduction of specific NMR interactions under MAS conditions. This is possible because each of the nuclear spin interactions will display certain transformation properties under rf irradiation induced rotation of the nuclear

spin polarisation. Equally, each interaction will transform in a certain manner under physical sample rotation occurring due to MAS. Therefore, it is possible to design NMR experiments that select certain interactions and suppress others by synchronising the applied rf pulses with the sample rotation.

In this work two different recoupling sequences, RFDR (Radio Frequency-Driven Recoupling) and the $SR6_6^2$ sequence, were used to selectively re-introduce the homonuclear dipolar interaction under MAS (see Chapter 5). The RFDR pulse sequence is widely used to recouple homonuclear dipolar couplings and it consists of four 180° pulses, each applied at the centre of a rotor period, with an appropriate phase alternation of the pulses.[34] The $SR6_6^2$ is an example of an R-symmetry sequence. R-sequences were introduced by M. H. Levitt as part of work describing how new rotor synchronised recoupling sequences could be developed through consideration of the rotational properties of the various nuclear spin interactions.[35]

The R-sequences have the generic form RN_n^ν, where N, n and ν are all positive integers. N is the number of 180° pulses* which fit into n rotor periods. A $\pm\phi$ phase alternation is applied to the pulses with the phase angle given as $\phi = 180° \frac{\nu}{N}$. So for example, the $R6_6^2$ sequence consists of six 180° pulses within six rotor periods with alternating phases of ±60°. The $SR6_6^2$ is a variant of the $R6_6^2$ sequence which contains modifications to this basic sequence, including the use of $90_{180}270_0$ composite pulses and supercycling (repetition of the sequence with a phase shift), which help compensate for certain errors.[36]

Since their development R-sequences have been used in a wide range of experiments to recouple various NMR interactions, e.g. the CSA[37;38], heteronuclear

*Composite or shaped pulses that have the same overall effect as a 180° pulse may also be used.

dipolar couplings[39;40]. Additionally, many successful recoupling sequences in previous use were found to conform to the principles used in the design of symmetry sequences. For example, in this formalism the RFDR sequence can be described as a variation of the $R4_4^1$ sequence.

Interestingly, R-sequences have also been successfully employed to carry out proton homonuclear dipolar decoupling[41;42]. This is possible because sequences such as the $R8_1^4$ and the $R16_3^8$ recouple the isotropic chemical shift and the J-coupling but suppress all other NMR interactions. An example of the use of R-sequences for decoupling will be given in Chapter 6.

3.5 Dynamic Nuclear Polarisation

Dynamic nuclear polarisation (DNP) is a method that can drastically increase the available signal intensity in an NMR experiment by transferring the polarisation of unpaired electrons to nearby nuclei. The electron polarisation in a magnetic field is much larger than that of the nuclear polarisation so significant signal enhancements can be obtained. There are a variety of mechanisms which can be used to achieve this transfer of polarisation between electrons and nuclei such as the Overhauser effect, the solid effect, the cross effect and thermal mixing. The cross effect in particular has been applied successfully to solid samples under high magnetic fields and was used to record the DNP enhanced spectra presented in Chapter 6. This section intends to provide an overview of some of the basic theory underpinning the cross effect. For a more complete description of the theory and application of DNP relevant literature should be consulted.[43]

For effective polarisation transfer via the cross effect a three spin system, con-

sisting of two dipolar coupled electron spins and a nuclear spin, is necessary. In order to generate this type of system NMR samples used in DNP experiments are often prepared by the addition of a suitable radical that acts as the polarising agent. To achieve transfer via the cross effect the following condition must be satisfied.

$$\omega_{0S2} - \omega_{0S1} = \omega_{0I} \tag{3.7}$$

Where ω_{0S2} and ω_{0S1} are the electron Larmor frequencies of two electrons present in the radical. Due to this condition the inhomogeneous linewidth of the radical's EPR spectrum must be large so that it contains two frequencies that are separated by the nuclear Larmor frequency. Therefore, an efficient polarising agent used for DNP enhancement via the cross effect would have a small homogeneously broadened EPR (Electron Paramagnetic Resonance) linewidth (δ) but also have inhomogeneously broadened linewidth (Δ), that is larger than the Larmor frequency (ω_{0I}) of the nucleus that receives that transferred polarisation, i.e. $\Delta > \omega_{0I} > \delta$.

In EPR spectra it is frequently the g-anisotropy, an effect that resembles the chemical shift anisotropy in ordinary solid-state NMR spectra, that results in the large inhomogeneous broadening. Certain nitroxide radicals have previously been used as polarisation agents as they tend to produce EPR spectra with large inhomogeneous linewidths and biradicals in particular, that contain two dipolar coupled spin pairs, make good polarising agents for transfer via the cross effect. AMUPol (see Figure 3.6)[44] is an example of a biradical polarising agent that can be dissolved in aqueous solution that was used to record the DNP spectra presented in this thesis.

Figure 3.7 shows an energy level diagram for the three spin system required to achieve the cross effect. It can be used to explain the mechanism of polarisation

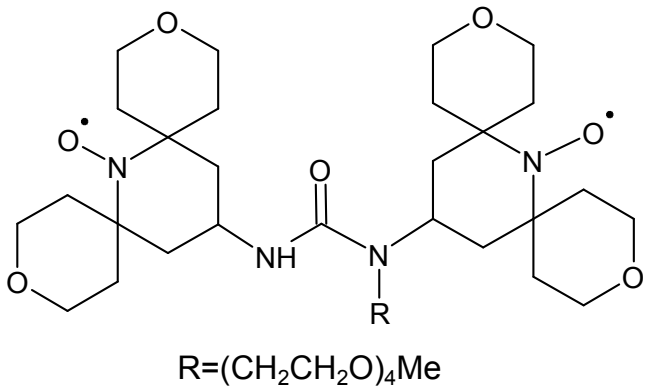


Figure 3.6: Structure of the DNP polarising agent AMUPol.

transfer. In a general three spin system represented in Figure 3.7:A there are eight non-degenerate energy levels with NMR transitions marked as ω_{0I}. Due to the small Botzmann factor present in NMR the difference in the populations of the states connected by an NMR transition is small. If the condition given in Equation 3.7 is satisfied two of the energy levels (4 and 5) will become degenerate (see Figure 3.7:B and 3.7:C). Applying microwave radiation at the frequency ω_{0S1} saturates the EPR transitions of one of the two dipolar coupled spin systems. This is displayed in Figure 3.7:B. The states labelled 4 and 5 are degenerate and so will form mixed states and in this case the transitions marked CE are allowed. By saturating the EPR transitions with a frequency ω_{0S1} the populations of the states labelled 1, 4, 5 and 8 will become equalised. In terms of the NMR transitions this leads to an increased population in the β state and therefore a negative enhancement of the signal intensity.

Figure 3.7:C outlines how a positive signal enhancement can be generated using DNP. This occurs in the same way as for the negative enhancement in Figure 3.7:B except this time a microwave frequency of ω_{0S2} is applied which saturates the EPR transitions of the other electron spin. This then equalises the populations of the states labelled 2, 4, 5 and 7. In terms of the NMR transitions this leads to an increased population of the α state and hence a positive signal enhancement. In practice during the course of a DNP experi-

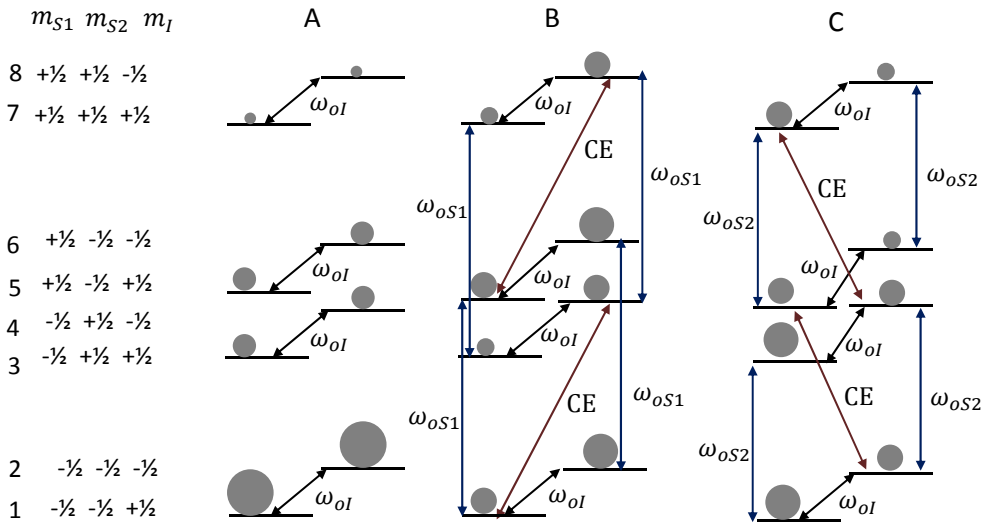


Figure 3.7: Energy level diagrams showing how polarisation transfer can be achieved using the cross effect. A: Displays the NMR transitions. B: Demonstrates how a negative DNP enhancement is obtained via the cross effect. C: Demonstrates how a positive DNP enhancement is obtained via the cross effect.

ment continuous microwave irradiation at one frequency is applied, therefore in any one experiment only case B or C (not both) will apply.

Chapter 4

Spin Diffusion and Domain Sizes in Polymers

Spin diffusion NMR experiments are a well established method of determining domains sizes in diblock polymers and a vast amount of literature has been generated on the subject. Spin diffusion involves the spatial re-distribution of magnetisation via the homonuclear dipolar couplings without either material transport or energy exchange with the surroundings. It is most apparent in systems that contain a network of strongly dipolar coupled spins and proton nuclei are a common choice for spin diffusion studies. A typical spin diffusion experiment involves generating a non-equilibrium magnetisation distribution by selecting magnetisation in a particular part of the sample. During the subsequent mixing time the spin diffusion process acts to return the magnetisation to its equilibrium distribution. By monitoring either the decrease in magnetisation in the initially selected region (the source) or the increase in magnetisation in the initially de-selected region (the sink) the distances between different polymer domains can usually be inferred.

Some of the earlier spin diffusion studies were based on the Goldman-Shen

experiment[45] which selects regions of the sample according to relaxation time differences and is typically used to study block copolymers containing both rigid and mobile domains. Various improvements to this methodology have been made, such as using dipolar filters[46–57] to select the mobile component or using DQ (Double Quantum) filters to select the rigid component[58–62]. These experiments can be carried out under static conditions with proton detection, generating spectra with very broad linewidths for the rigid component. However, the mobile component usually has a much narrower linewidth due to the effects of motional averaging of the proton homonuclear dipolar couplings. Therefore, it is usually possible to deconvolute the spectra of such samples and assess the changes in intensity of the rigid and mobile components independently.

Alternatively, the initial selection can be carried out on the basis of chemical shift differences within the sample and an experiment using a chemical shift filter, suitable for application at low MAS rates, was proposed[46]. At low MAS rates proton spectra of rigid polymers typically show poor resolution and cross polarisation and ^{13}C detection must be used in order to acquire spectra that can be analysed. The disadvantage of this method is that it leads to increased acquisition times in comparison to proton detected experiments. It is possible to obtain well resolved proton spectra at low and intermediate MAS rates by using specially designed pulse sequences that decouple the proton homonuclear dipolar couplings[63–65]. Due to recent technological advances fast MAS can now be used to acquire high resolution proton spectra without the need for complicated decoupling and this methodology has already been used in conjunction with spin diffusion experiments[50;60;66]. In this chapter spin diffusion experiments carried out under fast MAS will be applied to study the domain sizes of a range of diblock polymers and an investigation into the

effects of T_1 relaxation on these results will also be carried out.

The build-up or decay curves, produced when carrying out the spin diffusion experiments with increasing mixing times, from either the source or sink region, must be analysed to obtain a domain size. The transfer of magnetisation occurring during the mixing time can be modelled mathematically in the same fashion as ordinary material diffusion and general texts in this field are available for reference[67]. Fick's second law can be be used to provide appropriate solutions

$$\frac{\partial m}{\partial t} = D\left(\frac{\partial^2 m}{\partial x^2} + \frac{\partial^2 m}{\partial y^2} + \frac{\partial^2 m}{\partial z^2}\right). \tag{4.1}$$

The rate of diffusion is defined by the spin diffusion coefficient - D. The above equation is valid for systems where the diffusivity is constant and isotropic (i.e where D is the same in all directions and does not change due to varying concentration of the diffusing substance). Full analytical solutions are available for a variety of initial and boundary conditions but these tend to become more complicated as the dimensionality of the system increases[46;58;68–70]. An initial rate approximation has also been developed which uses a fit to the initial linear section of the diffusion profile to extract a domain size, providing that the sample morphology is known[46;71]. An alternative approach involves using simulations to numerically solve the spin diffusion equation[53;68;71–73].

The initial rate approximation is probably the most widespread method of analysis due to its simplicity. The advantage of a numerical simulation is that the effects of T_1 relaxation can be incorporated into the simulation[71;72;74;75]. This is necessary when T_1 relaxation occurs on the same time scale as spin diffusion because the results will depend on both processes. Typically the analytical solutions were developed without taking relaxation into consideration and are therefore valid in situations where spin diffusion is fast in compari-

son to the T_1 time. In this scenario the magnetisation would reach full re-equilibration before significant relaxation effects are observed. A method to mitigate the effects of T_1 relaxation involves applying a $\pm$z phase alternation on a pulse prior to the mixing time[71]. Using this phase cycle the decay in magnetisation caused by T_1 has an exponential form and the data can be corrected by multiplication by $\exp(t_m/T_1)$. The correction is valid so long as all the sites in the sample have the same T_1 value. For samples that show a strong, spatial T_1 variation this back correction will not be able to completely separate spin diffusion and relaxation effects[74]. Existing studies have compared data analysed using the T_1 corrected initial rate approximation method with the results of numerical simulations[51;75;76]. As the initial rate approximation represents a simple method of analysis of spin diffusion data some suggestions have been proposed as to which T_1 values give the best match in comparison to the simulation results when used in a back-correction[76].

As all of the methods described above are based on Fick's diffusion equation (Equation 4.1) an accurate value of the diffusion coefficient is necessary to extract domain sizes. A significant number of publications detail different methods of calculating the spin diffusion coefficient[46;49;57;73] . These methods include calculations based on spectral linewidths, using a calibration rule developed on the basis of T_2 values and calibrating NMR results against domain sizes obtained via other methods, e.g. Small Angle X-Ray Scattering (SAXS). There are also examples of internally calibrating the spin diffusion coefficient using spin diffusion data and intrinsic distances appropriate for the sample[66;77]. This approach will be followed in this work as it contains obvious advantages in that experimental data from other sources is unnecessary and the calculated diffusion coefficient is appropriate for the sample of interest under the conditions used in the experiment. This is especially important when using MAS

because sample spinning is known to average dipolar couplings and therefore reduce the rate of spin diffusion[52;55;73]. Literature values for the diffusion coefficients acquired in studies carried out at low MAS rates are unlikely to be appropriate for the analysis of our results carried out in the fast MAS regime and an internal calibration is necessary.

4.1 The Initial Rate Approximation

This section contains a brief overview of the derivation of an expression for domain size using an initial rate approximation. For full details the relevant literature should be consulted[46;71].

In the initial rate approximation only the spin diffusion behaviour at short mixing times is considered. The diffusion process can then be described as one dimensional irrespective of the phase structure of the sample as only a small amount of magnetisation from the source has reached a small portion of the sink region. In the case of one dimensional diffusion with constant diffusivity Fick's second law (Equation 4.1) simplifies as follows,

$$\frac{\partial m}{\partial t} = D\left(\frac{\partial^2 m}{\partial x^2}\right). \tag{4.2}$$

Solutions to the diffusion equation can be obtained for a variety of initial and boundary conditions. For example, it is possible to model a lamellar system using an infinite array of alternating layers and then use this model to fit experimental data[46]. However, initial stages of spin diffusion period can be modelled as a semi-infinite source and sink as in the initial region the effects of the finite sizes of the domains are unlikely to be pronounced. An appropriate

solution is shown below.

$$m(x,t) = \frac{1}{2} m_o \operatorname{erfc}\left(\frac{x}{\sqrt{4Dt_m}}\right) \tag{4.3}$$

Where m_o is the total magnetisation and the interface between the two phases occurs at $x = 0$ and the x co-ordinate runs perpendicular to the interface. In the following discussion the source phase will be labelled A and is taken to be the dispersed phase. The sink phase will be labelled B.

The expected intensity of magnetisation within phase B, I_B, depends on the total surface area of the interface between the phases (S^{tot}_{A-B}) and at short mixing times it can then be calculated by evaluating the following integral,

$$I_B \approx S^{tot}_{A-B} \int_0^\infty \frac{1}{2} m_o \operatorname{erfc}\left(\frac{x}{\sqrt{4Dt_m}}\right) \tag{4.4}$$

$$I_B \approx S^{tot}_{A-B} m_o \sqrt{Dt_m/\pi}. \tag{4.5}$$

When the magnetisation has fully equilibrated the expected value for the signal intensity in the region B can be calculated as follows,

$$I_B(t_m \to \infty) = m_o f_B f_A V^{tot}. \tag{4.6}$$

Where f_A and f_B are the volume fractions of phase A and B respectively and V^{tot} is the total volume. At the mixing time obtained by extrapolating the initial rate out to the time taken for full equilibration, defined as $\sqrt{t^*_m}$, the values of $I_{B(t_m \to \infty)}$ and I_B are equal therefore $\sqrt{t^*_m}$ characterises the volume per interfacial area of the sample.

$$S^{tot}_{A-B} m_o \sqrt{Dt^*_m/\pi} = m_o f_B f_A V^{tot} \tag{4.7}$$

$$\frac{V^{tot}}{S^{tot}_{A-B}} = \frac{1}{f_B f_A}\sqrt{Dt^*_m/\pi} \tag{4.8}$$

The ratio of the volume and interfacial area is also related to the phase structure of the sample and depends on the length of the dispersed phase d_A and the sample morphology ϵ (ϵ=1 for lamellar, ϵ=2 for cylindrical and ϵ=3 for spherical) as follows,

$$\frac{V^{tot}}{S^{tot}_{A-B}} = \frac{d_A}{2\epsilon f_A}. \tag{4.9}$$

This can be used to relate the value of $\sqrt{t^*_m}$ obtained using the initial rate approximation to the size of the dispersed phase d_A providing that the morphology is known.

$$d_A = \frac{\epsilon}{f_B}\sqrt{4Dt^*_m/\pi} \tag{4.10}$$

The size of the long period, d_l, (the sum of the domain sizes of phase A and phase B) can be calculated according to the following equation,

$$d_l = \frac{d_A}{\sqrt[\epsilon]{f_A}}. \tag{4.11}$$

The entirety of the above analysis assumes that the diffusion behaviour is the same in both phases. For di-block polymers this is not generally true and the proton densities and the diffusion coefficients typically vary between the phases. In this scenario an extended version of Equation 4.10 must be used that accounts for these differences.

$$d_A = \left(\frac{\rho_A f_A + \rho_B f_B}{f_A f_B}\right)\frac{4\epsilon f_A}{\sqrt{\pi}}\frac{\sqrt{D_A D_B}}{\sqrt{D_A}\rho_A + \sqrt{D_B}\rho_B}\sqrt{t^*_m} \tag{4.12}$$

Where ρ_A and ρ_B and D_A and D_B are the proton densities and diffusion coefficients of phases A and B respectively. In systems with very similar proton densities Equation 4.10 can still be used by substituting the value of D for

an effective diffusion coefficient D_{eff} which is the geometric average of the diffusion coefficients of the two phases.

$$\sqrt{D_{eff}} = \frac{2\sqrt{D_A}\sqrt{D_B}}{\sqrt{D_A} + \sqrt{D_B}} \tag{4.13}$$

4.2 Domain Sizes of Diblock Polymers

The macroscopic properties of block-copolymers are governed by factors pertaining to their microscopic structure, such as the domain size of the phase separated blocks. Therefore, synthetic methods that can produce block-copolymers containing domains with certain characteristic sizes and morphologies are desirable. This necessitates the use of instrumental methods to provide measurements of the polymer domain sizes.

A range of diblock polymers have been synthesised using a novel method[78;79] that involves the use of supercritical CO_2 as a green solvent. The domain sizes of these polymers were measured using solid state NMR with fast magic angle spinning. The samples studied included;
poly(methyl methacrylate)-b-polystyrene, (PMMA-b-PS)
poly(methyl methacrylate)-b-poly(benzyl methacrylate), (PMMA-b-PBzMA)

4.2.1 Materials

Polymer samples of PMMA-b-PS and PMMA-b-PBzMA and the constituent homopolymers were all synthesised in supercritical carbon dioxide at a pressure of 275 bar and a temperature of 60 °C according to previously published methods[78;79]. The diblock polymer volume fractions, determined from solution state NMR spectra, and the sample morphologies, obtained from TEM (Transmission Electron Microscopy) images, were also supplied. The domain

Sample	PMMA/PS M_n (kDa)	Total M_n (kDa)	f_{MMA}	Morphology	d_l (nm) SAXS	d_l (nm) TEM
1A	22.5 / 37.5	60	0.373	lamellar	37	33
1B	30 / 30	60	0.494	cylindrical	39	35
1C	37.5 / 22.5	60	0.623	spherical	39	41
1D	45 / 15	60	0.719	spherical	25	44
1E	37.5 / 62.5	100	0.358	lamellar	54	48
1F	50 / 50	100	0.499	spherical	62	76
1G	62.5 / 37.5	100	0.624	spherical	49	55
1H	75 / 25	100	0.775	spherical	46	55

Table 4.1: Data supplied for PMMA-b-PS polymers.

Sample	PMMA/PBzMA M_n (kDa)	Total M_n (kDa)	f_{MMA}	Morphology
2A	22.5 / 37.5	60	0.39	lamellar/none
2B	30 / 30	60	0.51	lamellar/none
2C	37.5 / 22.5	60	0.61	lamellar/cylindrical
2D	37.5 / 62.5	100	0.38	lamellar/none
2E	62.5 / 37.5	100	0.64	lamellar/bicontinuous
2F	75 / 25	100	0.78	spherical/none

Table 4.2: Data supplied for PMMA-b-PBzMA polymers.

sizes of a number of the polymers had already been measured using SAXS and TEM and could be used as a comparison to the NMR results. Tables 4.1 and 4.2 display the relevant data for the diblock polymers.

Figure 4.1 shows TEM images of two different PMMA-b-PS samples, one with a lamellar and the other with a spherical morpholgy. The TEM images of all of the PMMA-b-PS samples displayed a good degree of phase separation and only sample 1D showed any evidence of disorder. The ability of a block copolymer to form distinct polymer domains is governed by the product χN, which must exceed 10.5 for phase separation to occur[80]. χ is the Flory-Huggins parameter which characterises the energy of interaction of the two polymer

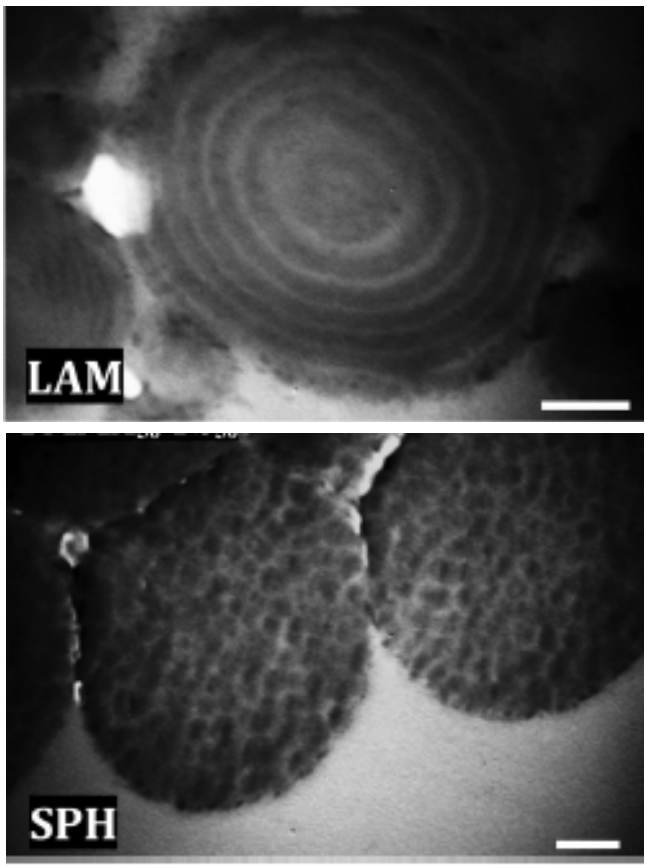


Figure 4.1: TEM images of PMMA-b-PS samples 1A (top) with a lamellar morphology and 1F (bottom) with a spherical morphology. The white scale bar in the images is 200 nm.

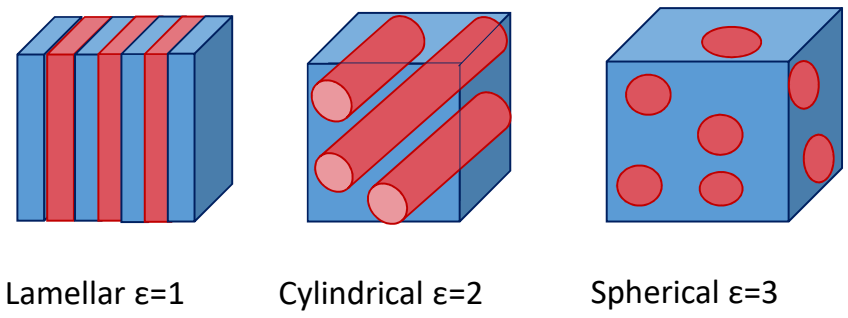


Figure 4.2: Pictorial representation of the morphologies observed in the diblock polymers

chains (and is positive where the interaction is repulsive and negative when mixing is favourable) and N is the degree of polymerisation. Figure 4.2 shows a representation of the different morphologies displayed by the diblock polymers.

In contrast to the PMMA-b-PS polymers the PMMA-b-PBzMA polymers displayed more disorder and weaker phase separation. This can be seen in Figure 4.3 that shows two TEM images of sample 2B. In one of the images there is a clear lamellar morphology while the other shows no discernible phase separation.

The observed morphologies of the PMMA-b-PS samples are particularly interesting because they deviate from the expected values[80]. In general, the morphology depends on the relative volume fraction and can be estimated based on the following inequalities[81];

$0.35 < fa < 0.5$ - lamellar morphology

$0.15 < fa < 0.4$ - cylindrical morphology

$fa < 0.2$ - spherical morphology.

Phase diagrams for both the PMMA-b-PS samples and the PMMA-b-PBzMA samples are displayed in Figure 4.4. For the PMMA-b-PBzMA samples the observed morphologies correspond roughly to the expected outcome on the basis of the relative volume fractions of the two blocks. However, for the PMMA-b-PS the regions in the phase diagram corresponding to the various morphologies appear shifted with respect to the volume fraction. Significant deviations from the expected phase structure can also be observed in Table 4.1. The fact that some of the PMMA-b-PS samples show unexpected morphologies was attributed to differential swelling of the polymer blocks in supercritical carbon dioxide occurring during the synthesis[80;82].

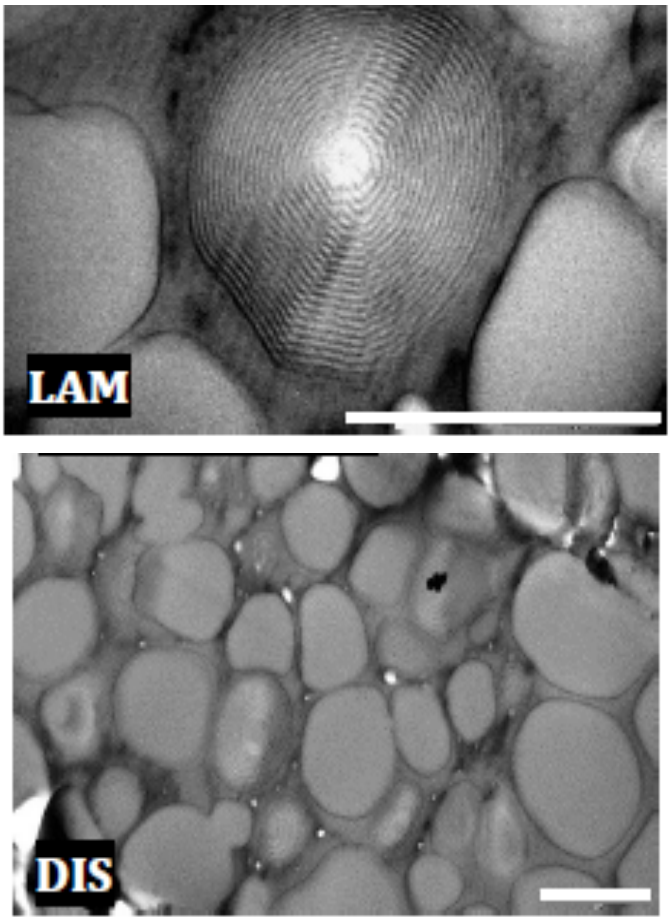


Figure 4.3: TEM images of PMMA-b-PBzMA sample 2B with a lamellar morphology (top) and with a disordered amorphous structure (bottom). The white scale bar in the images is 1 μm.

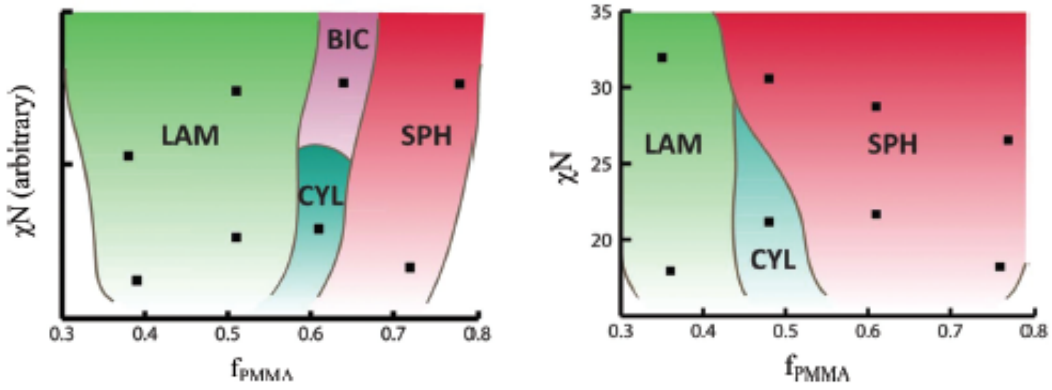


Figure 4.4: Phase diagrams constructed on the basis of TEM images for the PMMA-b-PBzMA polymers (left) and PMMA-b-PS samples (right). The scale of the y axis in the PMMA-b-PBzMA plot is arbitrary because no χ interaction parameter is available for this system.

4.2.2 Experimental Method

All NMR data were acquired on a Bruker Avance III spectrometer operating at 600.13 MHz using a 1.3 mm HX probe. A simple three pulse sequence for exchange spectroscopy of the form $90_x - t_1 - 90_x - t_m - 90_x$, including a ±z-alternation phase cycle on one of the pulses prior to the mixing period, was used to acquire ^{1}H-^{1}H spin diffusion spectra. TPPI (Time Proportional Phase Incrementation) processing was used and 2048 by 256 complex data points were acquired in t_2 and t_1 respectively. All the spectra of the block-copolymer samples were recorded using a spinning rate of 60 kHz and a 50 ppm spectral width in both dimensions. To obtain a complete diffusion profile between thirteen and seventeen 2D spectra were acquired for each sample using mixing times that ranged between 0.001 and 0.7 s. The relaxation delay used was set to at least three times the T_1 and was generally between 5-7 s depending on the sample. For a relaxation delay of 5 s the total acquisition time for a single 2D ^{1}H-^{1}H spin diffusion spectrum was around three hours. All the spectra of the di-block polymers were recorded with the temperature of the VT gas set to 298 K.

Deconvolution of the spectra was carried out in Matlab by fitting 16 2D peaks (PMMA-b-PS) or 9 2D peaks (PMMA-b-PBzMA) to the data surface using a fixed peak shape and peak position and a varying peak width and height. Intensities were obtained by taking the volume integrals of the fitted peaks. These were corrected for T_1 relaxation during the mixing time and then normalised against the total magnetisation, taken from fitted spectra recorded with low mixing times.

T_1 values were recorded for all the samples in separate saturation-recovery experiments. 1D spectra were also recorded to obtain the expected equilibrium

Monomer Unit	Distance Used	Average Distance (nm)
Methyl Methacrylate	methyl-methoxy	0.56
Styrene	aromatic-aliphatic	0.50
Benzyl Methacrylate	methyl-methoxy	0.51
Benzyl Methacrylate	aromatic-methoxy	0.45
Benzyl Methacrylate	aromatic-methyl	0.72

Table 4.3: Characteristic distances of polymer repeating units.

magnetisation levels. These were deconvoluted in Matlab using fixed peak shapes, peak widths and peak positions while varying the height during the fitting procedure.

Spectra of the PMMA, PBzMA and PS homopolymers were also acquired using the same experimental procedure as for the diblock polymer samples. Spectra were acquired at 60 kHz MAS rate with the spectral width set to 50 ppm in both dimensions. Typical mixing times used varied from between 0.0005 to 0.1 s.

The spectra were deconvoluted by fitting four peaks to the data surface in the case of PMMA and PS and nine peaks in the case of PBzMA. A fixed peak shape and peak position was used and the peak width and height were varied. The peak intensities were obtained by taking the volume integrals of the fitted peaks and these were normalised to the total magnetisation present in the spectrum. The T_1 values of different sites within each of the homopolymers were very similar and therefore no T_1 correction was required.

In order to calculate a diffusion coefficient a distance measurement related to diffusion within a domain is required for each polymer. These distances were obtained by geometry optimising the appropriate repeating unit in QChem[83], using B3LYP and a 6-31G** basis set. Table 4.3 shows the calculated distances

between various proton sites within the repeating unit.

4.2.3 Results and Discussion

Figure 4.5 shows three ^{1}H-^{1}H spin diffusion spectra of sample 1B recorded with increasing mixing time. Three distinct peaks can be observed in the spectra. The peak at ca. 7 ppm corresponds to the aromatic protons in the polystyrene block of the polymer, the peak at ca. 4 ppm corresponds to the methoxy protons in the PMMA block of the polymer and the peak between 0-2 ppm corresponds to aliphatic protons from the polymer backbone. There is also a sharp, truncated peak that appears at ca. 0 ppm. This signal does not originate from the block-copolymer but is due to the presence of poly(dimethylsiloxane) that is used as a solubiliser during the synthesis. This site was omitted when fitting the spectra and determining polymer domain sizes.

At short mixing times the majority of the magnetisation is present along the diagonal. At longer mixing times increases in the cross peak intensity were observed. Cross peaks initially form between the polystyrene aromatic protons and the aliphatic protons and between the methoxy protons on the PMMA and the aliphatic protons. This is indicative of magnetisation transfer within the respective domains of the block-copolymer. Eventually, if sufficient time is allowed for spin diffusion to take place a cross peak can be observed between the PS aromatic and PMMA methoxy peaks indicating inter-domain magnetisation transfer.

A one-dimensional ^{1}H spectrum of the same sample is displayed in Figure 4.6. Four fitted Gaussian/Lorentzian peaks shapes used to determine the expected

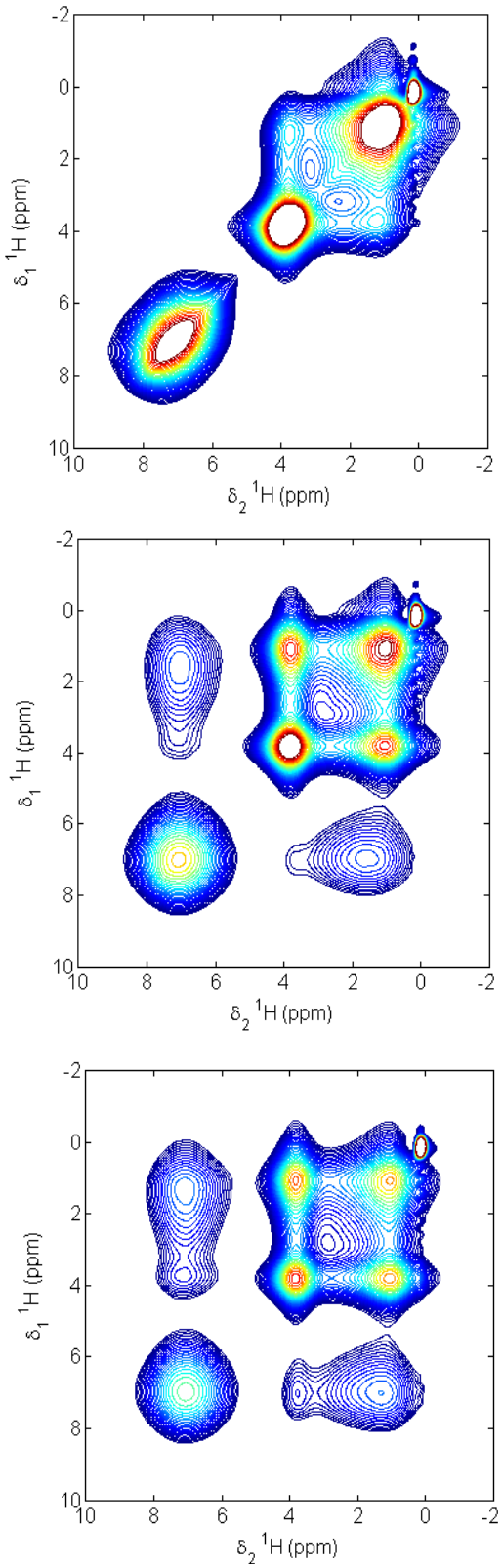


Figure 4.5: ^{1}H-^{1}H spin diffusion spectra of sample 1B recorded with mixing times of 0.0025 s (top), 0.025 s (centre) and 0.2 s (bottom).

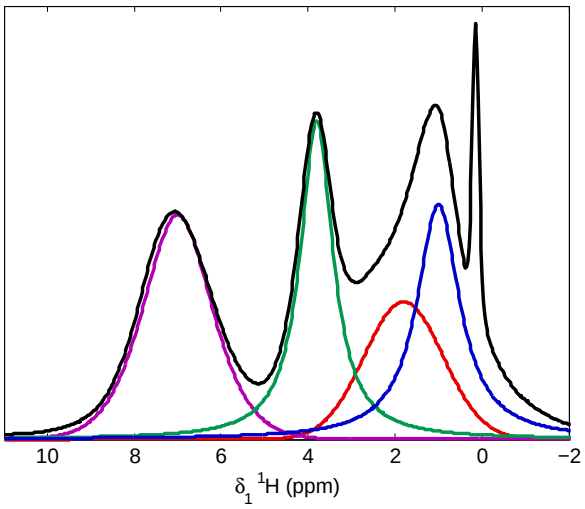


Figure 4.6: ^{1}H NMR spectrum of sample 1B with four fitted mixed Gaussian/Lorentzian peaks.

equilibrium magnetisation ratio of the different proton environments are also displayed. Two-dimensional versions of these peak shapes were used to fit the ^{1}H-^{1}H spin diffusion spectra (see Figure 4.5) for the full range of mixing times.

Figure 4.7 shows a plot of the magnetisation decay of the PS aromatic peak on the diagonal from the 1B sample with increasing mixing time. This decay had two linear regions, the first corresponded to spin diffusion within a polymer domain and the second corresponded to inter-domain spin diffusion. The upper horizontal red line in the plot divides these two regions and the mixing time at this point, denoted $t_{m1}^{*1/2}$, was taken to correspond to full equilibration between the PS aromatic protons and PS aliphatic protons. The lower horizontal red line indicates the expected equilibrium magnetisation based on the relative peak intensities present in the 1D spectrum. By extrapolating the fit of the second decaying region out to this lower line a second value of $t_m^{*1/2}$ can be obtained, given as $t_{m2}^{*1/2}$. This value represents the time taken for full equilibration of magnetisation between the PS and PMMA domains

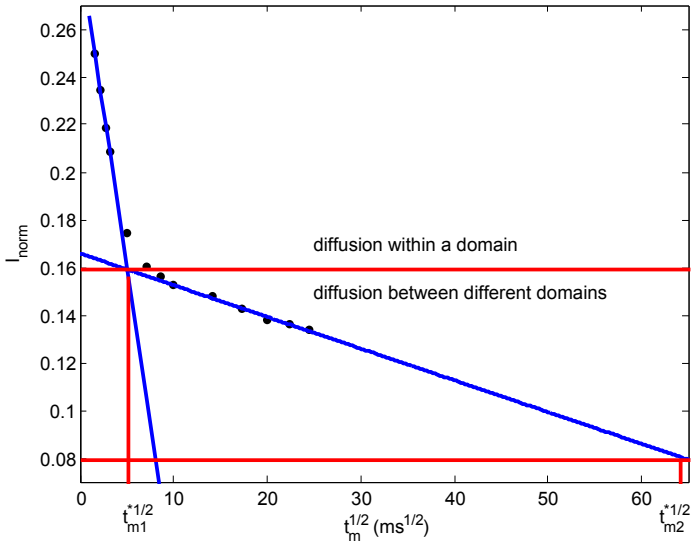


Figure 4.7: Decay of intensity of the diagonal aromatic peak of sample 1B with increasing mixing time.

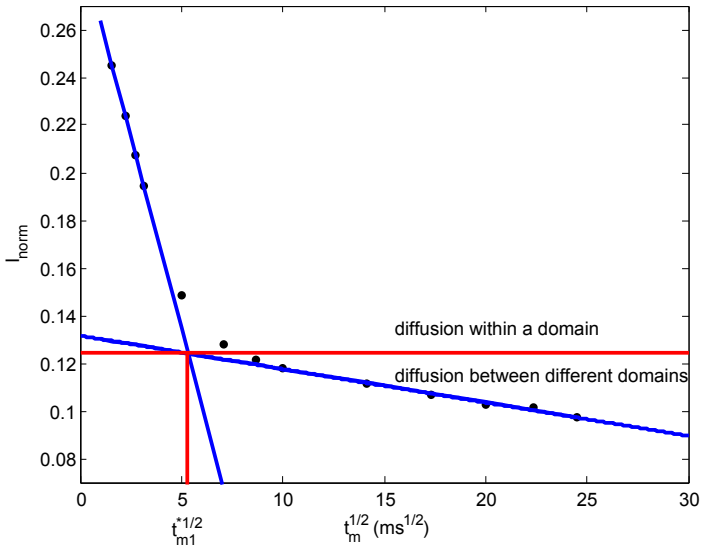


Figure 4.8: Decay of intensity of the diagonal methoxy peak of sample 1B with increasing mixing time.

of the block-copolymer. The diffusion coefficient for the PS domain of the block-copolymer was calculated according to Equation 4.14 below using the

$t_{m1}^{*1/2}$ value and $x = 0.50$ nm[66;77].

$$D = \frac{\pi x^2}{4t_{m1}^*} \tag{4.14}$$

To obtain the diffusion coefficient for the PMMA domain the procedure was repeated using a distance of 0.56 nm and a $t_{m1}^{*1/2}$ value taken from the decay of the PMMA diagonal methoxy peak (see Figure 4.8). This decay profile can be seen in Figure 4.8. The diffusion coefficients for the two domains were averaged according to Equation 4.13 to give the effective diffusion coefficient. This was inputted into Equation 4.10 along with the $t_{m2}^{*1/2}$ value to calculate a size for the smaller volume fraction domain, d_A. This was then converted into a measurement of the long period, d_l using Equation 4.11. This resulted in an NMR measured d_l value of 38 nm for this polymer. This compared well with the results of SAXS and TEM measurements which were 39 nm and 35 nm respectively.

The experiment was repeated on the seven other PMMA-b-PS polymers and the resulting diffusion profiles are displayed in Appendix A. Table 4.4, shows the internally calibrated diffusion coefficients and both the d_A and d_l values of all of the PMMA-b-PS samples. The NMR d_l values for all the samples are comparable to the domain sizes as measured by SAXS and TEM.

Sample	D_{PS} (nm^2ms^{-1})	D_{PMMA} (nm^2ms^{-1})	D_{eff} (nm^2ms^{-1})	d_A NMR (nm)	d_l NMR (nm)	d_l SAXS (nm)	d_l TEM (nm)
1A	0.0068 (±0.0022)	0.0095 (±0.0021)	0.0080 (±0.0035)	9 (±2)	24 (±6)	37	33
1B	0.0078 (±0.0010)	0.0087 (±0.0007)	0.0082 (±0.0013)	26 (±3)	38 (±4)	39	35
1C	0.0072 (±0.0010)	0.0098 (±0.0012)	0.0084 (±0.0017)	24 (±3)	33 (±4)	39	41
1D	0.0085 (±0.0009)	0.0126 (±0.0047)	0.0102 (±0.0045)	20 (±5)	30 (±7)	25	44
1E	0.0076 (±0.0016)	0.0090 (±0.0012)	0.0083 (±0.0023)	18 (±4)	50 (±10)	54	48
1F	0.0078 (±0.0011)	0.0077 (±0.0015)	0.0077 (±0.0021)	48 (±8)	60 (±10)	62	76
1G	0.0070 (±0.0010)	0.0094 (±0.0034)	0.0081 (±0.0036)	29 (±7)	41 (±10)	49	55
1H	0.0069 (±0.0013)	0.0083 (±0.0010)	0.0076 (±0.0019)	25 (±4)	41 (±7)	46	55

Table 4.4: Table showing the diffusion coefficients and domain sizes of all the PMMA-b-PS diblock polymers.

Sample	D_{eff} (nm^2ms^{-1})	d_A NMR (nm)	d_l NMR (nm)
2A	0.008 (±0.0008)	10 (±2)	26 (±3)
2B	0.008 (±0.0008)	9 (±1)	18 (±2)
2C (lamellar)	0.008 (±0.0008)	7 (±1)	18 (±2)
2C (cylindrical)	0.008 (±0.0008)	14 (±2)	22 (±3)
2D	0.008 (±0.0008)	8 (±1)	21 (±3)
2E	0.008 (±0.0008)	12 (±3)	34 (±7)
2F	0.008 (±0.0008)	none	none

Table 4.5: Table showing the domain sizes of all the PMMA-b-PBzMA diblock polymers. The diffusion coefficient used for all the samples was calculated based upon the results from homopolymers of PMMA and PBzMA.

These experiments were also repeated on all the samples of PMMA-b-PBzMA and the results are displayed in Table 4.5. From the TEM images it was not possible to determine if sample C had cylindrical or lamellar phases and so the domain size was calculated twice for each possible scenario.

Figure 4.9 shows three ^{1}H-^{1}H spin diffusion spectra recorded at a range of mixing times for sample 2B. The PBzMA domain of these PMMA-b-PBzMA samples contains aliphatic, methoxy and aromatic protons and so at intermediate mixing times (for example 0.025 s) the full range of cross peaks can be observed. The presence of methoxy protons in the same domain as the aromatic protons results in a few differences in the analysis of the results of these polymers. Firstly, the presence of inter-domain diffusion can only be clearly observed by tracking the changes in the decay of the PBzMA aromatic peak. This is displayed in Figure 4.10 for sample 2B and the diffusion profiles for the remaining samples are presented in Appendix B. As before the polymer domain size is calculated on the basis of the $t_{m2}^{*1/2}$ extracted from the extrapolation of the fit of the second shallower decaying region to the equilibrium level of magnetisation. Secondly, internal calibration of the spin diffusion coefficient cannot be carried out on these polymers.

In order to carry out the internal calibration it is necessary to have a unique site in each block of the polymer. This is not the case in the PMMA-b-PBzMA polymers as the methoxy and aliphatic resonances from the PMMA block overlap with resonances from the PBzMA domains. As an alternative to carrying out the internal calibration the average of the diffusion coefficients of the two homopolymers (PMMA and PBzMA), obtained under the same experimental conditions, was used.

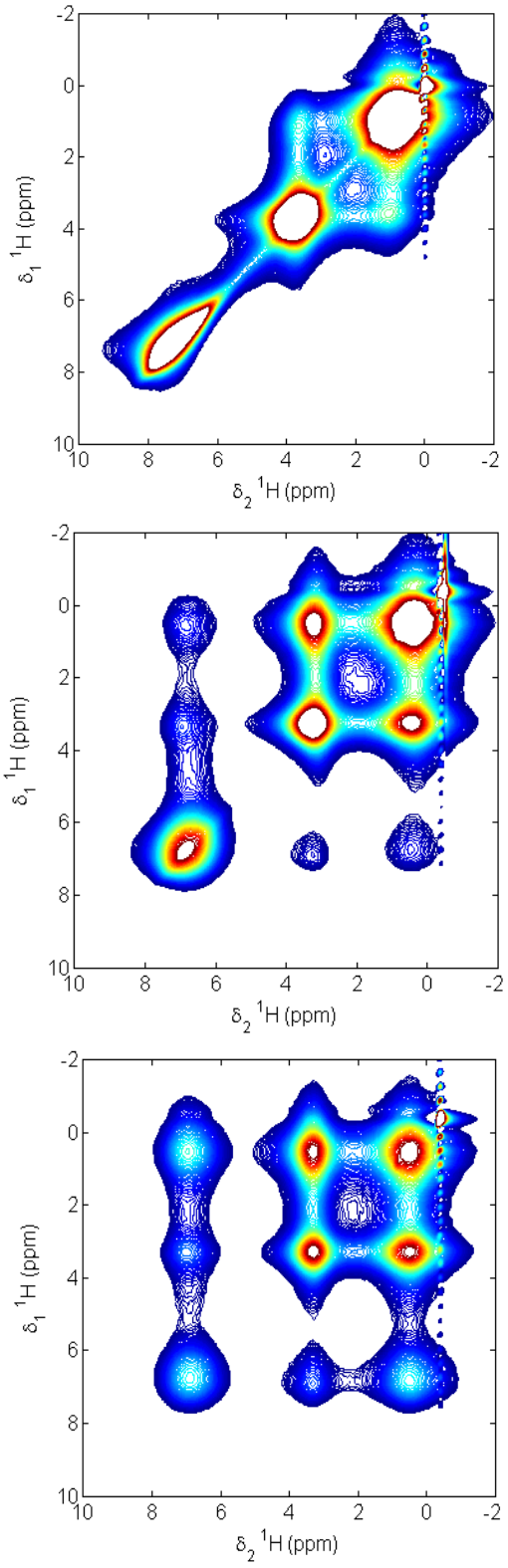


Figure 4.9: ^{1}H-^{1}H spin diffusion spectra of sample 2B recorded with mixing times of 0.0025 s (top), 0.025 s (centre) and 0.2 s (bottom).

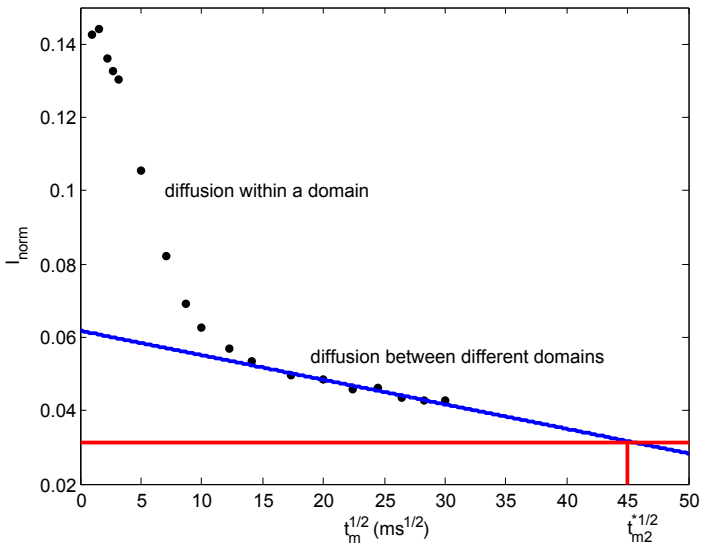


Figure 4.10: Decay of intensity of the diagonal aromatic peak of sample 2B with increasing mixing time

However, the use of the homopolymer diffusion coefficients may actually have been more appropriate for the analysis of the PMMA-b-PBzMA polymers. The blocks of the PMMA-b-PBzMA are generally more miscible than the PMMA-b-PS blocks and so typically display a lower level of phase separation. This is demonstrated in Table 4.2, where none listed under morphology signifies that the samples appeared partially amorphous in TEM images (Figure 4.3 contains TEM images showing amorphous regions of a PMMA-b-PBzMA sample). In a partially phase separated sample the initial steep decay would probably contain contributions from the poorly phase separated portions of the sample and would therefore be less suitable as a calibration.

Sample 2F was so poorly phase separated that no second decay corresponding to inter-domain magnetisation transfer was observed in its spin diffusion profile and instead a plateau was reached (see Figure 4.11). This suggests that the amount of phase separated material in the sample was so low that it was below the detection limit. It was therefore not possible to calculate a domain size for

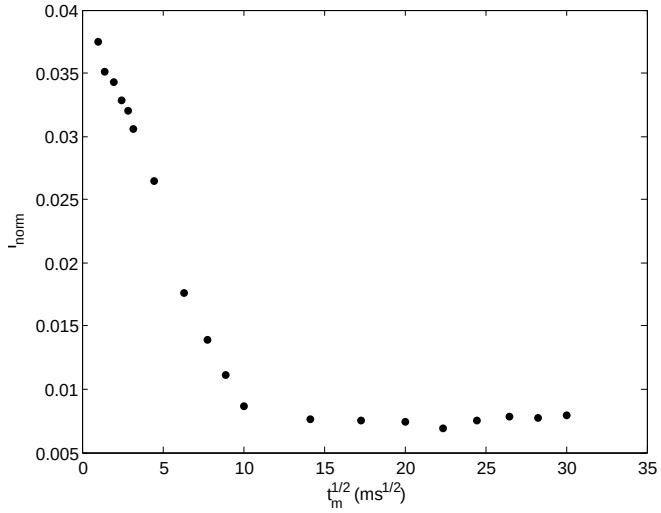


Figure 4.11: Decay of intensity of the diagonal aromatic peak of sample 2F with increasing mixing time. The second decay corresponding to inter-domain spin diffusion is not observed.

sample 2F.

TEM and SAXS measurements of the domain size of the PMMA-b-PBzMA polymers have only been carried out on samples 2B and 2C to date. For sample 2B SAXS returned a value of the long period of 31 nm and TEM gave a value of 22 nm. For sample 2C the values obtained from SAXS and TEM were 31 and 26 nm respectively. For these two samples the TEM measured domain sizes were comparable to the NMR values. The results from SAXS were generally slightly larger than the NMR results but this may be due to the presence of more amorphous material due to the increased miscibility of the domains.

The errors quoted in Tables 4.4 and 4.5 (in brackets) are obtained by using the 95% prediction bounds of the fitted lines. They also incorporate the effect of the error in the T_1 values that were obtained from a single exponential fit of the results of the saturation-recovery experiment. The errors associated with the SAXS and TEM results are unknown.

The spin diffusion coefficients of these polymers are greatly reduced in comparison to values reported at lower spinning speeds. A diffusion coefficient of 0.8 nm^2 ms^{-1} at 4 kHz MAS rate has previously been quoted[46]. More recently values of 0.2-0.3 nm^2 ms^{-1} were obtained directly from NMR data using a sample of PS at spinning rates between 2-5 kHz[73]. A large reduction in the diffusion coefficient on moving to faster MAS rates would be expected due to more effective averaging of the dipolar couplings.

It was necessary to apply a T_1 correction of the form $exp(t_m/T_1)$ to the diffusion profiles to take into account loss of magnetisation occurring during the mixing time. The application of T_1 corrections to spin diffusion data has previously been a source of contention[74;75] and corrections of this sort are only strictly valid if the T_1 is homogeneous throughout the sample.[71;75]. The T_1 values for all sites in all of the polymers were between 0.9-2.1 s and the differences in T_1 between different sites within the same polymer were all below 1 s (see Appendices A and B). It is expected that the use of the initial rate approximation with a back correction will introduce an additional source of error into the results and in other systems where the variation in T_1 is larger this approximation would become increasingly less valid. In the following section the effect that this variation in T_1 has on the calculated domain size will be assessed.

4.3 T_1 Relaxation in Spin Diffusion Experiments

In general, the changes in magnetisation resulting from the spin diffusion process and from T_1 relaxation are hard to separate. For example, during the

mixing time of a spin diffusion experiment carried out on the block copolymers, magnetisation is lost due to T_1 relaxation at the same time as it is re-distributed through spin diffusion. Furthermore, the loss of magnetisation due to T_1 relaxation in a saturation-recovery experiment is modified by the presence of spin diffusion between the blocks and this is incorporated into the experimentally obtained T_1 value. There is a complicated interplay between these two processes and using a T_1 value obtained from a saturation-recovery experiment in an exponential back-correction may not fully compensate for changes due to spin lattice relaxation.

There is experimental evidence that suggests that the effects of T_1 relaxation may not be fully accounted for by the use of the back-correction. The domain sizes obtained in Table 4.4 were calculated using the decay of the diagonal PS aromatic proton peak as this was the most well resolved site in the spectrum. However, as the spectra are deconvoluted in order to obtain the peak intensities, it should be equally possible to carry out the same analysis using the decay of the diagonal PMMA methoxy protons. As the process of spin diffusion from the PS block to the PMMA block and spin diffusion from the PMMA to the PS block should be equivalent the domain sizes calculated using the decay of both these peaks should be the same. Table 4.6 shows the size of the long period d_l calculated using these two different peaks and their arithmetic average. A similar trend in the domain sizes is produced whichever peak is used but the calculated domain sizes are not equivalent. Using the decay of the PMMA methoxy protons generally results in a smaller calculated domain size than when the decay of the PS aromatic protons is used. The source of this discrepancy could be the result of using the T_1 values obtained from saturation-recovery experiments to back-correct the diffusion profiles.

Sample	d_l (nm) calculated from PS peak	d_l (nm) calculated from PMMA peak	d_l (nm) average	d_l (nm) SAXS	d_l (nm) TEM
1A	24	21	23	37	33
1B	38	24	31	39	35
1C	32	28	30	39	41
1D	30	24	27	25	44
1E	50	30	40	54	48
1F	60	45	53	62	76
1G	41	27	34	49	55
1H	41	62	52	46	55

Table 4.6: PMMA-b-PS domain sizes calculated using the decay of the PS aromatic peak, the PMMA methoxy peak and the average of these two results. The domain sizes obtained from SAXS and TEM are included as a comparison.

It would be useful to obtain a T_1 value that could be successfully used in a back-correction to the initial rate approximation to fully remove the effect of relaxation and two alternative methods of back-correcting the experimental data were attempted. In the first case the average of all the T_1 values recorded experimentally in the saturation-recovery experiments on each diblock polymer was used. The results of this are displayed in Table 4.7. In the second case the T_1 values obtained from the PS and PMMA homopolymers were used (2.451 s for the PS and 0.882 s for PMMA) to back-correct the experimental data. These results are given in Table 4.8. The homopolymers are synthesised following the same method as the diblock polymers and their T_1 values may be a reasonable estimate of the T_1 values expected for the two domains of the diblock polymer in the absence of any spin diffusion between the domains.

It is apparent from the results displayed in Tables 4.7 and 4.8 that the use of either the homopolymer T_1 values or a sample average T_1 fails as a correction method. The values obtained show little resemblance to the SAXS and TEM results and in many cases physically unrealistic domain sizes are obtained (such

Sample	d_l (nm) calculated from PS peak	d_l (nm) calculated from PMMA peak
1A	70	16
1B	93	18
1C	44	20
1D	35	20
1E	-53	18
1F	7708	20
1G	72	18
1H	70	23

Table 4.7: Domain sizes obtained through back-correction of the decay of the PMMA methoxy peak and the PS aromatic peak using a sample average T_1 value.

d_l (nm) calculated from PS peak	d_l (nm) calculated from PMMA peak
18	215
27	49
25	166
25	98
30	121
45	-242
30	-364
26	4000

Table 4.8: Domain sizes obtained through back-correction of the decay of the PMMA methoxy peak and the PS aromatic peak using the T_1 values of the homopolymers.

as very large numbers and negative numbers). Using the T_1 values, obtained from saturation-recovery experiments, in a back correction gives physically realistic results for the domain sizes in all cases so on that basis alone it may be considered a superior approach. Simulations were carried out in order to further investigate how differences in T_1 values between the polymer domains affect the calculated domain size.

Although the effect of T_1 relaxation in spin diffusion experiments has previously been studied using numerical simulations this has mainly been carried out using diffusion coefficients applicable at low spinning rates. The effect of fast MAS in the experiments involving the diblock polymers was to reduce the diffusion coefficients but lengthen the T_1 time and the subsequent simulations will incorporate these changes. A description of how a suitable simulation may be set-up is given in the subsequent section and the following section will

present the results.

4.3.1 Simulation of Spin Diffusion Profiles

Numerical simulations have previously been used to model the spin diffusion process and it is possible to extract domain sizes by fitting the simulated results to experimental data[51–54;68;72;73;75;76]. The following section gives a brief overview of how numerical methods can be used to solve the diffusion equation and for further details relevant texts may be consulted[67]. The construction of a simulation that was used to generate spin diffusion profiles for a lamellar system will subsequently be described.

It is possible to see how the equations used to simulate spin diffusion profiles are derived by considering Fick's first law (see Equation 4.15). This states that the rate of transfer of a diffusing substance through a unit surface area is proportional to the concentration gradient normal to that surface.

$$F = -D\frac{\delta C}{\delta x} \tag{4.15}$$

Using this equation and taking the example of a one dimensional sheet, which starts with a magnetisation gradient, it is possible to determine how the magnetisation changes with time. The sheet may be divided into smaller sections of width a and the magnetisation at the edges of each section may be labelled as m_0, m_1 and m_2. The label, m_1, can be used to represent the average magnetisation level within the region extending from the midpoint of the prior section to the midpoint of the subsequent section (corresponding to the grey box in Figure 4.12). The amount of magnetisation flowing into this region q_{in}

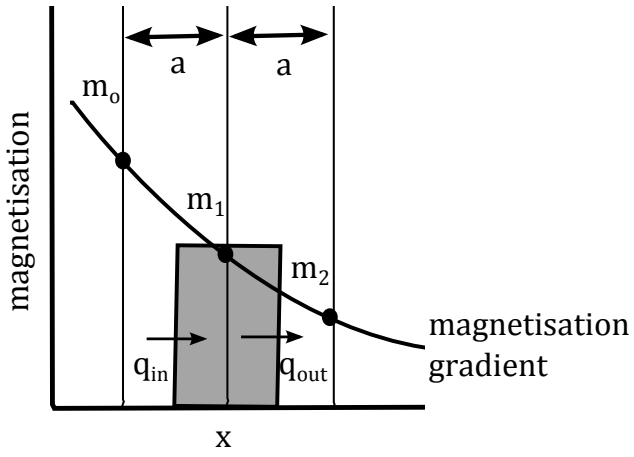


Figure 4.12: Diagram showing the transfer of magnetisation in a one dimensional sheet with a magnetisation gradient

within a short period of time τ can be given by the following equation,

$$q_{in} = -D\tau(m_1 - m_0)/a. \tag{4.16}$$

The amount flowing out q_{out} of the region within the same time period can be given as,

$$q_{out} = -D\tau(m_2 - m_1)/a. \tag{4.17}$$

Therefore the total amount of magnetisation gained within the region surrounding point m_1 can be given as follows,

$$q_{in} - q_{out} = \frac{D\tau}{a}(m_0 - 2m_1 + m_2). \tag{4.18}$$

The amount of magnetisation gained within this region can also be written as $(m_1 - m_1^{'})a$. Where $m_1^{'}$ is the concentration at the end of time period τ. Subsequently, we can write an equation for how the magnetisation changes within the region around m_1 as,

$$m_1^{'} - m_1 = \frac{D\tau}{a^2}(m_0 - 2m_1 + m_2). \tag{4.19}$$

This equation deals with magnetisation transfer in a one dimensional system where only magnetisation transfer from and to the left and the right is considered. It is possible to implement this within a computer simulation by modelling the rate of transfer between a line of equally spaced points. The results of such a simulation would be representative of spin diffusion in a block copolymer with a lamellar morphology where the magnetisation transfer between the different polymer domains is restricted to one dimension. It is possible to extend this approach to higher dimensionalities by using either a grid of points (2D) or a cube (3D). In order for the simulation to converge the following inequality must be observed,

$$\frac{D\tau}{a^2} < 0.5. \tag{4.20}$$

It is possible to simulate the effects of T_1 relaxation by incorporating an extra term into Equation 4.19 that causes a loss of magnetisation from the system (see Equation 4.21).

$$m_1^{'} - m_1 = \frac{D\tau}{a^2}(m_0 - 2m_1 + m_2) - \frac{\tau}{T_1}m_1 \tag{4.21}$$

The T_1 value used in this equation will be referred to as the intrinsic T_1. This intrinsic T_1 determines the rate of relaxation in the absence of spin diffusion and is difficult to determine experimentally.

The simulations displayed in the following section were obtained by implementing these equations in Matlab. Only the results for a one dimensional system (a lamellar diblock polymer), modelled using magnetisation transfer along a line of points, was considered. Therefore, only fits to the experimental data for samples 1A and 1E were attempted as these are the only PS-b-PMMA

samples with a lamellar morphology. The spacing between the points was set to 0.5 nm and the time step for the simulations was 5 ms. The line was divided into two blocks corresponding to a single PMMA layer and a single PS layer. Magnetisation transfer from and to the left and the right of each point was calculated in every step of the simulation. The magnetisation in the final point of the line was permitted to transfer into the initial point of the line and vice versa. This creates two effective interfaces between the blocks one positioned somewhere towards the centre of the line (the exact position varying dependent on the simulated volume fraction) and one at the start/end of the line. A single constant diffusion coefficient was used. The starting condition for the simulations of the spin diffusion experiments involved setting the magnetisation at each point in the selected block to positive, equal, numerical values and the points in the other block were assigned a value of zero. The time step was incremented until the magnetisation equilibrated between both blocks.

In order to assess the effect of T_1 relaxation it was necessary to incorporate the intrinsic T_1 values of the two blocks of the polymer into the simulation. Obtaining intrinsic T_1 values of a block copolymer is not straightforward and so for the simulations the T_1 values of the constituent homopolymers were used.

To gain an understanding of the effect T_1 relaxation has on the spin diffusion experiment a range of simulations were carried out. The total length of the line was set to between 20-70 nm and the relative lengths of the two blocks were chosen to correspond to volume fractions of 0.25, 0.375, 0.5, 0.625 and 0.75. A diffusion coefficient of 0.0083 nm^2 ms^{-1} was used. The spin diffusion process was simulated twice for each system both with and without the effects of T_1 relaxation. Figure 4.13 displays a diagram outlining the operation of the

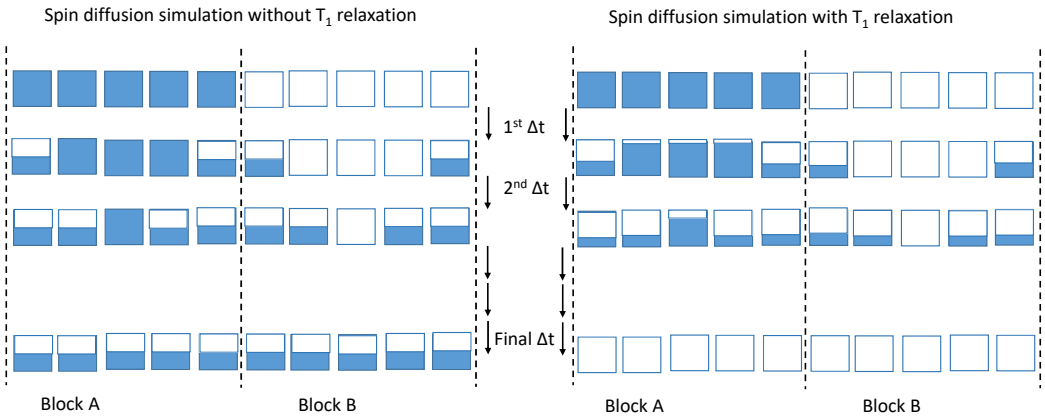


Figure 4.13: Diagram illustrating the operation of the simulation. A blue box = a point on the line with a unit of magnetisation. An empty box = a point on the line containing zero magnetisation. Δt = incrementation of the time step. Black dashed lines = boundaries between the two blocks of the diblock polymer (labelled A and B).
Left: A simulation including the effects of spin diffusion but with no T_1 relaxation. At the start of the simulation all of the magnetisation is present in the initially selected block (A in this case). In each time step the magnetisation passes through the boundaries between the blocks from block A into block B. At the end of the simulation the magnetisation is evenly distributed between the two blocks.
Right: A simulation including the effects of spin diffusion and T_1 relaxation. At the start of the simulation all of the magnetisation is present in the initially selected block (A in this case). In each time step the magnetisation passes through the boundaries between the blocks from block A into block B. However, there is also a concurrent loss of magnetisation from both of the blocks due to T_1 relaxation. At the end of the simulation the magnetisation is zero in both blocks.

spin diffusion simulations for both scenarios.

The rate of relaxation in the presence of spin diffusion was also simulated by including the intrinsic T_1 values and starting the simulation with magnetisation present in both the blocks. The resulting decays were fitted to obtain a T_1 value that incorporates the effect of spin diffusion and is therefore similar to the T_1 values that would be obtained from a saturation-recovery experiment. This simulated T_1 value was used to apply an exponential back-correction to the simulated spin diffusion profiles that incorporate the effects of T_1 relaxation.

Simulations were also compared with experimental data for lamellar samples 1A and 1E. For the simulations the experimentally calibrated effective diffusion coefficients of samples 1A and 1E (see Table 4.4) were used and the relative sizes of the blocks in the simulation were set close to the actual volume fractions of the polymer domains (see Table 4.1). The effect of T_1 relaxation was incorporated into the simulations using the homopolymer T_1 values and the results were compared to experimental spin diffusion profiles without the applied back-correction. The simulated build-up in magnetisation was compared to the experimental diffusion profile showing the build-up of cross peak intensity between the PMMA methoxy protons and the PS aromatic protons. The simulations were repeated with a range of different domain sizes to find the result that produced the best match to the experimental data.

Although, the decay of a diagonal peak was previously used to extract domain sizes using the initial rate approximation it was preferable to compare the build-up of a cross peak with simulated data for two reasons. Firstly the diagonal peak diffusion profiles consist of two decays corresponding to intra and inter domain diffusion (as well as an overall loss of magnetisation due to T_1 effects) this means that the results of two separate simulations would have to be combined to reproduce the shape of this profile. Only inter-domain spin diffusion and T_1 relaxation contribute to the intensity of the cross peak between the PS aromatic and PMMA methoxy protons and so its behaviour is simpler to simulate. Secondly the simulations require an accurate starting point for the initial magnetisation. For a build-up there is only one realistically feasible value for the starting magnetisation (0) whereas the starting point of a decay would incorporate any errors that arise from fitting the experimental data and may be open to more interpretation.

4.3.2 Results from Simulated Diffusion Profiles

Figures 4.14 and 4.15 show the results of simulated spin diffusion experiments for a model system where the total length of the domain size was set to 40 nm and the volume fraction of PMMA was 0.375. Figure 4.14 starts with magnetisation selected in the PS domain and Figure 4.15 starts with magnetisation selected in the PMMA phase. In both cases the simulation carried out without T_1 relaxation shows a plateau at the expected equilibrium magnetisation level. Using the initial rate approximation to extract domain sizes from the fit to this diffusion profile results in the expected value ($\approx$ 40 nm) no matter which domain was initially selected.

Simulations were also carried out which incorporated the effects of T_1 using the homopolymer T_1 values as an estimate of the intrinsic T_1. These simulations are also displayed in Figures 4.14 and 4.15 and instead of reaching a plateau these curves decay to zero as all the magnetisation was eventually lost via spin lattice relaxation. These decays were back-corrected using simulated T_1 values for the same system which incorporate the effects of both relaxation and spin diffusion.

The results of applying the back-correction to the simulation including T_1 relaxation with the magnetisation starting in the PS domain is displayed in Figure 4.14. The back-corrected curve does not overlay with the simulation carried out in the absence of any T_1 relaxation and the fit to this curve produces a larger $t_m^{*1/2}$ value and therefore a larger domain size ($\approx$ 61 nm). The converse effect can be observed in Figure 4.15 where the magnetisation starts in the PMMA domain. The back-corrected curve produces a smaller $t_m^{*1/2}$ value and therefore a smaller domain size ($\approx$ 29 nm). The arithmetic average of these two results ($\approx$ 45 nm) is closer to the actual domain size.

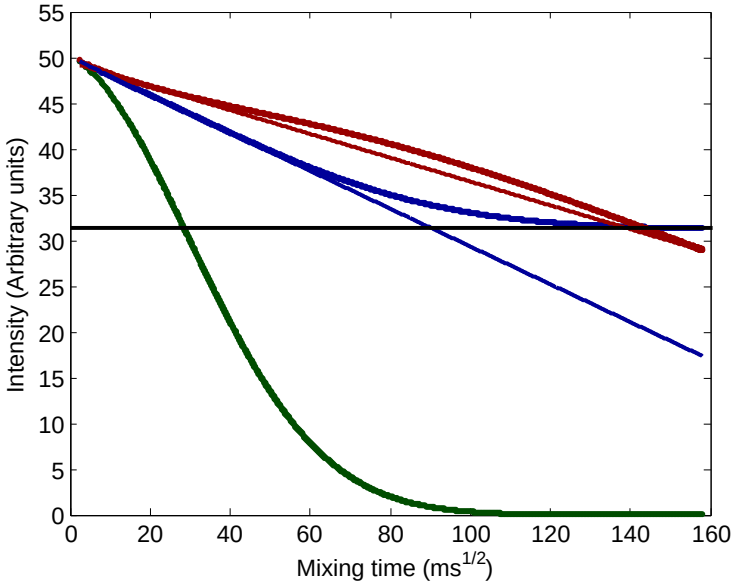


Figure 4.14: Simulated diffusion profiles for a lamellar PMMA-b-PS diblock polymer with a total domain size of 40 nm, a PMMA volume fraction of 0.375 and with the magnetisation starting in the PS domain. Blue Curve: Results without including T_1 relaxation. Green Curve: Results including T_1 relaxation. Red Curve: Results including T_1 relaxation and an applied back-correction using a simulated T_1 value.

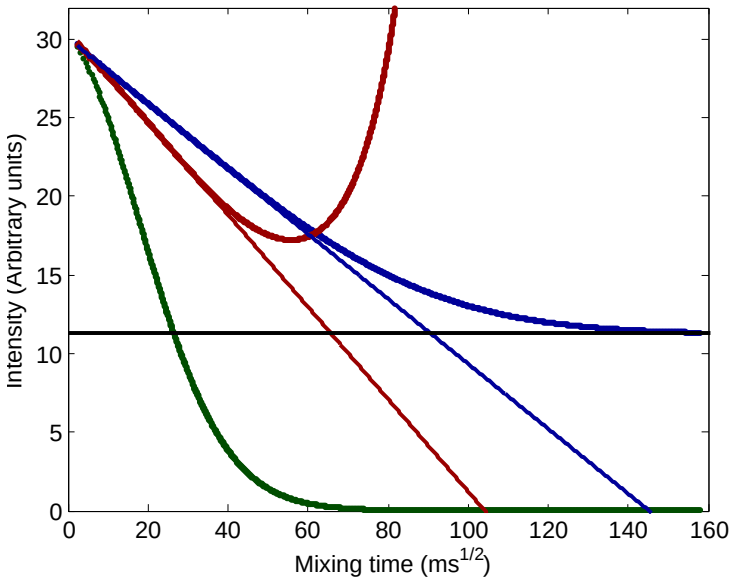


Figure 4.15: Simulated diffusion profiles for a lamellar PMMA-b-PS diblock polymer with a total domain size of 40 nm, a PMMA volume fraction of 0.375 and with the magnetisation starting in the PMMA domain. Blue Curve: Results without including T_1 relaxation. Green Curve: Results including T_1 relaxation. Red Curve: Results including T_1 relaxation and an applied back-correction using a simulated T_1 value.

These results were reproduced for all the simulations carried out, which had domain sizes between 20-70 nm and a range of different volume fractions. In all cases the domain size produced from simulations with the magnetisation initially staring in the PS domain was larger than the actual value. The simulations with magnetisation starting in the PMMA domain produced smaller values than the actual domain size. The closest match to the actual domain size was produced by taking the arithmetic average of these two values.

These results bear some resemblance to the experimental data displayed in Table 4.6 for the PMMA-b-PS diblock polymers. The domain sizes calculated from the decays of the PS aromatic peak tended to be larger than the domain sizes calculated from the decays of the PMMA methoxy proton peak. As the simulations demonstrated that the average of the two back-corrected values gave a domain size closer to the actual value. This may also be true for the experimental results and the arithmetic average of the two domain sizes displayed in column four of Table 4.6 may provide a better estimation of the polymer domain size.

However, the fluctuations in the domain sizes calculated from the experimental results do not appear to be as extreme as those observed in the simulations. A possible explanation for this difference is that during the simulations we assumed that the homopolymer T_1 values are a reasonable estimate of the intrinsic T_1 values of the diblock polymers and perhaps this is not the case. If the intrinsic T_1 values of the two domains were closer together this would likely result in less extreme fluctuations due to T_1 differences.

Figures 4.16 and 4.17 show the spin diffusion profiles for the build-up of intensity for the cross-peak between the PS aromatic and PMMA methoxy protons

for samples 1A and 1E respectively. Neither of the displayed profiles incorporated a T_1 correction. A range of simulated profiles, carried out using different domain sizes, are also displayed in each figure. On the basis of the simulations the best fit to the experimental data for sample 1A would be for a domain size between 20-25 nm. For sample 1E the best fit was obtained using a domain size of 40 nm. These domain sizes are similar to the domain sizes shown in Table 4.6 which were calculated from the experimental data using the initial rate approximation. The simulated results most closely match the domain size obtained by taking the arithmetic average of the domain sizes obtained from the decay of the PMMA methoxy and the PS aromatic protons diagonal peaks (the third column in Table 4.6). This again suggests that this average may provide a better estimate of the domain size rather than the results obtained from the decay of the PMMA methoxy peak or the PS aromatic peak alone.

These simulations provide a route to obtaining domain sizes from the experimental data without the need to apply a back-correction. However, in its current form the simulation relies on certain input parameters including the T_1 values and a spin diffusion coefficient. In the simulations carried out in this section the homopolymer T_1 values were used. Although, as was previously stated, these may not represent the true intrinsic T_1 value of the diblock polymers.

There is potential to further develop these simulations so that they can be carried out with fewer input parameters and also so they can take into account other polymer morphologies. Simulating other morphologies would involve changing the current simulation involving a line of points into either a grid of points for cylindrical structures or a data cube for spherical structures.

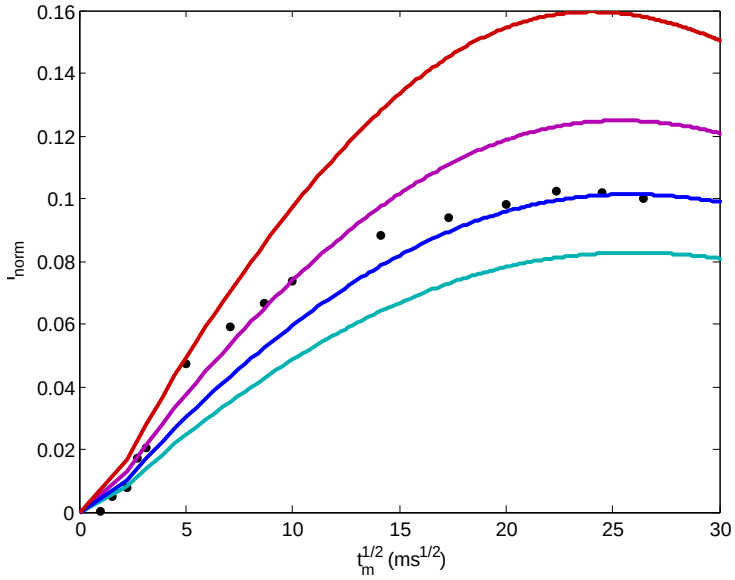


Figure 4.16: Experimental data showing the intensity build-up of the cross-peak between the PMMA methoxy and PS aromatic protons in sample 1A (black dots). Four simulated build-up curves, of differing domain size, incorporating the effects of both spin diffusion and T_1 relaxation are also displayed. Cyan = 30 nm domain size. Blue = 25 nm domain size. Purple = 20 nm domain size. Red = 15 nm domain size.

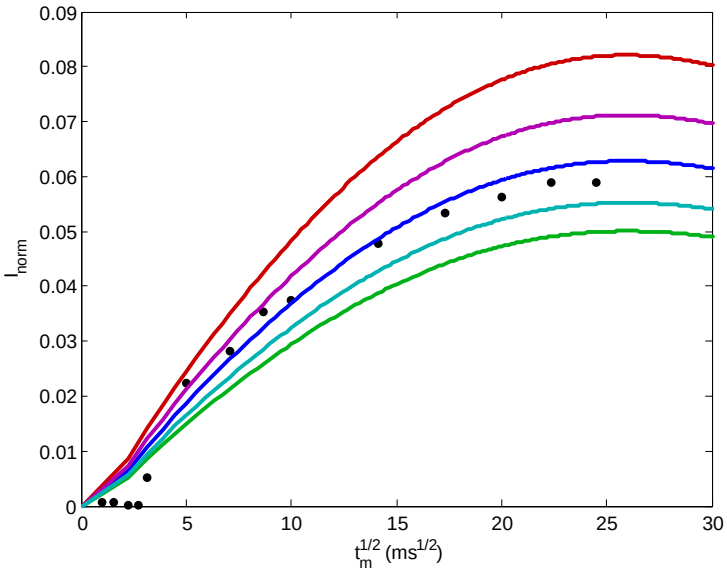


Figure 4.17: Experimental data showing the intensity build-up of the cross-peak between the PMMA methoxy and PS aromatic protons in sample 1E (black dots). Five simulated build-up curves, of differing domain size, incorporating the effects of both spin diffusion and T_1 relaxation are also displayed. Green = 50 nm domain size. Cyan = 45 nm domain size. Blue = 40 nm domain size. Purple = 35 nm domain size. Red = 30 nm domain size.

4.4 Conclusions

The domain sizes of a range of block co-polymers have been successfully measured using solid-state NMR with ultra-fast MAS. In this regime straightforward ^{1}H exchange experiments can be used to acquire spin diffusion spectra with fast acquisition times. The NMR measured domain sizes compared favourably to the results of SAXS and TEM studies. The spin diffusion coefficients of the PMMA-b-PS samples were determined by internal calibration whereas for the PMMA-b-PBzMA these values were extracted from spectra of the relevant homopolymers. In all cases the spin diffusion coefficients were much reduced under the application fast MAS. A range of simulations were also carried out to investigate the effect that T_1 relaxation has on these experiments. The use of a back-correction using T_1 values obtained from saturation-recovery experiments did result in some variation in the data. Simulations incorporating T_1 relaxation effects were used to fit the experimental data for two polymer samples and this produced domain sizes that were similar to results from the initial rate approximation. Additionally, the simulations suggested that a better estimate of the domain size can be obtained using the initial rate approximation if the results from diffusion profiles obtained by monitoring magnetisation changes in both blocks of the diblock polymer are averaged.

Chapter 5

Spin Diffusion Coefficient of Polystyrene

A study of the factors affecting the spin diffusion coefficient of polystyrene is presented in the following section. The rate of spin diffusion was established at both varying MAS rate and varying temperature. A temperature calibration of the 1.3 mm MAS probe was carried out to determine the actual temperature of the sample. The effect of incorporating recoupling sequences (see Section 3.4) into the mixing time was also investigated.

5.1 Experimental Method

Polystyrene spectra were acquired at a range of spinning rates between 15 and 65 kHz, using the same experimental procedure outlined in Section 4.2.2. The spectral width was set to 50 ppm in both dimensions for spectra acquired at spinning rates of 40 kHz and above but it was widened to 100 ppm for the spectra acquired at 35 kHz and below to incorporate spinning sidebands. Spectra were recorded with mixing times that varied between 0.00005 s and

0.1 s and relaxation delays that varied between 4 and 7.5 s. To study the effects of changing temperature on the diffusion coefficient the spectra at 60 kHz spinning speed were recorded at three different VT gas temperatures (268, 298 and 328 K). All other spectra were recorded with the VT gas set to 298 K.

^{1}H-^{1}H spin diffusion spectra were recorded at 60 kHz MAS with both the RFDR and the $SR6_6^2$ recoupling sequences inserted into the mixing time of the experiment. The RFDR sequence was implemented in a windowed fashion using four equally spaced 5 μs 180° pulses applied within four rotor periods. The pulse phases following the XY4 phase alternation scheme[34;84]. The $SR6_6^2$ is a windowless recoupling sequence that uses a $90_{180}270_0$ composite pulse as the basic element of the pulse sequence. The length of this basic element must equal the full rotor cycle time and to achieve this rotor synchronisation at 60 kHz MAS it was necessary to use a 90° pulse length of 4.17 μs. This basic element is repeated six times with a phase alternation of ±60° and then this sequence is supercycled using both an inversion supercycle and a three step phase supercycle. The inversion supercycle involves repeating the sequence with the opposite sign on the phase of all the pulses and the three step phase cycle involves repeating the pulse sequence and the phase inverted pulse sequence three times stepping the phases on all the pulses through 0°, 120° and 240°. For full details of the set-up and operation of this pulse sequence the relevant literature should be consulted[35;36].

Obviously, the length of the recoupling pulse sequences restricts the choice of mixing times that can be used in the acquisition. For the RFDR sequence, spectra were acquired at mixing times corresponding to multiples of the full RFDR sequence (four rotor periods) with values ranging between 0.0001 s to

0.01 s. Due to the supercycling scheme used the total length of the $SR6_6^2$ sequence is equal to 36 rotor cycles. This was not considered a sufficiently fine increment to accurately track the changes in magnetisation due to spin diffusion. As such, mixing times were acquired at multiples of 12 rotor cycles, which corresponded to sampling after every inversion supercycle of the sequence. Typical mixing times ranged between 0.0002 s to 0.003 s.

The processing, deconvoluted and analysis of all the spectra was carried out following the procedure outlined in Section 4.2.2

5.2 Temperature Calibration of the 1.3 mm Probe

Temperature calibration of MAS probes is necessary due to the significant frictional heating generated by fast spinning. Although most probes come equipped with a temperature control system, due to mechanical constraints, the temperature displayed by the spectrometer reflects the temperature of the VT gas. The actual sample temperature is typically much higher and as such an independent temperature calibration is required. Lead nitrate is widely used for temperature calibration of MAS probes as ^{207}Pb exhibits a temperature dependent chemical shift and can be used over a wide range of temperatures[85–88].

The temperature of the 1.3 mm probe was calibrated by extracting the isotropic shift from powder spectra of lead nitrate recorded under static conditions at a variety of temperatures. On the basis of these results a relationship between temperature and the isotropic chemical shift of ^{207}Pb was established. This

was subsequently used to determine the actual sample temperature from MAS spectra of lead nitrate acquired at a variety of different MAS rates and VT gas temperatures.

Static ^{207}Pb spectra of lead nitrate were recorded using a spin echo pulse sequence to avoid magnetisation loss during the spectrometer dead time. The 90° pulse length was set to 4.5 μs and an echo time of 43.3 μs was used. The chemical shift scale was referenced by setting the downfield line in the ^{13}C NMR spectrum of adamantane to 37.77 ppm. This is equivalent to setting the ^{1}H shift of tetramethylsilane in a 1% solution in $CDCl_3$ solution, which is the primary reference in the IUPAC recommended unified scale, to zero ppm[89]. It is then possible to use tables of Ξ values defined in Equation 5.1, which are stored on the spectrometer, to convert between the primary reference and a secondary reference of second nuclide, X, such as ^{207}Pb.

$$\Xi = \nu^{obs}_{sample}(X)/\nu^{obs}_{TMS} \tag{5.1}$$

Spectra were recorded at increments of 10 K between 288 and 338 K. Under static conditions it was assumed that the temperature recorded on the spectrometer display was an accurate measure of the temperature at the sample.

Figure 5.1 shows the expected powder pattern of lead nitrate which is axially symmetric and has a small CSA compared to other common lead compounds[90]. The isotropic chemical shift can be calculated according to Equation 2.31 however the principal components of the chemical shift tensor may be hard to define by visual inspection of the powder pattern and more accurate values may be obtained by simulation. The fit to the spectrum in Figure 5.1 was produced by simulation and fitting of the powder pattern using the SIMPSON program

Temperature (K)	**Isotropic Shift (ppm)**	**CSA (ppm)**	**Asymmetry**
288	-3496	-38.74	0.099
298	-3488	-35.67	0.107
308	-3481	-33.87	0.116
318	-3474	-32.81	0.117
328	-3466	-31.35	0.126
338	-3458	-29.36	0.143

Table 5.1: Table showing isotropic shift, CSA and asymmetry obtained from fits to the static spectra of lead nitrate recorded at different temperatures.

for solid-state NMR simulations[11]. The values of the isotropic chemical shift, CSA and asymmetry were all optimised using a simplex minimisation procedure. The results for all the measured temperatures can be seen in Table 5.1. The variation of the lead isotropic chemical shift with temperature is shown in Figure 5.2 and the equation of the fitted line suitable for converting between isotropic shift value and temperature (T) is given below,

$$\delta^{207}Pb = 0.76\ T(K) - 3714. \tag{5.2}$$

This result is similar to a previous calibration available in the literature[87].

Lead nitrate MAS spectra were recorded at a range of different VT gas temperatures and spinning speeds. Figure 5.3 shows a selection of MAS spectra recorded at different spinning speeds at a VT gas temperature of 298 K. The peak position moves downfield with increasing MAS rate indicating that the sample temperature is increasing. The actual sample temperature was calculated by picking the top of the lead nitrate peak and converting the chemical shift into a temperature according to Equation 5.2. Figure 5.4 shows a plot of the actual sample temperature with increasing MAS rate while the VT gas temperature was set to 298 K. At the fastest spinning speeds frictional effects

cause significant sample heating and the true sample temperature at 60 kHz spinning is 328 K.

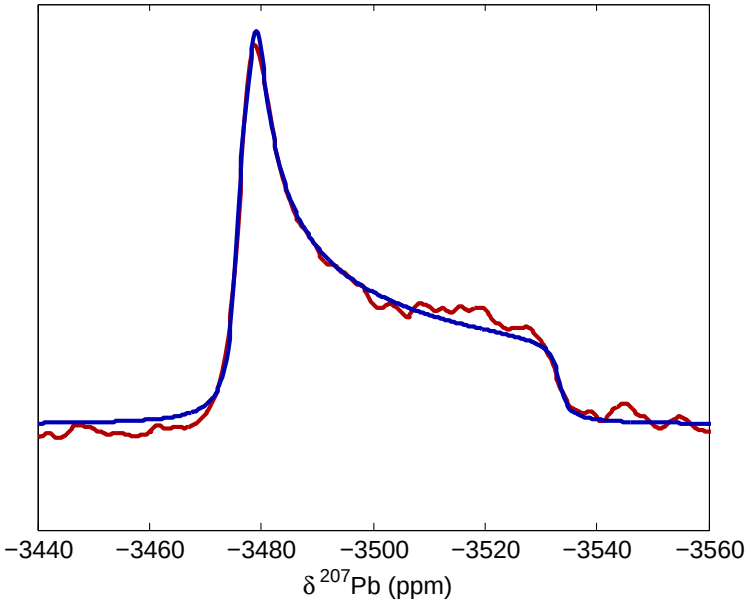


Figure 5.1: Static spectrum of lead nitrate recorded with the VT gas temperature set to 288 K and the simulated fit to the spectrum

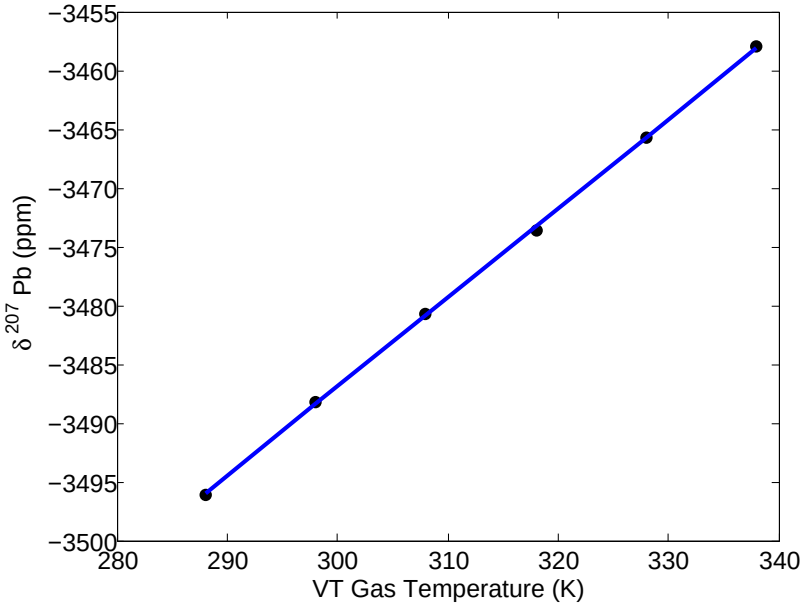


Figure 5.2: Plot showing the variation of the chemical shift of lead nitrate with changing temperature.

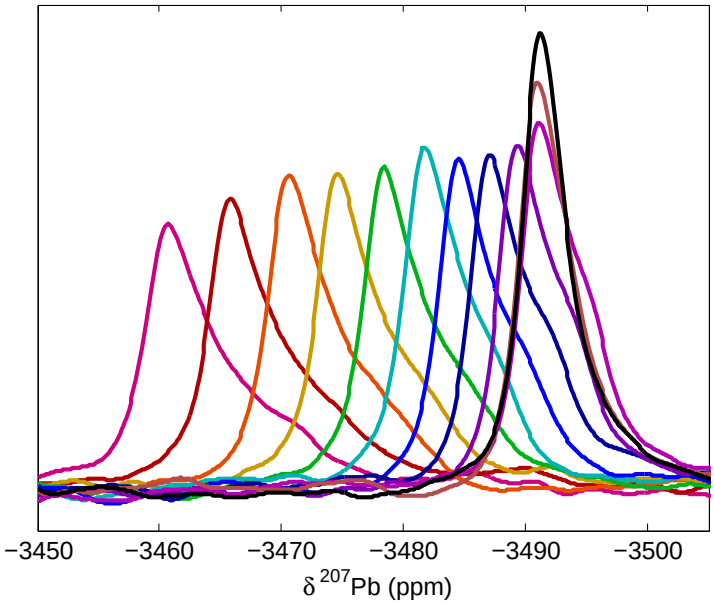


Figure 5.3: MAS spectra of lead nitrate recorded with increasing spinning speed at a constant VT gas temperature of 298 K. Black = 10 kHz, Brown = 15 kHz, Magenta = 20 kHz, Purple = 25 kHz, Navy = 30 kHz, Blue = 35 kHz, Cyan = 40 kHz, Green = 45 kHz, Yellow = 50, Orange = 55 kHz, Red = 60 kHz and Pink = 65 kHz

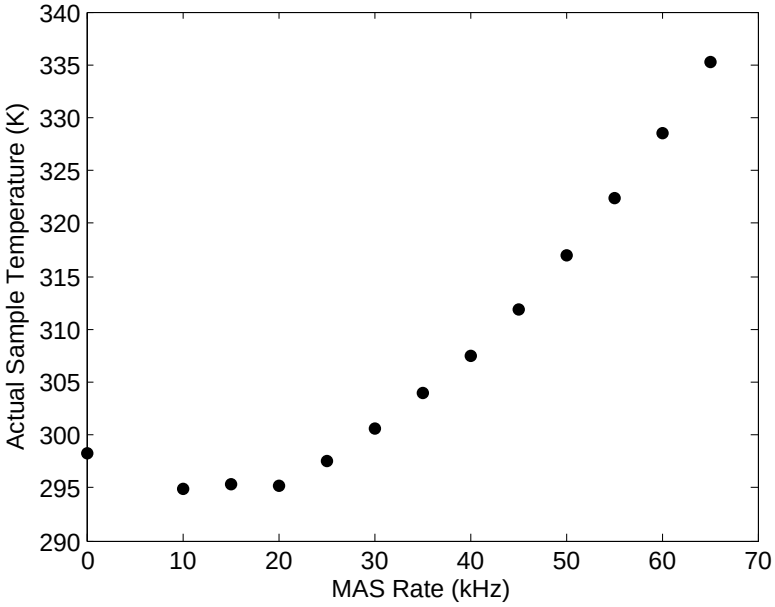


Figure 5.4: Plot of the actual sample temperature with increasing MAS rate when the VT gas temperature was set to 298 K

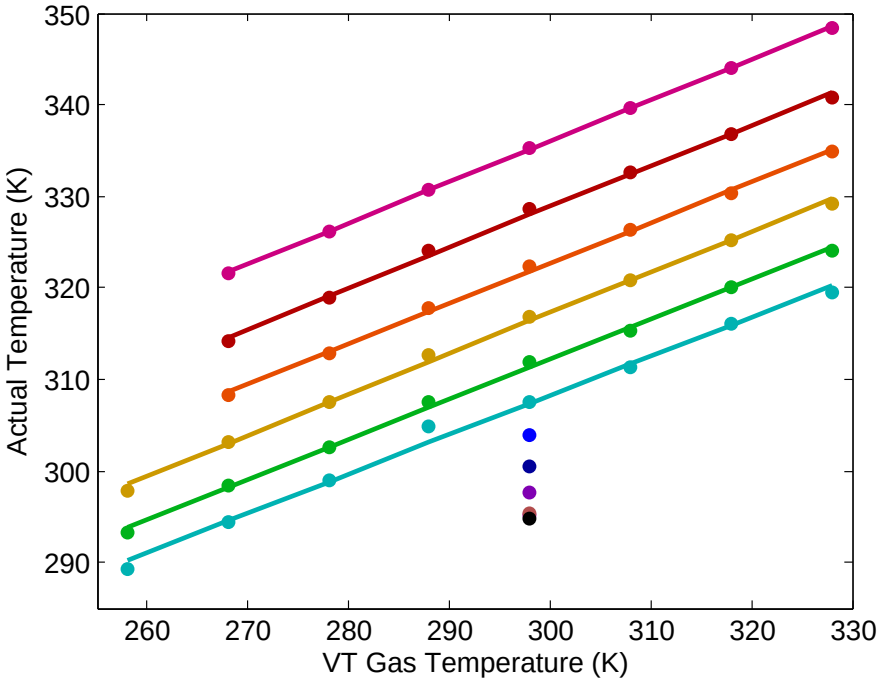


Figure 5.5: Plot of the spectrometer VT gas temperature against the actual sample temperature. Black = 10 kHz, Brown = 15 kHz, Magenta = 20 kHz, Purple = 25 kHz, Navy = 30 kHz, Blue = 35 kHz, Cyan = 40 kHz, Green = 45 kHz, Yellow = 50, Orange = 55 kHz, Red = 60 kHz and Pink = 65 kHz

The spectra in Figure 5.3 are fairly broad and this is due to a chemical shift distribution caused by the temperature gradients present across the sample. This spread of frequencies becomes broader at higher spinning speeds and we attribute this to the increasing amount of drive gas applied to the rotor causing a more pronounced temperature gradient. Figure 5.5 shows the actual sample temperature against the VT gas temperature for a range of MAS rates. It is clear from the graph that changes to the VT gas temperature do not result in a commensurate change in the actual sample temperature. This is probably caused by the application of room temperature drive and bearing gas to the rotor, which buffer the sample to a certain extent against the applied temperature changes.

5.3 Results and Discussion

Figure 5.6 shows two ^{1}H-^{1}H spin diffusion spectra of polystyrene recorded at 60 kHz MAS with different mixing times. As expected, only diagonal peaks are present in the spectrum acquired with a short mixing time. At longer mixing times cross peaks appear between the aromatic and aliphatic sites demonstrating that magnetisation is exchanged between the two types of proton present in the sample.

Figure 5.7 plots the build up of polystyrene cross peak intensity with increasing mixing time for a variety of different spinning speeds. Both the decrease in the initial gradient and the increase in the time taken for full equilibration of magnetisation observed with increasing MAS rate indicate that a reduction in the rate of spin diffusion is taking place. Through extrapolation of the initial rate of build up out to the time taken for full equilibration of magnetisation a t^{*}_{m1} value can be obtained that can be used to calculate the spin diffusion coefficient according to Equation 4.14. Figure 5.8 displays the change in the spin diffusion coefficient with increasing MAS rate. Table 5.4 contains all the

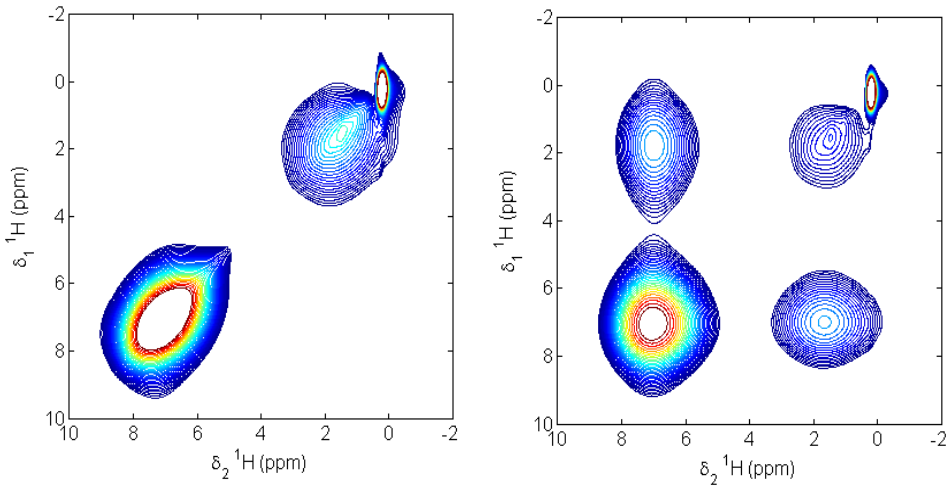


Figure 5.6: ^{1}H-^{1}H spin diffusion spectra of polystyrene recorded with mixing times of 0.002 s (left) and 0.02 s (right)

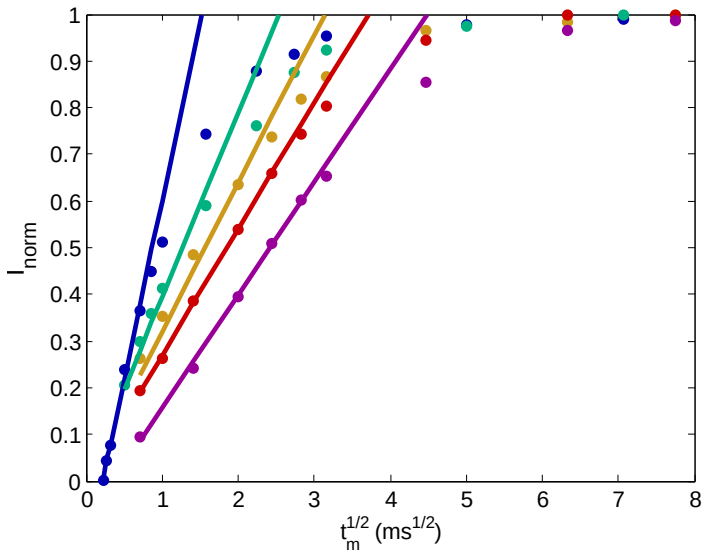


Figure 5.7: Diffusion profiles of the polystyrene cross peak intensity with increasing mixing time for a range of MAS rates. Blue = 20 kHz. Green= 30 kHz Yellow= 40 kHz Red = 50 kHz Purple = 60 kHz

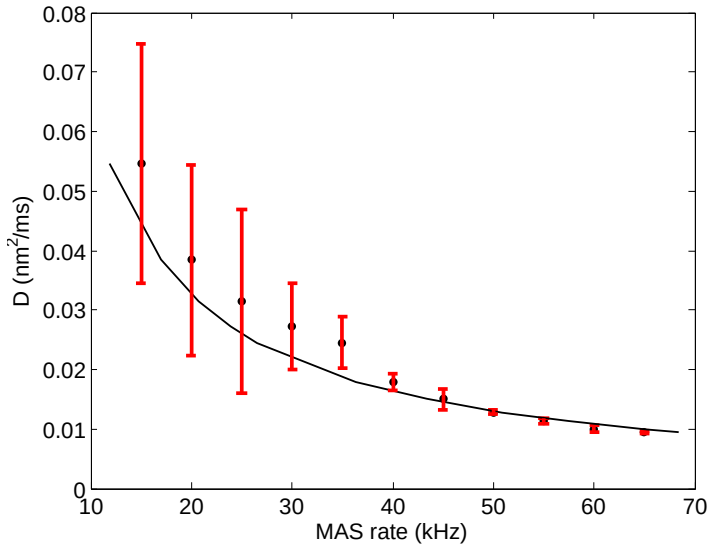


Figure 5.8: Plot of the polystyrene spin diffusion coefficient with increasing MAS rate.

spin diffusion coefficients reported in this section.

The rate of spin diffusion decreases with increasing MAS rate and at the highest spinning rates available its value is much reduced. A previously reported value

for the diffusion coefficient of PS-b-PMMA block-copolymers was given as 0.8 nm^2ms^{-1} at 4.5 kHz MAS[46] and more recent publications have cited values for the diffusion coefficient of polystyrene of 0.2-0.3 nm^2 ms^{-1} at low spinning rates (2-5 kHz).[73] The spin diffusion coefficient of polystyrene reported here at a spinning rate of 60 kHz is more than an order of magnitude lower. The reduction in spin diffusion coefficient with increasing MAS is unsurprising. Faster spinning leads to more efficient averaging of the proton homonuclear dipolar couplings which are the origin of the magnetisation transfer occurring during spin diffusion.

The error bars in Figure 5.8 are obtained from the 95% confidence limits of the fitted spin diffusion profiles used to extract the t^*_{m1} values and obtain a spin diffusion coefficient. The reduction in the size of the error bars with increasing spinning rate is due to the line narrowing effect of MAS. At the lowest spinning speeds the spectra are substantially broadened meaning that the deconvolution and fitting is less reliable resulting in larger error bars.

Previous work has been carried out to investigate the changes to the spin diffusion coefficient with spinning rate for a sample of polyethylene at low MAS rates[55]. A relationship between spinning rate and the diffusion coefficient was established based on the motional averaging of the dipolar interaction by MAS. This was derived on the basis of the following equation that is often used to describe motional averaging in solids[55;91]

$$\tau = \alpha \frac{1}{\sqrt{M_2}} tan\left[\frac{\pi}{2}\frac{M_2}{M_2^0}\right]. \tag{5.3}$$

M_2 is the proton second moment and M_2^0 is the proton second moment of the rigid lattice. τ is the correlation time associated with the motion and α is

an adjustable parameter which is usually close to 1. A correlation time, τ_R related to the sample spinning under MAS can be defined as $\tau_R = 2\pi\nu_R$ where ν_R is the rotor frequency. Diffusion coefficients can be related to the proton second moment by the following equation,

$$D = k_0 < r^2 > \sqrt{M_2} \qquad D_0 = k_0 < r^2 > \sqrt{M_2^0}. \tag{5.4}$$

where k_0 is a constant, $< r^2 >$ is the mean square distances between nearest spins and D_0 is the rate of spin diffusion in the rigid lattice in the absence of MAS. This results in the following equation relating the spinning speed to the diffusion coefficient[55]

$$2\pi\nu_R = \frac{\sqrt{M_2^0}D}{\alpha D_0 tan\left[\frac{\pi}{2}\frac{D^2}{D_0^2}\right]} - \frac{1}{\tau}. \tag{5.5}$$

The τ in this equation is the correlation time that relates to thermally activated molecular motion.

The black line in Figure 5.8 shows a fit to the experimental data using this equation. The fit created using Equation 5.5 is a good match to the experimental data displayed in Figure 5.8 and so we can conclude that the theory used to describe the averaging of the dipolar couplings and hence the changes in the spin diffusion observed at lower MAS rates are still valid at much faster spinning rates. For the fit the value of α was assumed to be 1. The value of $\frac{1}{\tau}$ was restricted to 0, implying that the reduction in the spin diffusion coefficient is purely caused by the sample spinning. A value of 0.8 nm^2 ms^{-1} was initially used for D_0, which is a literature value obtained for PMMA-b-PS diblock polymers under low MAS rates[46]. The value of $\sqrt{M_2^0}$ was optimised during the fit, giving a value of $\approx$ 8 kHz.

For a Gaussian lineshape the linewdith, $\Delta\nu$, is related to $\sqrt{M_2^0}$ by the following equation

$$\Delta\nu = 2\sqrt{2ln2M_2^0}. \tag{5.6}$$

Assuming the spectral lineshape is Gaussian this gives a proton linewidth of $\approx$ 19 kHz. A more recent report determined a rate of spin diffusion of between 0.2-0.3 nm^2 ms^{-1} for polystyrene at low spinning speeds[73]. The same fit to the data was generated using values of 0.2 and 0.3 nm^2 ms^{-1} for D_0. This resulted in values of $\sqrt{M_2^0}$ of 32 and 21 kHz and values of $\Delta\nu$ of 76 and 50 kHz respectively. These linewidths, which are presented in Table 5.3 along with a theoretical value, correspond to generally expected values for protons in strongly dipolar coupled solids in the absence of MAS.

A value for M_2^0 can also be calculated using the following equation[91–94], which is valid for a powder sample containing randomly orientated crystallites,

$$M_2^0 = \frac{3}{5}\Big(\frac{\mu_0}{4\pi}\Big)^2\gamma^4\hbar^2 I(I+1)\Big(\frac{1}{N}\Big)\sum_{j\neq k}\frac{1}{r_{j,k}}. \tag{5.7}$$

N is the number of protons in the dipolar coupled network (eight for the polystyrene repeating unit). In order to calculate the sum present in this equation knowledge of the various proton-proton distances ($r_{j,k}$) in the compound is required. These distances were obtained using the procedure detailed in Chapter 4 for a single repeating unit of polystyrene (see Figure 5.9). However, all the proton-proton distances will be included in the summation (see Table 5.2), whereas in Chapter 4 only the average distance between the polystyrene aromatic and the polystyrene aliphatic protons was used.

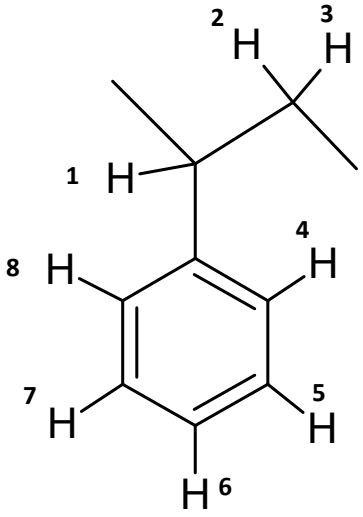


Figure 5.9: A single repeating unit of polystyrene

j,k	**r** ($\AA$)	**j,k**	**r** ($\AA$)	**j,k**	**r** ($\AA$)	**j,k**	**r** ($\AA$)
12	2.5	31	3.1	51	5.5	71	4.6
13	3.1	32	1.8	52	6.2	72	6.6
14	3.8	34	2.3	53	1.8	73	6.2
15	5.5	35	1.8	54	2.5	74	5.0
16	5.8	36	3.9	56	2.5	75	4.3
17	4.6	37	6.2	57	4.3	76	2.5
18	2.3	38	7.2	58	5.0	78	2.5
21	2.5	41	3.8	61	5.8	81	2.3
23	1.8	42	3.9	62	7.2	82	4.5
24	3.9	43	2.3	63	3.9	83	7.2
25	6.2	45	2.5	64	4.3	84	4.3
26	7.2	46	4.3	65	2.5	85	5
27	6.6	47	5.0	67	2.5	86	4.3
28	4.5	48	4.3	68	4.3	87	2.5

Table 5.2: Table showing the proton-proton distances in a repeating unit of polystyrene

	Fit, D_0 = 0.8 nm^2 ms^{-1}	Fit, D_0 = 0.3 nm^2 ms^{-1}	Fit, D_0 = 0.2 nm^2 ms^{-1}	theoretical
$\sqrt{M_2^0}$ (kHz)	8	21	32	37
$\Delta\nu$ (kHz)	19	50	76	88

Table 5.3: Table showing the proton second moments and proton linewidths obtained from fits to the data and from a theoretical calculation.

This value of M_2^0 calculated using Equation 5.7 was ≈ 1400 kHz^2. This resulted in values of $\sqrt{M_2^0}$ and $\Delta\nu$ of 37 and 88 kHz respectively. These theoretical values are compared to the results from the fitting in Table 5.3. The best match to the theoretical value is obtained by using a fit with D_0 set to 0.2 nm^2 ms^{-1}.

However, there a variety of reasons why the value calculated using Equation 5.7 may differ from the values obtained from the fit. Firstly, each of the values for D_0 used for the fits (0.8, 0.3 and 0.2 nm^2 ms^{-1}) were measured on a polymer sample under low MAS rates at roughly room temperature[46;73]. The value of M_2^0 calculated using Equation 5.7 is for a non-spinning sample in a rigid lattice (even in a solid sample some motion will be present at room temperature). Secondly, the calculation of a theoretical value should take into account all of the proton-proton distances present in the molecule. To produce the theoretical value in Table 5.3 the proton-proton distances given in Table 5.2 were used. These are the proton-proton distances within a repeating unit and therefore this calculation neglects the effect of any proton-proton couplings between repeating units and all intramolecular proton-proton couplings.

In order to prove that the reduction in spin diffusion with increasing spinning speed occurs primarily due to the effect of MAS it is important to consider any effect temperature may have on the sample. The polystyrene spectra at

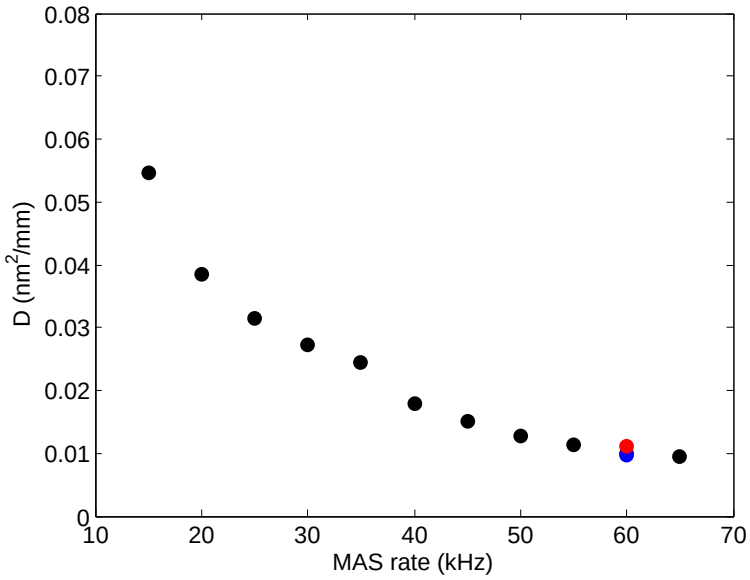


Figure 5.10: Spin diffusion coefficient of polystyrene with increasing MAS rate. Data acquired at VT gas temperatures of 298 K = black markers, 328 K = red marker and 268 K = blue marker.

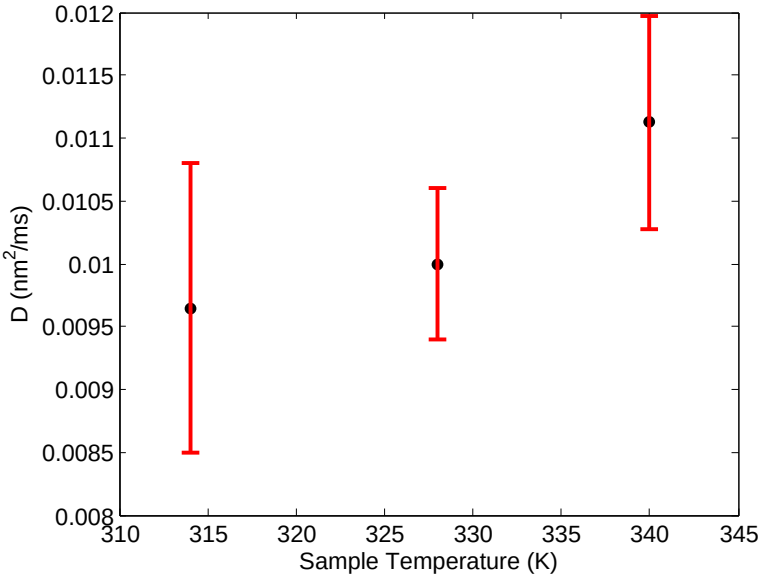


Figure 5.11: Plot of the polystyrene spin diffusion coefficient recorded at 60 kHz MAS with increasing sample temperature

all the different spinning speeds were recorded at a set temperature of 298 K. However, it is clear from Figure 5.4 that this does not accurately depict the

temperature at the sample and at 60 kHz MAS a displayed temperature of 298 K resulted in an actual sample temperature of 328 K. In order to prove that the changes in spin diffusion were not due to sample heating the spin diffusion spectra at 60 kHz MAS were re-recorded at two different temperatures. For the higher (328 K) and the lower (268 K) displayed temperatures the actual sample temperature was 340 K and 314 K respectively (see Figure 5.5). Figure 5.10 is the same as Figure 5.8 except for the addition of the calculated diffusion coefficients recorded at a higher and lower temperature (the error bars have also been removed for clarity). At 60 kHz MAS rate there is a small increase in the polystyrene spin diffusion coefficients with increasing temperature. This can be seen more clearly in Figure 5.11 that plots the three spin diffusion coefficients against the actual temperature. However, the change is small and not particularly significant. Additionally, if the spin diffusion coefficient did change with temperature it would mainly be expected to decrease with increasing temperature. This is because temperature changes would be expected to lead to increased motion in the system that could contribute to the averaging of the dipolar couplings, therefore reducing the rate of spin diffusion.

In general temperature changes would only be expected to affect the rate of spin diffusion if they lead to drastic increases in sample motion. All the samples studied were below the glass transition and would have quite restricted motion that would remain largely unchanged over a moderate temperature range. The results displayed in Figures 5.10 and 5.11 support this conclusion. The decrease in spin diffusion coefficient observed in Figure 5.8 can therefore be primarily attributed to the averaging of the dipolar couplings due to MAS and not to any underlying temperature variation. A significant increase in the sample mobility of these polymers would only be expected to occur if the temperature approached the glass transition (T_g). If the samples studied had been near or

MAS rate (kHz)	**D (nm^2 ms^{-1})**	**MAS rate (kHz)**	**D (nm^2 ms^{-1})**
15	0.0547 (±0.0201)	50	0.0128 (±0.0004)
20	0.0384 (±0.0160)	55	0.0113 (±0.0004)
25	0.0315 (±0.0155)	60	0.0100 (±0.0006)
30	0.0272 (±0.0072)	65	0.0095 (±0.0002)
35	0.0245 (±0.0043)	60†	0.0096 (±0.0012)
40	0.0179 (±0.0015)	60‡	0.0111 (±0.0009)
45	0.0150 (±0.0017)	60*	0.1272 (±0.0155)

Table 5.4: Table showing the calculated spin diffusion coefficients of polystyrene at different MAS rates. † VT gas temperature was set to 268 K. ‡ VT gas temperature was set to 328 K. For all other values the VT gas temperature was set to 298 K. * RFDR recoupling was used in the mixing time.

above the T_g the effect of temperature on the spin diffusion coefficient may have been more significant.

Additionally, in the work carried out on the PMMA-b-PS samples in the previous chapter the spin diffusion coefficient was obtained using an internal calibration. This means that the calibrated spin diffusion coefficient is correct for the temperature and spinning speed used during the experiment. This is one of the principal advantages of carrying out an internal calibration of the diffusion coefficient.

The use of recoupling in spin diffusion experiments was also investigated. Three diffusion profiles showing the build-up of polystyrene cross peak magnetisation with increasing mixing time are displayed in Figure 5.12. The build-up of magnetisation obtained from spectra acquired using RFDR proceeds at a much faster rate in comparison to the same experiments acquired without recoupling. This is a consequence of the RFDR sequence successfully recoupling the homonuclear dipolar couplings leading to a faster rate of spin diffusion. The results obtained by using a $SR6_6^2$ pulse sequence in the mixing time were

surprisingly poor. Although the curve seems to show an initial fast rate of magnetisation build-up, similar to the results for RFDR, it failed to approach the expected equilibrium magnetisation distribution. This was attributed to signal losses under the recoupling sequence becoming too pronounced to reliably analyse the data.

The rate of magnetisation loss with increasing mixing time was greater in spectra acquired with recoupling in comparison to spectra acquired without recoupling and this effect was more pronounced for the $SR6_6^2$ sequence than RFDR. In spectra acquired without recoupling the total loss of magnetisation occurring during the mixing time is solely the result of T_1 relaxation. Whereas the application of re-coupling sequences during the mixing time may lead to magnetisation losses via a variety of different mechanisms, e.g. pulse imperfections. The normalisation procedure used in the analysis should compensate for the reduction in the total magnetisation occurring during the mixing time but this may become unreliable in the case of very low magnetisation intensity. Under the $SR6_6^2$ the total magnetisation present is rapidly reduced to levels that are too low to be reasonably analysed.

The spectra acquired using the RFDR sequence were used to calculate a diffusion coefficient using the previously described method. Figure 5.13 shows a plot of the diffusion coefficients of polystyrene acquired at different spinning speeds and the diffusion coefficient for polystyrene acquired at 60 kHz MAS with RFDR applied in the mixing time. The diffusion coefficient obtained under RFDR is much larger (0.1272 nm^2 ms^{-1}) than the diffusion coefficients acquired without recoupling (0.0100 nm^2 ms^{-1}) proving that application of RFDR in the mixing time can successfully increase the rate of spin diffusion by at least an order of magnitude.

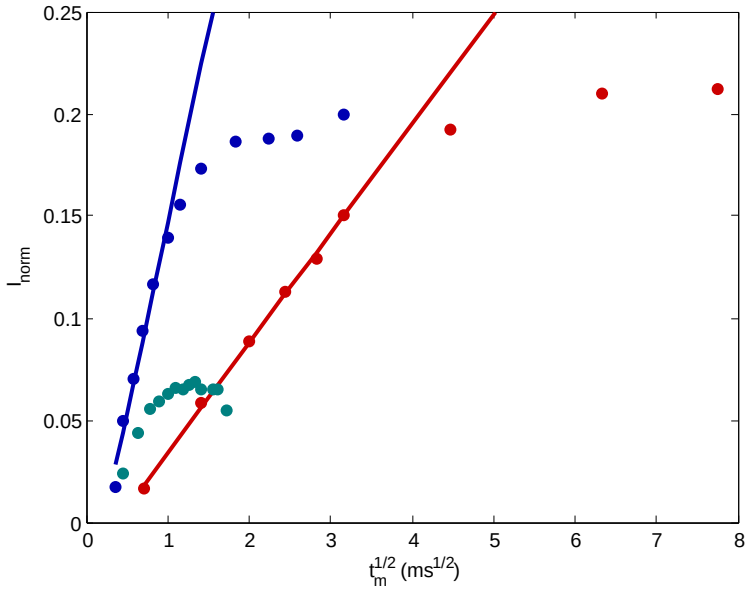


Figure 5.12: The build-up of polystyrene cross peak intensity with increasing mixing time obtained from spectra recorded using RFDR (blue), the $SR6_6^2$ sequence (cyan) and without recoupling (red).

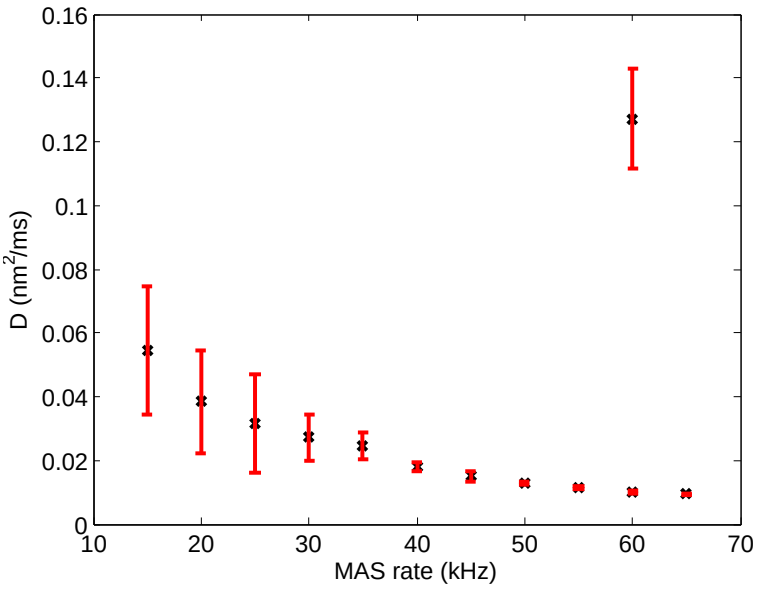


Figure 5.13: Plot of the polystyrene spin diffusion coefficient with increasing MAS rate. The diffusion coefficient obtained from spectra acquired at 60 kHz MAS with RFDR recoupling in the mixing time is also included.

5.4 Conclusions

A study was undertaken into the factors affecting the spin diffusion coefficient in a sample of polystyrene. The spin diffusion coefficient was observed to decrease with increasing spinning rate due to the improved averaging of the homonuclear dipolar couplings. Moderate changes in temperature, of the sort expected to occur with application of MAS, appeared to have little effect on the spin diffusion coefficient. The effect of introducing recoupling sequences into the mixing time of the spin diffusion experiment was carried out. The application of RFDR in the mixing time was shown to drastically increase the rate of spin diffusion, presumably through successful recoupling of the dipolar couplings. However, the use of recoupling sequences leads to an increased rate of total magnetisation loss from the spectrum that may be counter productive in certain cases. Particularly when longer distances are present (and therefore longer mixing times are needed), such as for the domain sizes of the diblock polymers.

Chapter 6

Hydroxyapatite Nanoparticles

Bone tissue is an organic-inorganic composite material whose primary mineral component consists of nanoscale plates of hydroxyapatite[95] ($Ca_{10}(PO_4)_6(OH)_2$). Solid-state NMR has been widely applied to hydroxyapatite (HAp) containing biomaterials in order to elucidate their structure and formation and to investigate various pathologies[96–100]. In addition to these naturally occurring materials solid state NMR has been frequently used to study synthetic hydroxyapatite nanoparticles[101–104]. Firstly the formation of these materials can give insight into the in vivo formation of hydroxyapatite and secondly as they resemble the natural material they can have important clinical applications, particulary in bone regeneration[95].

In this section a variety of HAp nanoparticles coated with different polymer dispersant molecules have been studied using solid-state NMR. In order to be industrially applicable, a method of creating HAp nanoparticles in a continuous flow process and subsequently dispersing them within a polylactic acid (PLA) matrix material was required. There are various possible advantages of using this composite material in bone repair. The use of hydroxyapatite alone may be problematic as loose HAp particles may migrate from the implant site to other

tissues where they may cause damage[105]. PLA is a biodegradable polymer that is suitable for medical applications and that can be used as a scaffold material in bone repair. Composites of these two materials have beneficial mechanical properties as the addition of the polymer may counteract the brittleness of the mineral phase creating a bone replacement material with the appropriate strength and toughness. Finally, implantable synthetic materials are more likely to undergo favourable recognition and binding within the body if they resemble the appropriate natural product[95]. The HAp nanoparticle within the PLA matrix suitably mimics bone tissue which is composed primarily of nanoscale hydroxyapatite surrounded by collagen fibres.

The HAp nanoparticles displayed a tendency to aggregate, and therefore fail to disperse correctly within the matrix. This clustering of the particles may detrimentally affect the strength of the material. To inhibit this aggregation process the nanoparticles are coated with short chain polymer molecules during the synthesis. The extent of coating is believed to be a critical factor that enables the dispersion of the nanoparticle in the PLA matrix. Solid-state NMR has been applied to a variety of HAp/dispersant molecule composite systems in order to gain a better understanding of the factors affecting the dispersant coating. In particular, it was used to elucidate the mechanism by which the dispersant polymers bind to the surface of the nanoparticle.

6.1 Materials

The HAp nanoparticles were produced by mixing an aqueous calcium nitrate stream with an aqueous ammonium phosphate stream in a continuous reactor[106]. The conditions in the reactor were held at 240 bar pressure and 220 °C temperature. For the coated hydroxyapatite materials, the dispersant

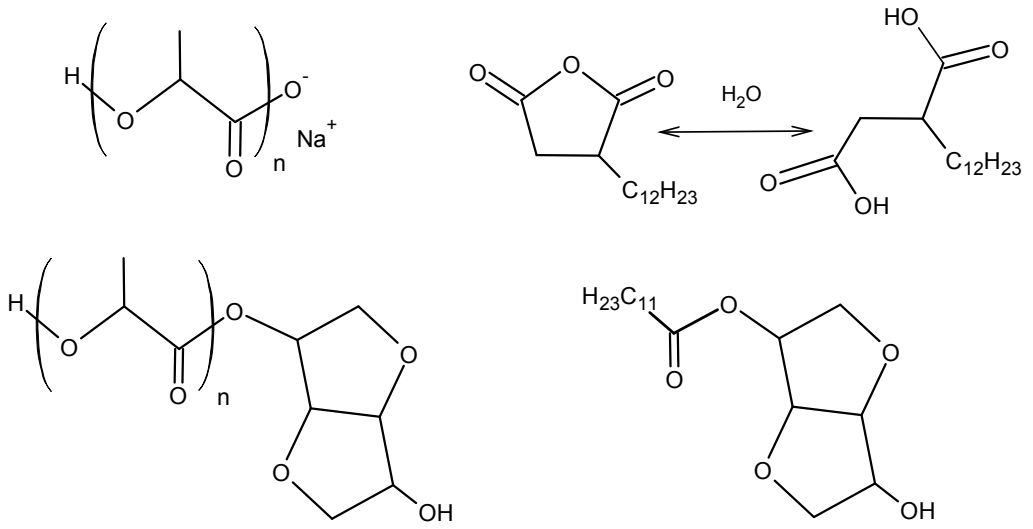


Figure 6.1: Structures of the dispersant molecules used to coat the surface of the nanoparticles. Top-left: PLA with a sodium carboxylate head group, n≈8. Top-right: dodecenyl succinic anhydride (DDSA) - this molecule undergoes ring opening in aqueous solution to form dodecenyl succinic acid which has a double carboxylate head group. Bottom-left: PLA with an isosorbide head group, n≈8 or 24. Bottom-right: lauric isosorbide.

molecules were also added into the reactor during the synthesis. The different dispersant molecules used to coat the surface of the nanoparticles are displayed in Figure 6.1. The two polylactic acid molecules displayed in Figure 6.1 contained around eight repeating units within the polymer chain. For comparison purposes a longer chain sample of polylactic acid with an isosorbide head group was analysed. This extended PLA chain contained around 24 repeating units. These different dispersant molecules can be categorised according to Table 6.1. The names given in brackets in the first column of the table shall be used to identify these molecules throughout this work.

The DDSA, which undergoes ring opening in aqueous solution as shown in Figure 6.1, was used as purchased. $[C_{11}H_{23}]$-$[C_7H_9O_5]$ was formed by an esterification reaction between isosorbide and lauric acid. The PLA based disper-

Dispersant molecule	Type of Chain	Type of Head Group
PLA + isosorbide head group, n≈8 ([PLA]-[$C_6H_9O_4$])	PLA	isosorbide
PLA + isosorbide head group, n≈24 ([PLA_{ex}]-[$C_6H_9O_4$])	PLA	isosorbide
PLA + carboxylate head group, n≈8 ([PLA]-[COONa])	PLA	carboxylate
Dodecenyl succinic acid ([$C_{12}H_{23}$]-[$C_2H_3(COOH)_2$])	aliphatic	bi-carboxylate
Lauric isosorbide ([$C_{11}H_{23}$]-[$C_7H_9O_5$])	aliphatic	ester isosorbide

Table 6.1: Properties of the different dispersant molecules used to coat the surface of the HAp nanoparticles

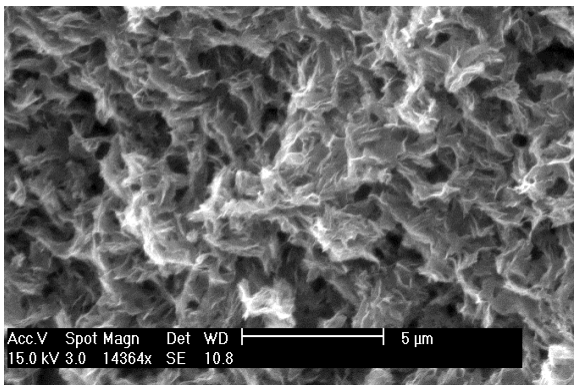


Figure 6.2: SEM image of the uncoated HAp nanoparticles.

sants were formed in a ring opening polymerisation reaction of lactide using a tin octanoate catalyst and either an isosorbide or a sodium hydroxide initiator. The dispersants were introduced into the reactor at the same time as the salts used to form the HAp and were dissolved in either a solution of acetone ([PLA]-[COONa], [PLA]-[$C_6H_9O_4$] and [PLA_{ex}]-[$C_6H_9O_4$]) or iso-propanol ([$C_{12}H_{23}$]-[$C_2H_3(COOH)_2$] and [$C_{11}H_{23}$]-[$C_7H_9O_5$]). All the nanoparticles extracted from the reactor were washed in water and acetone and then lyophilised.

Figure 6.2 shows an SEM (scanning electron microscopy) image of the un-

Sample	Approximate weight of the dispersant molecules as a % of the total weight of the sample.
HAp/[PLA]-[$C_6H_9O_4$]	13
HAp/[PLA_{ex}]-[$C_6H_9O_4$]	59
HAp/[PLA]-[COONa]	5
HAp/[$C_{12}H_{23}$]-[$C_2H_3(COOH)_2$]	10
HAp/[$C_{11}H_{23}$]-[$C_7H_9O_5$]	27

Table 6.2: Table showing the approximate weight of the polymer as a % of the total weight of the sample. These results were obtained from TGA.

coated hydroxyapatite nanoparticles. In order to assess the extent of coating of hydroxyapatite surface with the dispersant molecules ThermoGravimetric Analysis (TGA) was carried out and the results were supplied along with the samples. Table 6.2 summarises these results and displays the % weight of the sample that results from the presence of the dispersant molecules. Initially, the isosorbide containing dispersant molecules were expected to exhibit weaker binding to the surface of the nanoparticle in comparison to the dispersant molecules containing carboxylate groups. However, the TGA results appear to refute this hypothesis as the highest percentage weights were seen for the isosorbide containing composite materials (implying that the isosorbide dispersants were efficiently bound to the surface of the nanoparticle). This precipitated the use of solid-state NMR to investigate the mode of interaction between the dispersant molecules and the surface of the nanoparticle.

6.2 Experimental Set-up

^{1}H-^{31}P heteronuclear correlation spectra were acquired on the nanoparticles using DUMBO decoupling in the indirect dimension[25] and Lee-Goldberg Cross polarisation[18] to achieve the magnetisation transfer (see Chapter 3). Cross polarisation transfers magnetisation via the heteronuclear dipolar couplings and as such, peaks appearing in the correlation spectrum tend to indicate close spatial proximity between phosphorous and proton nuclei. ^{1}H-^{31}P correlation experiments have been widely used in solid state NMR to elucidate the structure of both synthetic hydroxyapatite and bone tissue[96–103]. In particular, they are useful in the study of these coated nanoparticles because the phosphorous is only present in the hydroxyapatite core whereas protons are present in both the mineral core and the dispersant molecules. Therefore, the peaks in a correlation spectrum may reveal which protons in the dispersant are close to the hydroxyapatite surface.

The ^{1}H-^{31}P correlation spectra were acquired at a MAS rate of 12 kHz, using the pulse sequence displayed in Figure 6.3. The relaxation delay was set from 3 - 4 s and SPINAL-64 decoupling[16] was applied to the proton channel during acquisition. For LGCP the power levels were matched to the ± 1 Hartmann-Hahn condition, the offset was between 40544.2 - 36084.39 Hz and a contact time of 5 ms was used. The 90° pulse length was set to 3.4 μs and the magic angle pulse length was set between 1.5 and 1.6 μs. The DUMBO pulse length was set to 26 μs and the field used was 96 kHz. The spectra were acquired with 4096 complex data points in the direct dimension and between 176 - 256 complex data points in the indirect dimension. Data was acquired using the States method to generate pure absorption lineshapes. The number of scans used to acquire the experiment was between 176 - 240 per increment giving

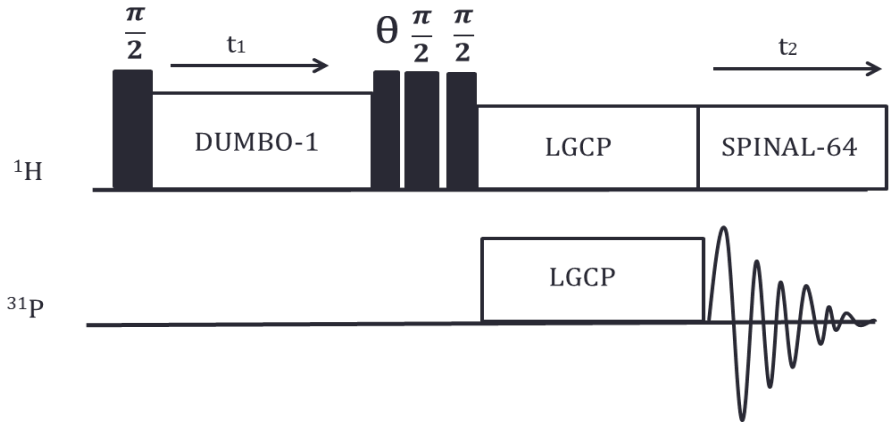


Figure 6.3: Pulse sequence used to acquire the ^{1}H-^{31}P correlation spectra.

typical experimental times between 3 - 5 days. The ^{1}H-^{31}P correlation spectra are all plotted using 100 contour levels linearly arrayed between the maximum peak height and 2% of this value.

6.3 Results and Discussion

Many characteristic features present in the proton spectra of both synthetic hydroxyapatite and bone tissue have already been identified. Usually the most prominent feature observed in the spectra of these materials is a sharp peak present at roughly 0 ppm that corresponds to the OH^- of the hydroxyapatite[96–104;107;108]. These OH^- groups stack in columns and are sufficiently far removed from each other that little significant hydrogen bonding takes place leading to a low chemical shift value[104]. In the proton spectra of many types of calcium phosphates broad peaks are seen between 5-6.5 ppm that are ascribed to surface adsorbed water[108]. Detailed knowledge of the surface environment of hydroxyapatite is crucial to understanding its reactivity and is of even greater importance for nanoparticles that contain a comparatively greater quantity of surface material.

Solid-state NMR has been used on a variety of occasions to attempt to differentiate signals arising from the bulk mineral and its surface[96;101;102;107]. A broad contribution to the proton spectrum typically observed between 8-17 ppm is assigned to HPO_4^{2-} [96;99;101–103], which is generally believed to form a disordered surface region[96;101;102]. Hydroxyapatite is prone to ionic substitution[104] and potentially some HPO_4^{2-} could be incorporated as defects into the bulk material. A recent study assigned a peak present at 3.1 ppm to HPO_4^{2-} defects in the crystal structure[102].

In addition to the peaks already described, the spectra of hydroxyapatite nanoparticles often display additional narrow lines between 1 and 2 ppm[97;98;101;102;108] whose assignment has been subject to some debate. A peak at 1.1 ppm was assigned to highly structured water at the surface, aligned with the hydroxyl columns of the bulk apatite material[102]. Previously this peak had been attributed to the presence of disordered hydroxyl groups which experience a greater amount of hydrogen bonding due to water molecules occupying some of the hydroxyl sites.[98] This suggestion is supported by the fact that fluorohydroxyapatites, which have more strongly hydrogen bonded hydroxyl groups due to the presence of fluoride, also show a peak in this region[108]. The ability of surface water to migrate into the hydroxyapatite crystal lattice by proton transfer with the hydroxide ions has also been separately demonstrated.[104]

Using the previous literature studies we may attempt to identify all the peaks in the ^{1}H spectrum (Figure 6.4) of the hydroxyapatite nanoparticles. The ^{1}H spectrum shows a narrow peak present at 0 ppm that can immediately be assigned to the OH^- of hydroxyapatite. The intensity between 5-8 ppm is principally attributed to surface adsorbed water. The broad tail of this peak that extends out to above 10 ppm is probably caused by a disordered surface

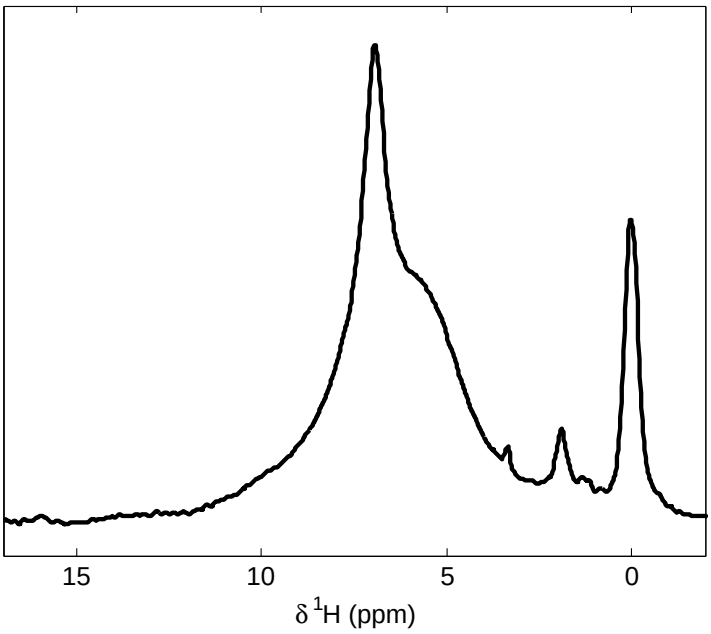


Figure 6.4: ^{1}H spectrum of the HAp nanoparticles.

layer of HPO_4^{2-}. Small peaks at 1.1 and 1.8 ppm could be due to highly structured water along the hydroxide columns and the small peak at 3.3 ppm may be due to HPO_4^{2-} defects present in the bulk material.

The ^{1}H-^{31}P correlation spectrum displayed in Figure 6.5 only gives peaks for protons that are in close proximity to phosphorous nuclei and so differs considerably in appearance from a simple proton direct excitation. An intense peak between 0-2 ppm can be assigned to correlations between phosphate and the OH^- protons in the apatite or with water structured along these channels. There is also a broad but less intense peak covering a proton range of 5-15 ppm. This is most likely present due to correlations between the surface adsorbed water and phosphate groups and the presence of HPO_4^{2-} at the crystal surface. In the skyline projection of the direct dimension two different types of phosphorous environments can be identified. There is a dominant narrow peak that corresponds to phosphate present in the bulk hydroxyapatite. This is superimposed over a much broader peak which is most likely caused by phos-

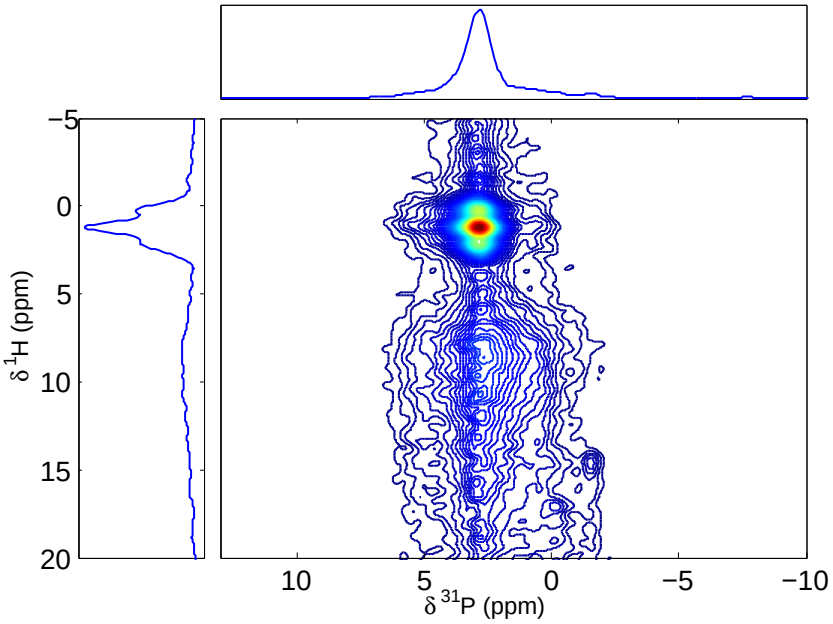


Figure 6.5: ^{1}H-^{31}P correlation spectrum of the HAp nanoparticles. Skyline projections of both dimensions are also displayed.

phate groups at or near the nanoparticle surface. A greater degree of disorder would be expected from phosphate groups in the surface region and this would result in a larger distribution of chemical shift values and therefore give rise to a broadened peak.

This spectrum of the hydroxyapatite nanoparticles provides a useful comparison for the hydroxyapatite-dispersant molecule composite systems. Any differences observed between this spectrum and the spectra of the composite materials must occcur due to the addition of the polymer. It is also possible that features may be observed that indicate an interaction between the polymer and the surface of the nanoparticle.

Figure 6.6 displays the ^{1}H-^{31}P correlation spectrum of HAp/[PLA]-[COONa] composite material. The intense signal with a proton shift between 0-2 ppm and the broad peak between 5-16 ppm that were previously observed in the

spectrum of HAp are still visible. However, an additional feature is present in the spectrum. There is a stripe of intensity that occurs at a slightly lower phosphorous chemical shift ($\approx$ 1.5 ppm) and extends over a range of higher proton shift values ($\approx$ 5-16 ppm). Within this region of intensity there is a sharp peak that appears at around 11 ppm. The high proton chemical shift values of this additional peak suggests that it originates from a strongly hydrogen bonded environment. These changes are likely caused by the binding of the polylactic acid molecule to the nanoparticle resulting in a modification of the hydroxyapatite surface. Figure 6.7 shows the spectrum of the HAp/[PLA]-[$C_6H_9O_4$] composite material. The same additional feature (the stripe at lower phosphorous ppm and a small peak in the proton dimension at around 11 ppm) can be seen in this spectrum as was previously observed in the spectrum of the HAp/[PLA]-[COONa] sample.

In general, the chemical shift is very sensitive to the electronic environment and if the dispersant molecule was binding to the surface via the head group then changes in the spectrum upon changing the head group may be expected. However, in this case altering the head group between a carboxylate group (HAp/[PLA]-[COONa]) and an isosorbide group which contains an alcohol group (HAp/[PLA]-[$C_6H_9O_4$]) generated the same additional features in the spectrum. This implies that the mode of interaction of both the [PLA]-[COONa] and the [PLA]-[$C_6H_9O_4$] molecules with the HAp surface was in fact quite similar.

To investigate the binding mechanism further nanoparticles with attached dispersant molecules containing an aliphatic chain were studied. The spectrum in Figure 6.8 shows the ^{1}H-^{31}P correlation of the HAp/[$C_{12}H_{23}$]-[$C_2H_3(COOH)_2$] sample whose dispersant contained a bicarboxylate head group and an aliphatic

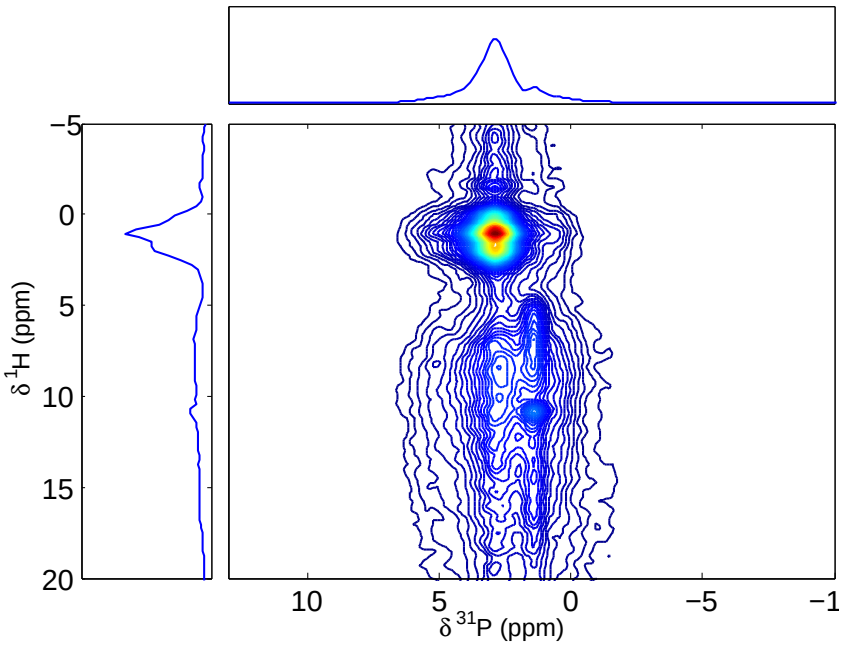


Figure 6.6: ^{1}H-^{31}P correlation spectrum of the HAp/[PLA]-[COONa] sample. Skyline projections of both dimensions are also displayed.

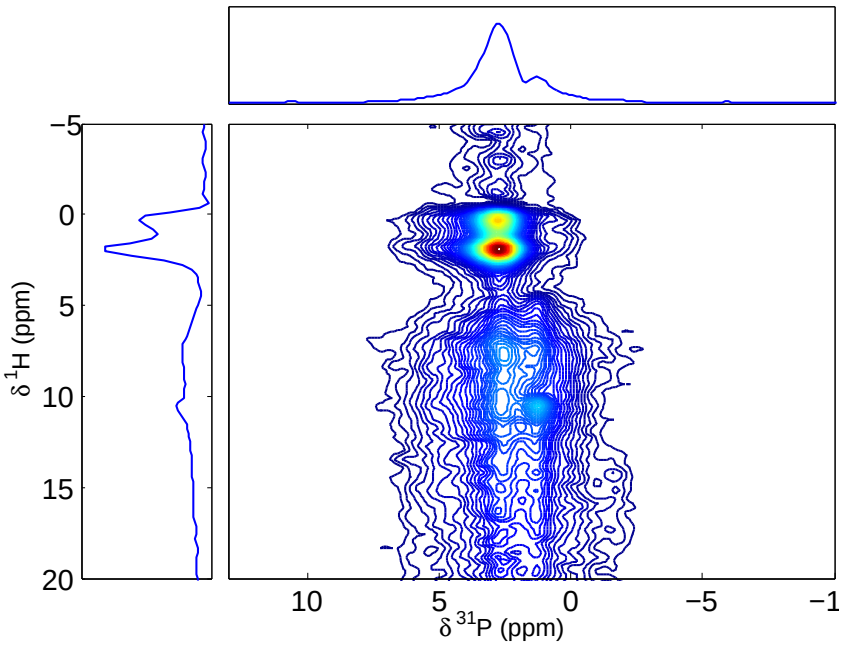


Figure 6.7: ^{1}H-^{31}P correlation spectrum of the HAp/[PLA]-[$C_6H_9O_4$] sample. Skyline projections of both dimensions are also displayed.

chain. The spectrum is dominated by a peak that appears just below 10 ppm in the proton dimension which completely overshadows the usual signals originating from the hydroxyapatite. As it is not present in the spectrum of hydroxyapatite alone it must be caused by the addition of the $[C_{12}H_{23}]$-$[C_2H_3(COOH)_2]$ to the nanoparticles. The $[C_{12}H_{23}]$-$[C_2H_3(COOH)_2]$ molecule contains a bicarboxylate group that is expected to bind strongly to the surface and this could mean that it forms a greater number of contacts with the HAp surface or that the distances over which the polarisation transfer must take place are much reduced. Either of these factors may cause an increase in peak intensity during a cross polarisation type experiment.

Figure 6.9 shows the ^{1}H-^{31}P correlation spectrum of the HAp/$[C_{11}H_{23}]$-$[C_7H_9O_5]$ composite material. In this case the dispersant polymer molecule contains an ester isosorbide head group and an aliphatic chain. The spectrum resembles the HAp spectrum (see Figure 6.5) except that it contains two extra peaks. These two peaks appear at lower phosphorous ppm ($\approx$ -0.5 and -1.7 ppm) and higher proton ppm ($\approx$ 13.25 and 15.5 ppm) and are attributed to the addition of the dispersant to the nanoparticle. The spectra in Figures 6.9 and 6.8 are quite dissimilar to each other and so for the aliphatic chain molecules clear differences can be observed in the spectrum when the head group is altered from a carboxylate group ($[C_{12}H_{23}]$-$[C_2H_3(COOH)_2]$) to an ester isosorbide group ($[C_{11}H_{23}]$-$[C_7H_9O_5]$).

All four of ^{1}H-^{31}P correlation spectra of the composite materials show extra features compared to the results for the nanoparticles alone. However, for the composites with the two dispersant molecules with the aliphatic chains (HAp/$[C_{12}H_{23}]$-$[C_2H_3(COOH)_2]$ and HAp/$[C_{11}H_{23}]$-$[C_7H_9O_5]$) the appearance of the spectrum changes when the head group is changed from carboxy-

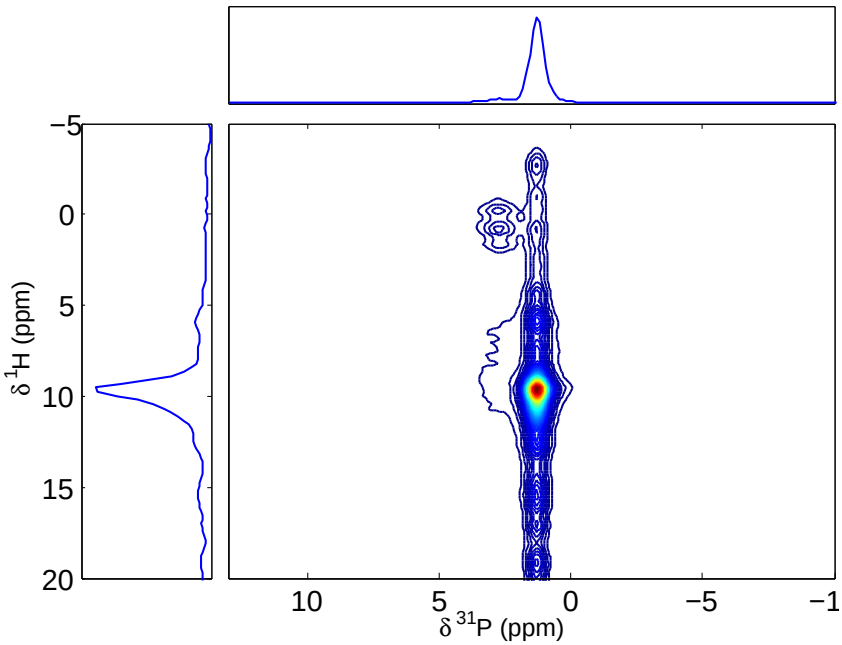


Figure 6.8: ^{1}H-^{31}P correlation spectrum of the HAp/[$C_{12}H_{23}$]-[$C_2H_3(COOH)_2$] sample. Skyline projections of both dimensions are also displayed.

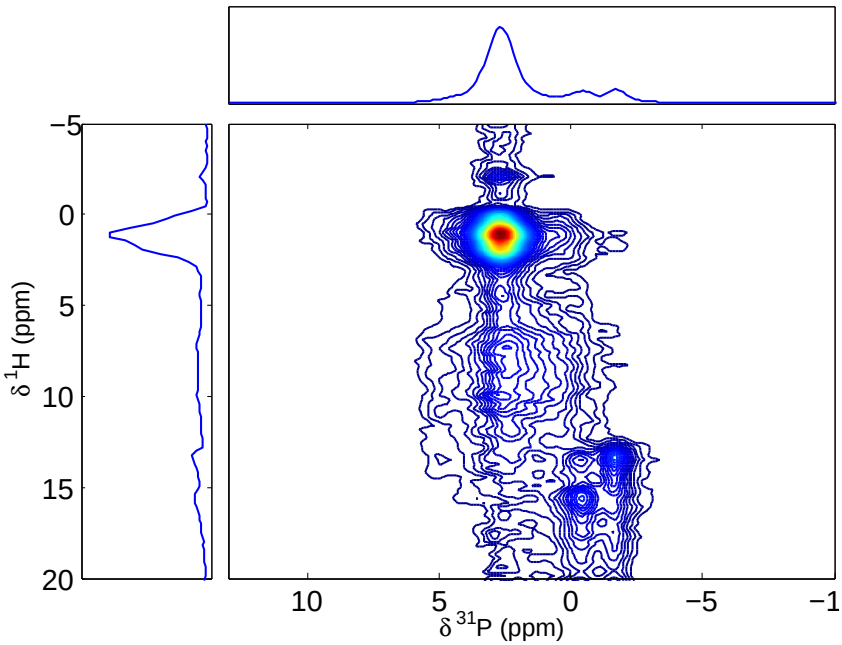


Figure 6.9: ^{1}H-^{31}P correlation spectrum of the HAp/[$C_{11}H_{23}$]-[$C_7H_9O_5$] sample. Skyline projections of both dimensions are also displayed.

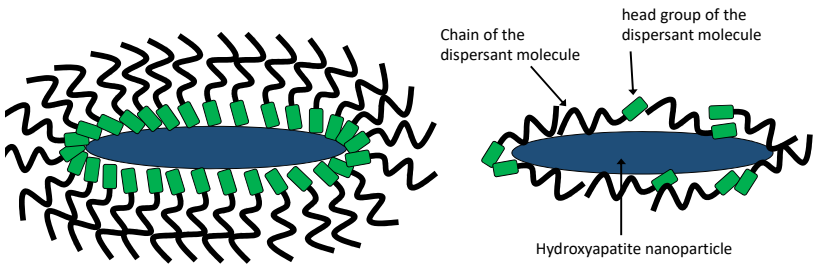


Figure 6.10: Diagram displaying the possible modes of binding of the dispersant molecule to the surface hydroxyapatite nanoparticle. Left: The dispersant molecule binds via its head group. Right: The dispersant molecule binds via the chain of the molecule. These diagrams are not drawn to scale and are for illustration purposes only.

late (HAp/[$C_{12}H_{23}$]-[$C_2H_3(COOH)_2$]) to an ester isosorbide (HAp/[$C_{11}H_{23}$]-[$C_7H_9O_5$]). This would be the expected result if the molecule was interacting with the HAp nanoparticles via its head group. In contrast to this, experiments on the two PLA chain dispersant composite materials produced spectra that were different to the hydroxyapatite but similar to each other. The fact that little change was observed in the spectra on moving from a carboxylate head group (HAp/[PLA]-[COONa]) to an isosorbide head group (HAp/[PLA]-[$C_6H_9O_4$]) suggests that these dispersants actually interact with the nanoparticles via the PLA chain of the molecule. In this scenario changing the head group would be expected to have little effect on the spectrum. See figure 6.10 for an illustration of these different modes of binding

It is also the case that the aliphatic chain molecules are more hydrophobic than the PLA based molecules. This could provide an extra driving force favouring attachment via the head group. It is easy to imagine that during the synthesis in an aqueous environment the aliphatic chains preferential orientate alongside each other generating a micellar type structure with the dispersants attached to the nanoparticle via the head group. The PLA molecules are less hydrophobic than the aliphatic chains and so may experience less of a driving force to align

themselves side by side. If, as the NMR spectra suggest, they are interacting with the nanoparticles via the PLA chain then it is probable that the polymer chains lie flat along the nanoparticles surface. From an applications perspective a micellar type of structure represents the desirable synthetic outcome as these structures are expected to disperse most effectively.

Further proof of the tendency of the PLA chain based dispersants to lie flat on the surface of nanoparticles was obtained from NMR spectra of the sample of HAp/[PLA_{ex}]-[$C_6H_9O_4$]. This dispersant molecule has the same headgroup and type of polymer chain as the [PLA]-[$C_6H_9O_4$] but with a chain length that is roughly three times longer. Figure 6.11 displays the ^{1}H-^{31}P correlation spectrum of this sample and the same stripe present at lower phosphorous chemical shift can be observed (seen previously in the correlation spectra of both HAp/[PLA]-[COONa] and HAp/[PLA]-[$C_6H_9O_4$]). However, in the spectrum of HAp/[PLA_{ex}]-[$C_6H_9O_4$] this feature is increased in intensity (in comparison to the spectra of the HAp/[PLA]-[COONa] and HAp/[PLA]-[$C_6H_9O_4$] samples) and is also resolved into three regions of proton intensity. The peak at $\approx$ 10 ppm in the proton dimension is still present and as before can be assumed to originate from an hydrogen bonded proton. The area of intensity within the stripe with a proton shift of $\approx$ 6-7 ppm can be assigned to correlations with water. However, there is also peak with a proton shift of $\approx$ 5 ppm that was not resolved in any of the previous spectra.

A plausible origin of this peak is that it represents a correlation between phosphate at the nanoparticles surface and a methoxy proton of the PLA chain. The spectrum in Figure 6.12 displays the ^{1}H spectrum of the HAp/[PLA_{ex}]-[$C_6H_9O_4$] sample and the most prominent features are due to the PLA component of the sample. The peak at $\approx$ 1 ppm correspond to the methyl protons

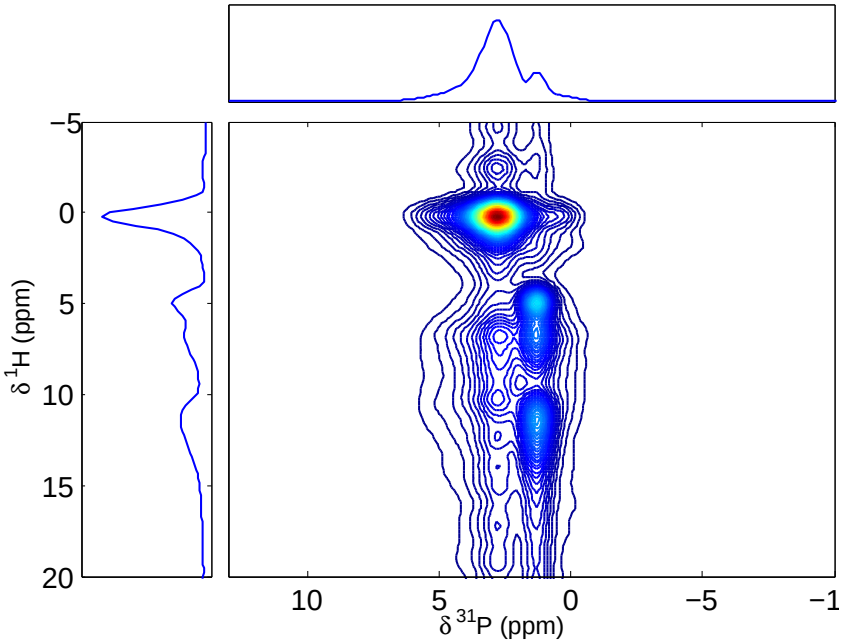


Figure 6.11: ^{1}H-^{31}P correlation spectrum of the HAp/[PLA$_{ex}$]-[$C_6H_9O_4$] sample. Skyline projections of both dimensions are also displayed.

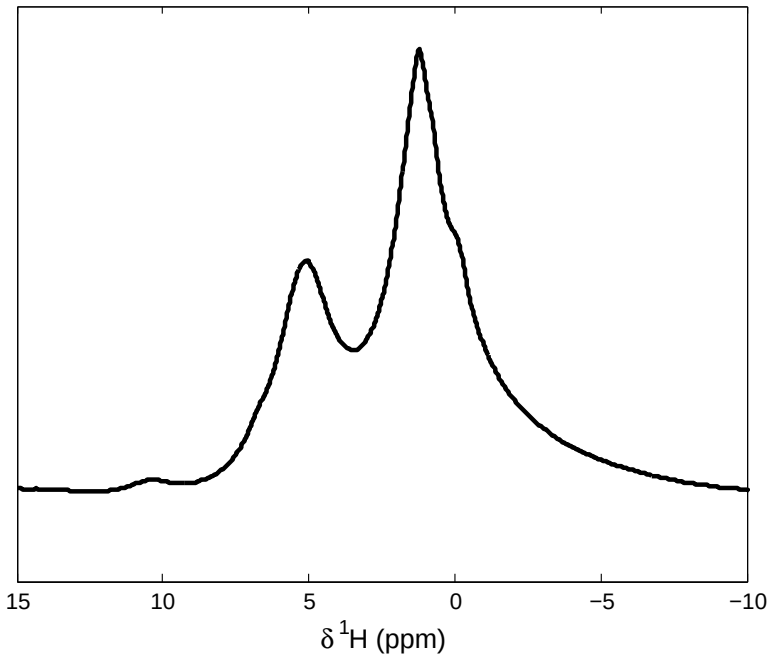


Figure 6.12: ^{1}H spectrum of HAp/[PLA$_{ex}$]-[$C_6H_9O_4$].

on the PLA chain and the peak at ≈ 5 ppm can primarily be attributed to the methoxy protons in the chain. The presence of a correlation between phosphate (which is only present in the HAp nanoparticle) and methoxy group of the polymer chain suggests that the polymer chain is in close proximity to the surface of the nanoparticle and therefore probably lies flat along the nanoparticle surface. This correlation is only clearly visible in HAp/[PLA_{ex}]-[$C_6H_9O_4$] in comparison to composites containing the other PLA dispersants due to the longer length of the polymer chain.

6.4 DNP Experiments

DNP can be used to drastically increase the signal intensity in NMR spectra by transferring the much larger polarisation of an unpaired electron to the proton nuclei in the sample (see Section 3.5). This enhanced polarisation can then spread, via spin diffusion, through the network of dipolar coupled protons and may subsequently be transferred to other nuclei. To obtain a DNP enhancement a polarising agent containing unpaired electrons must be incorporated into the NMR sample and this is frequently achieved by wetting the surface of the sample with a solution containing radicals.

This method of sample preparation results in radicals congregating at the surface of the sample, which will produce a preferential enhancement of signals emanating from surface species. However, although the nuclei at the surface will show enhanced signal intensity, a lower enhancement of signals from the sample bulk may be observed. This occurs because the majority of the polarisation will have been lost to various relaxation effects before sufficient time has elapsed for the magnetisation to be transferred to the nuclei in the bulk of the sample. Enhancement of surface species is desirable when the surface is the

primary source of interest, for example, in solid catalysts the surface species typically govern the catalyst's activity and may be of more interest than the constituents of the bulk. In contrast, spectra acquired from standard NMR experiments are usually dominated by signals originating from the bulk as this is the main constituent of the sample and the surface signals are often very low in intensity and may not be observed.

Samples of HAp/[PLA]-[$C_6H_9O_4$] and HAp/[$C_{12}H_{23}$]-[$C_2H_3(COOH)_2$] were studied using DNP enhanced solid-state NMR. One advantage of using DNP is that experiments can be carried out with much shorter acquisition times (due to increased signal intensity). The ^{1}H-^{31}P correlation spectra displayed in the previous section were acquired over the course of three days but with DNP enhancement shorter acquisition times could be used. Additionally, the motivation for studying the composite materials was to elucidate the binding mechanism of the dispersant molecules to the hydroxyapatite surface. DNP may assist in gaining further understanding of the mode of binding as it preferentially enhances surface signals.

6.4.1 Experimental Method

Samples of HAp/[PLA]-[$C_6H_9O_4$] and HAp/[$C_{12}H_{23}$]-[$C_2H_3(COOH)_2$] were prepared by wetting 30 mg of each sample with 30 μL of 10 mmol Amupol solution with 90/10% by volume D_2O/H_2O. When not in use samples were stored in the freezer to slow the decomposition of the radical.

All the DNP experiments were performed on a wide-bore AVIII 600 MHz (^{1}H Larmor frequency) Bruker spectrometer equipped with a 395 GHz gyrotron, a transmission line and a low temperature 3.2 mm HX MAS probe operating at $\approx$107 K.

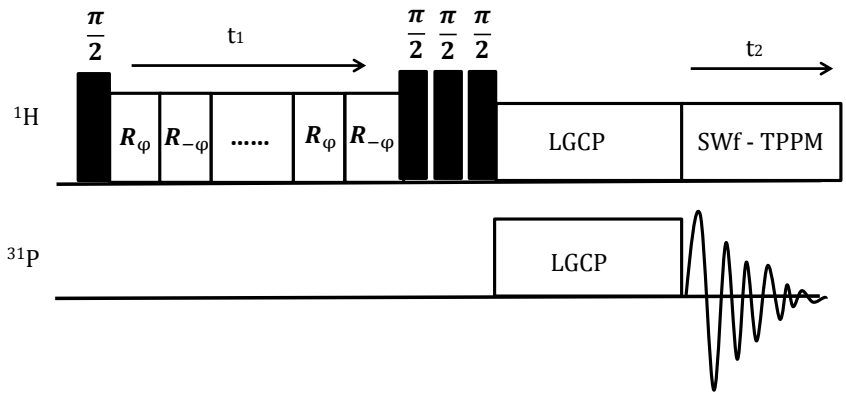


Figure 6.13: Pulse sequence used to acquire the DNP enhanced ^{1}H-^{31}P correlation spectra. $[R_{\phi}][R_{-\phi}] = [90_{45}90_{135}90_{45}][90_{-45}90_{-135}90_{-45}]$

The ^{1}H-^{31}P correlation spectra were acquired using the pulse sequence displayed in Figure 6.13. The principal difference between this sequence and the sequence displayed in Figure 6.3 is that an R-sequence was applied in the indirect dimension to carry out the homonuclear proton decoupling. The basic element of the R-sequence, R_{ϕ}, was a composite pulse of the form $90_{45}90_{135}90_{45}$. This sequence was used instead of DUMBO as it produced superior resolution under the conditions present in the DNP experiment.

All the DNP spectra were recorded at a MAS rate of 12 kHz with a recycle delay of 5 s. The 90° pulse length was set to 2.6 μs and SWf-TPPM decoupling[17] was applied to the proton channel during acquisition. TPPI was used to generate pure absorption lineshapes. The spectra were acquired using eight scans and the number of complex data points acquired in the direct and indirect dimension was 1024 and 150 respectively. For LGCP an offset of -37137 Hz was used and the contact time was set to 4.12 ms.

6.4.2 Results

Figure 6.14 displays the direct excitation spectra of proton nuclei in the sample of HAp/[PLA]-[$C_6H_9O_4$] recorded with and without application of microwave

irradiation. The peaks in the spectrum correspond to water (broad peak ≈ 7 ppm) and the OH group of the hydroxyapatite (narrow peak ≈ 0 ppm). A roughly five fold increase in signal intensity was observed due to DNP enhancement.

Figure 6.15 displays the direct excitation phosphorous spectra with and without microwave irradiation and an enhancement of three was observed. The obtained DNP enhancement would depend on the proximity of the nucleus to the polarising agent. The phosphorous would therefore be expected to show a lower enhancement as it is primarily located in the core of the coated nanoparticle further away from the polarising agent. Similar DNP enhancements were obtained for the HAp/$[C_{12}H_{23}]$-$[C_2H_3(COOH)_2]$ sample.

The ^{1}H-^{31}P correlation spectrum of the HAp/[PLA]-$[C_6H_9O_4]$ sample acquired with DNP enhancement is displayed in Figure 6.16. Figure 6.17 shows the corresponding DNP enhanced, correlation spectrum for the sample of HAp/$[C_{12}H_{23}]$-$[C_2H_3(COOH)_2]$. To plot the spectra 100 contour levels, linearly spaced between the maximum peak height and 5% of this value, were used. Both these spectra look substantially different to the solid-state NMR spectra for the same samples recorded in Figures 6.7 and Figures 6.8.

Differences between the DNP enhanced spectra and the standard solid-state NMR spectra are to be expected for a variety of reasons. Firstly, the sample is prepared for DNP by wetting with a solution of 90/10% D_2O/H_2O and this could lead to changes in the intensity of the water peak normally found at ≈ 6 ppm in the proton dimension. Secondly, the DNP experiments are carried out at a much lower temperature of ≈ 107 K in comparison to standard solid-state NMR experiments which are usually acquired close to room temperature.

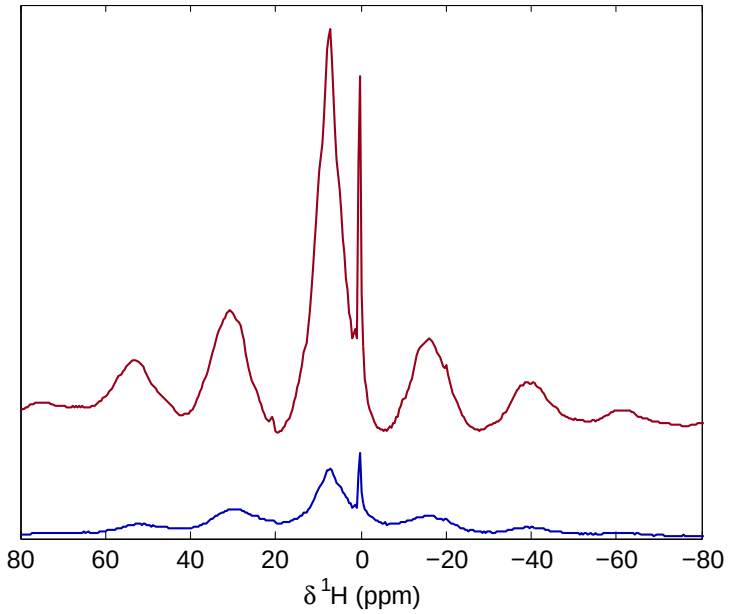


Figure 6.14: ^{1}H spectra of the HAp/[PLA]-[$C_6H_9O_4$] sample recorded with the microwaves off (blue) and the microwaves on (red)

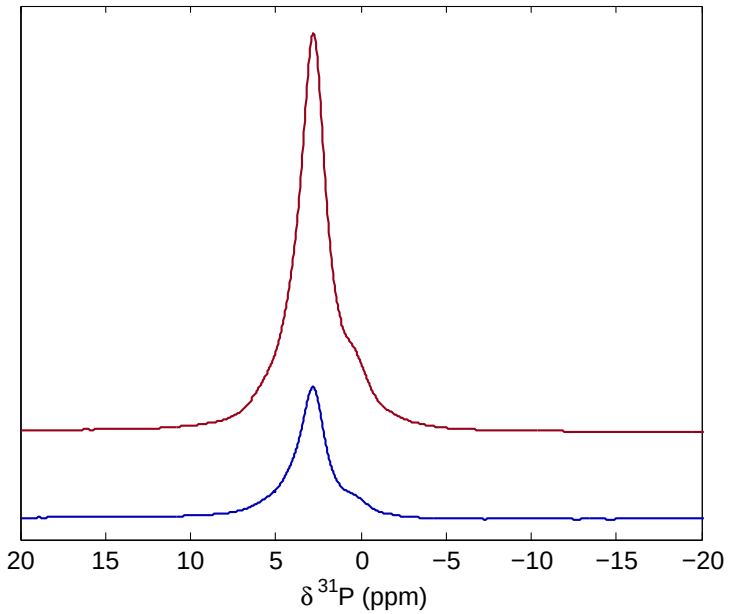


Figure 6.15: ^{31}P spectra of the HAp/[PLA]-[$C_6H_9O_4$] sample recorded with the microwaves off (blue) and the microwaves on (red)

Finally, it is important to remember that the radical polarising agent, which is added to the sample, will congregate at the sample surface. This will lead to a stronger enhancement of the surface species and therefore signals emanating from these regions will dominate the spectra. This effect should be beneficial for studying the interaction of the dispersant molecule with the hydroxyapatite as these interactions occur primarily close to the surface.

The standard solid-state NMR correlation spectrum of the uncoated hydroxyapatite nanoparticles (see Figure 6.5) displayed two different types of phosphate. A broad peak was observed that was attributed to surface phosphate whereas a narrow signal was attributed to more ordered phosphate within the bulk of the material. In the DNP enhanced spectra of the coated nanoparticles displayed in Figures 6.16 and Figures 6.17 a broad peak in the phosphorous dimension can be observed. This implies that it is the disordered phosphate, present at the surface of the hydroxyapatite material that is being enhanced. In both spectra this broad phosphate signal correlates with signals in the proton dimension for water ($\approx$ 6 ppm) and hydrogen bonded protons ($\approx$ 15 ppm), both of which are likely to be present at the surface of the hydroxyapatite core of the material.

Using standard solid-state NMR, peaks observed at 10-11 ppm in the correlation spectra of samples HAp/[PLA]-[$C_6H_9O_4$] and HAp/[$C_{12}H_{23}$]-[$C_2H_3(COOH)_2$] were previously assigned to hydrogen bonded protons at the hydroxyapatite surface. The higher chemical shift for these protons obtained under DNP was believed to occur principally due to temperature differences. The DNP spectra were recorded at a temperature of around 100 K whereas the standard solid-state NMR spectra were acquired close to room temperature.

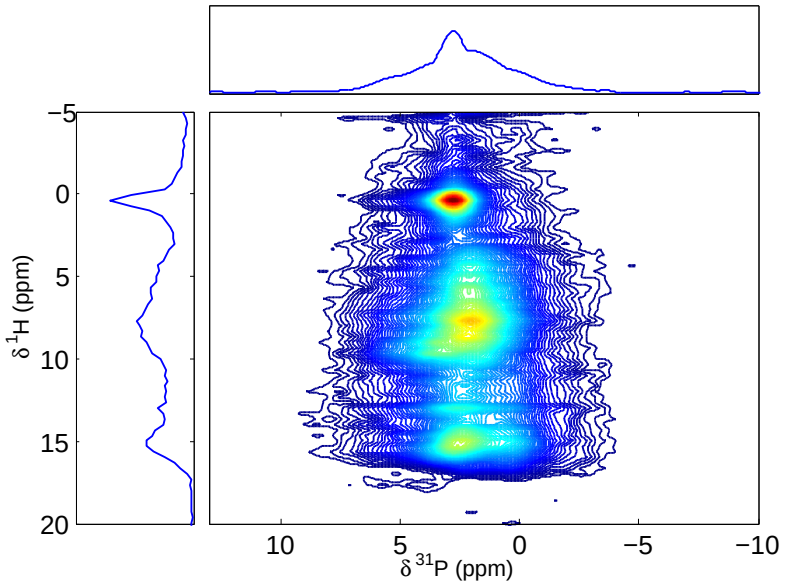


Figure 6.16: ^{1}H-^{31}P correlation spectrum of the HAp/[PLA]-[$C_6H_9O_4$] sample acquired using DNP. Skyline projections of both dimensions are also displayed.

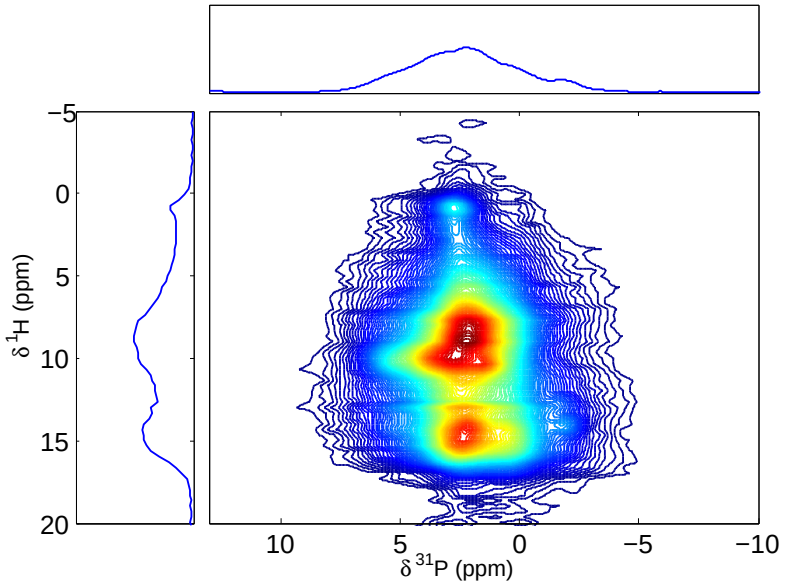


Figure 6.17: ^{1}H-^{31}P correlation spectrum of the HAp/[$C_{12}H_{23}$]-[$C_2H_3(COOH)_2$] sample acquired using DNP. Skyline projections of both dimensions are also displayed.

The DNP enhanced spectrum of the HAp/[PLA]-[$C_6H_9O_4$] sample differs from the HAp/[$C_{12}H_{23}$]-[$C_2H_3(COOH)_2$] spectrum because it contains a narrow peak close to 0 ppm in the proton dimension that correlates with a narrow peak in the phosphorous dimension at slightly higher ppm than the disordered phosphate signal (this can be seen clearly in the skyline projection of the direct dimension). This peak can be attributed to the hydroxyl protons of the bulk hydroxyapatite material. This signal emanating from the bulk is significantly lower in intensity in the DNP enhanced spectrum of the HAp/[$C_{12}H_{23}$]-[$C_2H_3(COOH)_2$] sample. These results provide information about the surface structure of the samples.

On the basis of the previously acquired solid-state NMR spectra it has been suggested that the HAp/[$C_{12}H_{23}$]-[$C_2H_3(COOH)_2$] forms a micellar-type structure whereas the polymer chains of the HAp/[PLA]-[$C_6H_9O_4$] sample lie flat along the hydroxyapatite surface. The DNP enhanced spectra provide further support for these conclusions. If the polymer molecules lie flat along the surface of the nanoparticle (as appears to be the case for HAp/[PLA]-[$C_6H_9O_4$] sample) the distance the polarisation has to travel to reach the bulk of the particle is relatively short. This means that the magnetisation enhancement will be transferred into the bulk material before significant relaxation has occurred and a signal for the the hydroxyl protons of the hydroxyapatite (at ≈ 0 ppm) would be observed. If the coating molecules attach to the surface via their headgroup and have their chains aligned perpendicular to the nanoparticle's surface (this is the suspected configuration of the HAp/[$C_{12}H_{23}$]-[$C_2H_3(COOH)_2$] sample) then the radicals will be positioned much further away from the inorganic hydroxyapatite core of the composite material. In this situation it is unlikely that the enhanced polarisation will extend into the bulk hydroxyapatite and this is probably the reason why it is principally the hydroxyapatite surface

signals that are observed in Figure 6.17. Application of DNP to study these materials provided further evidence for the changes occurring at the surface with different dispersant molecules. Additionally the spectra used to draw these conclusions could be acquired in a much faster time frame.

6.5 Conclusions

Spectra of hydroxyapatite nanoparticles were recorded and analysed and various proton environments commonly associated with hydroxyapatite type materials were identified. The spectra of the HAp nanoparticles were compared to five hydroxyapatite polymer composite materials containing different dispersant molecules. All the composite materials displayed differences in their spectra in comparison to the nanoparticles alone. The correlation spectra of the two composites containing PLA chain dispersant molecules with different head groups appeared similar to each other whereas the spectra of the composites containing the two aliphatic chain dispersants with different head groups differed from each other. On this basis it was suggested that the aliphatic chain molecules bind to the surface of the hydroxyapatite via their head group forming a structure reminiscent of a micelle. The PLA based dispersants are believed to interact with the surface of the particle via their chain and so lie flat along the surface. This hypothesis was further corroborated by the observation of a peak in the sample of HAp/[PLA_{ex}]-[$C_6H_9O_4$] indicating correlation between the proton sites in the PLA polymer chain and phosphate at the nanoparticle surface. It was also suggested that the reasons for these differences may relate to the relative hydrophobicity of the dispersant chains. As the micelle type conformation is preferred for efficient dispersal of these materials this information should help guide the creation of suitable dispersant molecules for these systems in the future.

DNP enhanced ^{1}H-^{31}P correlation spectra have been carried out on two of the coated hydroxyapatite nanoparticle samples (HAp/[PLA]-[$C_6H_9O_4$] and HAp/[$C_{12}H_{23}$]-[$C_2H_3(COOH)_2$]). The use of DNP resulted in preferential enhancement of the phosphate signals at the surface of the hydroxyapatite material. The spectra also provided further support for the conclusion that the PLA chains lie flat along the surface of the nanoparticle while the HAp/[$C_{12}H_{23}$]-[$C_2H_3(COOH)_2$] composite adopts a micellar configuration.

There is the potential to use DNP in future work to provide greater details on the interaction between the organic coating materials and the hydroxyapatite nanoparticles in these composite materials. The acquisition of ^{31}P-^{13}C correlation spectra of these materials using a double CP experiment has been considered as it has great potential for studying the changes occurring at the hydroxyapatite surface upon binding of the dispersant molecule. However, this was found to be totally infeasible using standard solid-state NMR because the available signal intensity was too low. The use of DNP may provide sufficient signal intensity to make such experiments possible.

Chapter 7

Summary and Outlook

During the course of this thesis a wide variety of solid-state NMR techniques have been applied to study a range of new materials.

The domain sizes of diblock polymers were measured using spin diffusion experiments carried out under fast MAS. In this regime there was sufficient resolution to acquire and analyse directly detected proton spectra without implementation of proton homonuclear decoupling. For each sample a series of two dimensional exchange spectra were recorded with increasing mixing times. The change in peak intensity with increasing mixing time was monitored and used to extract the polymer domain size according to the initial rate approximation. The domain sizes obtained from NMR were comparable to the results of TEM and SAXS measurements of the same samples.

For the PMMA-b-PS samples it was also possible to internally calibrate the spin diffusion coefficient from the same data used to obtain the polymer domain sizes. The spin diffusion coefficients determined at 60 kHz MAS were found to be much reduced in comparison to literature values determined at much lower spinning speeds. Additionally, the validity of applying a T_1 correction in

conjunction with the initial rate approximation was investigated by simulating spin diffusion experiments using a home written Matlab program.

The spin diffusion profiles analysed in this work showed two separate decays, a faster decay corresponding to intra-domain and a slower decay caused by inter-domain spin diffusion. One of the samples, which lacked any discernible phase separation, displayed a single, rapid decay. Comparison of the extent of intra-domain magnetisation exchange with expected equilibrium magnetisation levels may provide a method of quantifying the extent of phase separation in partially phase separated samples.

All of the work so far has been carried out on diblock polymers where both domains are below the glass transition at room temperature. Some of the original NMR studies of block copolymers were carried out using samples that contained both glassy and rubbery domains. It may be informative to study the spin diffusion behaviour of these systems under fast MAS. The spin diffusion coefficient of a mobile polymer is already much lower than a glassy polymer due to motional averaging of dipolar couplings and application of MAS would be expected to lower this even further. However, temperature changes are likely to have a greater effect on polymers containing mobile sections. This should be considered when designing experiments for use with such samples and it may be necessary to mitigate temperature changes caused by the frictional heating that occurs at high MAS rates.

Further development of the Matlab program that simulates the outcomes of spin diffusion experiments would be helpful. In its current form the program re-distributes magnetisation along a line of points and is therefore suitable for simulating lamellar system. It should be fairly trivial to extend this to cover

cylindrical and spherical morphologies by adapting the program into either a grid or a cube of points. Although the run time associated with these simulation would lengthen correspondingly. With further development it should be possible to use the simulation program to obtain intrinsic T_1 values and domain sizes by fitting simulated data to experimental saturation-recovery and spin diffusion results. This would provide a method of analysing experimental data without the need for T_1 correction of the initial rate approximation, which has previously been a source of contention.

The changes in the spin diffusion coefficient of a sample of polystyrene have been studied under a variety of experimental conditions including varying MAS rate, temperature changes and introduction of homonuclear dipolar recoupling sequences into the experimental mixing time. Increasing MAS rate was found to decrease the rate of spin diffusion and an attempt was made to fit these changes to a functional form. Fitting changes in the diffusion coefficient to an equation may have future applications in obtaining spin diffusion coefficients of diblock polymers that cannot be internally calibrated according to the methods outlined in Chapter 4. It may be possible to obtain diffusion coefficients and domain sizes using spin diffusion experiments carried out at two different spinning speeds.

In order to study the effect temperature changes have on the spin diffusion coefficient it was necessary to carry out a temperature calibration of the MAS probe using a sample of lead nitrate. Experiments were acquired at three different temperatures and changing temperature was determined to have negligible effect on the spin diffusion coefficient of polystyrene over a reasonable temperature range.

The introduction of RFDR into the mixing time of the spin diffusion experiment was found to substantially increase the spin diffusion coefficient. However, application of the $SR6_6^2$ sequence was less successful due to the rapid rate of signal loss that precluded any useful analysis. It may be possible to find other recoupling sequences that result in a higher spin diffusion coefficient and a lower rate of signal loss.

Hydroxyapatite nanoparticles and a range of hydroxyapatite/organic dispersant molecule composite nanoparticles have been studied using solid-state NMR. In particular, ^{1}H-^{31}P correlation spectra were critical in the study of the changes occurring at the surface of the hydroxyapatite due to the binding of the dispersant molecules. The correlation spectra displayed similar features for all the composites containing PLA dispersant molecules regardless of the choice of head group. Whereas, the spectra containing the dispersant molecules with an alkyl chain showed clear changes upon alteration of the head group and were also different from the spectra of the samples containing PLA dispersant. This led to the conclusion that the PLA dispersants lie flat along the surface of the nanoparticle while the aliphatic chain dispersants form a micellar type structure with the hydroxyapatite nanoparticle. This was corroborated by evidence in the spectrum of a hydroxyapatite nanoparticle coated with a longer chain PLA which appeared to show a signal from the PLA chain correlating with phosphate in the hydroxyapatite.

These results appear reasonable when the relative hydrophobicities of the dispersants are considered and this information may help guide the creation of other coated hydroxyapatite materials. Future work could involve studying hydroxyapatite coated with different dispersants, including dispersants that have hydrophobicities intermediate between that of PLA and an alkyl chain.

Polycaprolactone is an appropriate example of such a dispersant and it may be interesting to study its mode of interaction with the surface of hydroxyapatite nanoparticles.

DNP was also used to study two of the coated hydroxyapatite nanoparticles. As expected, the surface regions of the hydroxyapatite nanoparticle were enhanced by the DNP. The signal for the bulk hydroxyl groups of the hydroxyapatite were present in much greater extent in the PLA coated material in comparison to the alkyl chain coated material. This supports the previous conclusion suggesting that the PLA chains lie flat along the nanoparticle while the alkyl chains align perpendicular to the surface. There are a wide range of experiments that could be carried out in the future that have been made feasible due to the enhanced signal intensities available with DNP. Acquisition of ^{31}P-^{13}C correlation spectra would be useful to study the interaction between the organic dispersant and the surface of the hydroxyapatite. These experiments would have prohibitively long acquisition times using standard NMR but this may be reduced considerably using DNP.

Bibliography

[1] E. M. Purcell, H. C. Torrey and R. V. Pound, *Physical Review*, 1946, **69**, 37–38.

[2] F. Bloch, W. W. Hansen and M. Packard, *Physical Review*, 1946, **69**, 127–127.

[3] R. R. Ernst and W. A. Anderson, *Review of Scientific Instruments*, 1966, **37**, 93–102.

[4] W. P. Aue, E. Bartholdi and R. R. Ernst, *The Journal of Chemical Physics*, 1976, **64**, 2229–2246.

[5] D. M. Grant and R. K. E. Harris, *Encyclopedia of Nuclear Magnetic Resonance, Volume 1, Historical Perspectives*, John Wiley and Sons, Chichester, 1996.

[6] I. J. Lowe, *Physical Review Letters*, 1959, **2**, 285–287.

[7] E. R. Andrew, A. Bradbury and R. G. Eades, *Nature*, 1958, **182**, 1659–1659.

[8] D. C. Apperley, R. K. Harris and P. Hodgkinson, *Solid-State NMR: Basic Principles and Practice*, Momentum Press LLC, New York, 2012.

[9] M. J. Duer, *Introduction to Solid-State NMR Spectroscopy*, Blackwell Publishing Ltd., Oxford, 2004.

[10] M. H. Levitt, *Spin Dynamics*, John Wiley and Sons Ltd., Chichester, 2nd edn., 2008.

[11] M. Bak, J. T. Rasmussen and N. C. Nielsen, *Journal of Magnetic Resonance*, 2000, **147**, 296–330.

[12] M. M. Maricq and J. S. Waugh, *Journal of Chemical Physics*, 1979, **70**, 3300–3316.

[13] A. Boeckmann, M. Ernst and B. H. Meier, *Journal of Magnetic Resonance*, 2015, **253**, 71–79.

[14] M. Ernst, A. Samoson and B. H. Meier, *Chemical Physics Letters*, 2001, **348**, 293–302.

[15] A. E. Bennett, C. M. Rienstra, M. Auger, K. V. Lakshmi and R. G. Griffin, *Journal of Chemical Physics*, 1995, **103**, 6951–6958.

[16] B. M. Fung, A. K. Khitrin and K. Ermolaev, *Journal of Magnetic Resonance*, 2000, **142**, 97–101.

[17] R. S. Thakur, N. D. Kurur and P. K. Madhu, *Chemical Physics Letters*, 2006, **426**, 459–463.

[18] M. Lee and W. I. Goldburg, *Physical Review*, 1965, **140**, 1261–1271.

[19] A. Bielecki, A. C. Kolbert and M. H. Levitt, *Chemical Physics Letters*, 1989, **155**, 341–346.

[20] E. Vinogradov, P. K. Madhu and S. Vega, *Chemical Physics Letters*, 1999, **314**, 443–450.

[21] E. Vinogradov, P. K. Madhu and S. Vega, *Journal of Chemical Physics*, 2001, **115**, 8983–9000.

[22] M. Leskes, S. Steuernagel, D. Schneider, P. K. Madhu and S. Vega, *Chemical Physics Letters*, 2008, **466**, 95–99.

[23] M. Leskes, P. K. Madhu and S. Vega, *Journal of Magnetic Resonance*, 2009, **199**, 208–213.

[24] M. E. Halse and L. Emsley, *Physical Chemistry Chemical Physics*, 2012, **14**, 9121–9130.

[25] D. Sakellariou, A. Lesage, P. Hodgkinson and L. Emsley, *Chemical Physics Letters*, 2000, **319**, 253–260.

[26] A. Lesage, D. Sakellariou, S. Hediger, B. Elena, P. Charmont, S. Steuernagel and L. Emsley, *Journal of Magnetic Resonance*, 2003, **163**, 105–113.

[27] E. Salager, R. S. Stein, S. Steuernagel, A. Lesage, B. Elena and L. Emsley, *Chemical Physics Letters*, 2009, **469**, 336–341.

[28] B. Elena, G. de Paepe and L. Emsley, *Chemical Physics Letters*, 2004, **398**, 532–538.

[29] A. Pines, M. G. Gibby and J. S. Waugh, *Journal of Chemical Physics*, 1973, **59**, 569–590.

[30] S. R. Hartmann and E. L. Hahn, *Physical Review*, 1962, **128**, 2042–2053.

[31] E. O. Stejskal, J. Schaefer and J. S. Waugh, *Journal of Magnetic Resonance*, 1977, **28**, 105–112.

[32] G. Metz, X. L. Wu and S. O. Smith, *Journal of Magnetic Resonance Series A*, 1994, **110**, 219–227.

[33] B. J. van Rossum, C. P. de Groot, V. Ladizhansky, S. Vega and H. J. M. de Groot, *Journal of the American Chemical Society*, 2000, **122**, 3465–3472.

[34] A. E. Bennett, C. M. Rienstra, J. M. Griffiths, W. G. Zhen, P. T. Lansbury and R. G. Griffin, *Journal of Chemical Physics*, 1998, **108**, 9463–9479.

[35] M. H. Levitt, *Encyclopedia of Nuclear Magnetic Resonance*, 2002, **9**, 165–196.

[36] A. Brinkmann, J. Gunne and M. H. Levitt, *Journal of Magnetic Resonance*, 2002, **156**, 79–96.

[37] H. K. Miah, D. A. Bennett, D. Iuga and J. J. Titman, *Journal of Magnetic Resonance*, 2013, **235**, 1–5.

[38] G. J. Hou, I. J. L. Byeon, J. Ahn, A. M. Gronenborn and T. Polenova, *Journal of Chemical Physics*, 2012, **137**, year.

[39] G. J. Hou, I. J. L. Byeon, J. Ahn, A. M. Gronenborn and T. Polenova, *Journal of the American Chemical Society*, 2011, **133**, 18646–18655.

[40] X. Zhao, W. Hoffbauer, J. Gunne and M. H. Levitt, *Solid State Nuclear Magnetic Resonance*, 2004, **26**, 57–64.

[41] S. Paul, R. S. Thakur, M. H. Levitt and P. K. Madhu, *Journal of Magnetic Resonance*, 2010, **205**, 269–275.

[42] S. Paul, R. S. Thakur, M. H. Levitt and P. K. Madhu, *Journal of Magnetic Resonance*, 2010, **205**, 269–275.

[43] T. Maly, G. T. Debelouchina, V. S. Bajaj, K. N. Hu, C. G. Joo, M. L. Mak-Jurkauskas, J. R. Sirigiri, P. C. A. van der Wel, J. Herzfeld, R. J. Temkin and R. G. Griffin, *Journal of Chemical Physics*, 2008, **128**, year.

[44] C. Sauvee, M. Rosay, G. Casano, F. Aussenac, R. T. Weber, O. Ouari and P. Tordo, *Angewandte Chemie-International Edition*, 2013, **52**, 10858–10861.

[45] M. Goldman and L. Shen, *Physical Review*, 1966, **144**, 321–331.

[46] J. Clauss, K. Schmidt-Rohr and H. W. Spiess, *Acta Polymerica*, 1993, **44**, 1–17.

[47] P. A. Mirau and S. Yang, *Chemistry of Materials*, 2002, **14**, 249–255.

[48] N. Egger, K. Schmidt-Rohr, B. Blumich, W. D. Domke and B. Stapp, *Journal of Applied Polymer Science*, 1992, **44**, 289–295.

[49] F. Mellinger, M. Wilhelm and H. W. Spiess, *Macromolecules*, 1999, **32**, 4686–4691.

[50] X. He, Y. Liu, R. Zhang, Q. Wu, T. Chen, P. Sun, X. Wang and G. Xue, *Journal of Physical Chemistry C*, 2014, **118**, 13285–13299.

[51] H. Yu, A. Natansohn, M. A. Singh and T. Plivelic, *Macromolecules*, 1999, **32**, 7562–7571.

[52] C. Neagu, J. E. Puskas, M. A. Singh and A. Natansohn, *Macromolecules*, 2000, **33**, 5976–5981.

[53] J. Wang, K. S. Jack and A. L. Natansohn, *Journal of Chemical Physics*, 1997, **107**, 1016–1020.

[54] K. S. Jack, J. Wang, A. Natansohn and R. A. Register, *Macromolecules*, 1998, **31**, 3282–3291.

[55] Z. Jia, L. Zhang, Q. Chen and E. W. Hansen, *Journal of Physical Chemistry A*, 2008, **112**, 1228–1233.

[56] F. Mellinger, M. Wilhelm, H. W. Spiess, R. Baumstark and A. Haunschild, *Macromolecular Chemistry and Physics*, 1999, **200**, 719–730.

[57] S. Spiegel, K. Schmidt-Rohr, C. Boeffel and H. W. Spiess, *Polymer*, 1993, **34**, 4566–4569.

[58] A. Buda, D. E. Demco, M. Bertmer, B. Blumich, B. Reining, H. Keul and H. Hocker, *Solid State Nuclear Magnetic Resonance*, 2003, **24**, 39–67.

[59] A. Buda, D. E. Demco, B. Blumich, V. M. Litvinov and J. P. Penning, *Chemphyschem*, 2004, **5**, 876–883.

[60] B. R. Cherry, C. H. Fujimoto, C. J. Cornelius and T. M. Alam, *Macromolecules*, 2005, **38**, 1201–1206.

[61] D. E. Demco, V. M. Litvinov, G. Rata, C. Popescu, K. H. Phan, A. Schmidt and B. Bluemich, *Macromolecular Chemistry and Physics*, 2007, **208**, 2085–2095.

[62] C. Melian, D. E. Demco, M. Istrate, A. Balaceanu, D. Moldovan, R. Fechete, C. Popescu and M. Moller, *Chemical Physics Letters*, 2009, **480**, 300–304.

[63] P. Caravatti, P. Neuenschwander and R. R. Ernst, *Macromolecules*, 1985, **18**, 119–122.

[64] J. Brus and J. Dybal, *Macromolecules*, 2002, **35**, 10038–10047.

[65] W. Fu, R. Zhang, B. Li and L. Chen, *Polymer*, 2013, **54**, 472–479.

[66] J. Brus, M. Urbanova and A. Strachota, *Macromolecules*, 2008, **41**, 372–386.

[67] J. Crank, *The Mathematics of Diffusion*, Oxford University Press, London, 2nd edn., 1975.

[68] J. Wang, *Journal of Chemical Physics*, 1996, **104**, 4850–4858.

[69] A. Buda, D. E. Demco, M. Bertmer, B. Blumich, V. M. Litvinov and J. P. Penning, *Journal of Physical Chemistry B*, 2003, **107**, 5357–5370.

[70] D. E. Demco, A. Johansson and J. Tegenfeldt, *Solid State Nuclear Magnetic Resonance*, 1995, **4**, 13–38.

[71] K. Schmidt-Rohr and H. W. Spiess, *Multidimensional Solid-State NMR and Polymers*, Academic Press Limited, London, 1994.

[72] A. M. Kenwright and B. J. Say, *Solid State Nuclear Magnetic Resonance*, 1996, **7**, 85–93.

[73] Q. Chen and K. Schmidt-Rohr, *Solid State Nuclear Magnetic Resonance*, 2006, **29**, 142–152.

[74] A. M. Kenwright and K. J. Packer, *Chemical Physics Letters*, 1990, **173**, 471–475.

[75] S. Friebel, R. K. Harris and A. M. Kenwright, *Magnetic Resonance in Chemistry*, 1997, **35**, 290–296.

[76] M. Mauri, Y. Thomann, H. Schneider and K. Saalwachter, *Solid State Nuclear Magnetic Resonance*, 2008, **34**, 125–141.

[77] X. Jia, J. Wolak, X. Wang and J. L. White, *Macromolecules*, 2003, **36**, 712–718.

[78] J. Jennings, M. Beija, A. P. Richez, S. D. Cooper, P. E. Mignot, K. J. Thurecht, K. S. Jack and S. M. Howdle, *Journal of the American Chemical Society*, 2012, **134**, 4772–4781.

[79] J. Jennings, M. Beija, J. T. Kennon, H. Willcock, R. K. O'Reilly, S. Rimmer and S. M. Howdle, *Macromolecules*, 2013, **46**, 6843–6851.

[80] J. Jennings, S. P. Bassett, D. Hermida-Merino, G. Portale, W. Bras, L. Knight, J. J. Titman, T. Higuchi, H. Jinnai and S. M. Howdle, *Polymer Chemistry*, 2016, **7**, 905–916.

[81] T. M. Werkhoven, F. M. Mulder, C. Zune, R. Jerome and H. J. M. de Groot, *Macromolecular Chemistry and Physics*, 2003, **204**, 46–51.

[82] Y. Zhang, K. K. Gangwani and R. M. Lemert, *Journal of Supercritical Fluids*, 1997, **11**, 115–134.

[83] Y. Shao *et al.*, *Physical Chemistry Chemical Physics*, 2006, **8**, 3172–3191.

[84] Y. Nishiyama, R. C. Zhang and A. Ramamoorthy, *Journal of Magnetic Resonance*, 2014, **243**, 25–32.

[85] P. A. Beckmann and C. Dybowski, *Journal of Magnetic Resonance*, 2000, **146**, 379–380.

[86] A. Bielecki and D. P. Burum, *Journal of Magnetic Resonance Series A*, 1995, **116**, 215–220.

[87] G. Neue and C. Dybowski, *Solid State Nuclear Magnetic Resonance*, 1997, **7**, 333–336.

[88] T. Takahashi, H. Kawashima, H. Sugisawa and T. Baba, *Solid State Nuclear Magnetic Resonance*, 1999, **15**, 119–123.

[89] R. K. Harris, E. D. Becker, S. M. C. De Menezes, P. Granger, R. E. Hoffman and K. W. Zilm, *Solid State Nuclear Magnetic Resonance*, 2008, **33**, 41–56.

[90] G. Neue, C. Dybowski, M. L. Smith, M. A. Hepp and D. L. Perry, *Solid State Nuclear Magnetic Resonance*, 1996, **6**, 241–250.

[91] A. Abragam, *The Principles of Nuclear Magnetism*, Oxford University Press, Oxford, 1961.

[92] J. H. van Vleck, *Physical Review*, 1948, **74**, 1168–1183.

[93] N. Pislewski, J. Tritt-Goc and R. Jakubus, *Solid State Nuclear Magnetic Resonance*, 1994, **3**, 293–297.

[94] G. Kim, F. Blanc, Y.-Y. Hu and C. P. Grey, *The Journal of Physical Chemistry C*, 2013, **117**, 6504–6515.

[95] A. Planell, J, M. Best, S, D. Lacroix and A. Merolli, *Bone Repair Biomaterials*, Woodhead Publishing Ltd., Cambridge, 2009.

[96] Y. Wang, S. Von Euw, F. M. Fernandes, S. Cassaignon, M. Selmane, G. Laurent, G. Pehau-Arnaudet, C. Coelho, L. Bonhomme-Coury, M. M. Giraud-Guille, F. Babonneau, T. Azais and N. Nassif, *Nature Materials*, 2013, **12**, 1144–1153.

[97] J. Kolmas and W. Kolodziejski, *Chemical Communications*, 2007, 4390–4392.

[98] A. Kaflak-Hachulska, A. Samoson and W. Kolodziejski, *Calcified Tissue International*, 2003, **73**, 476–486.

[99] S. Maltsev, M. J. Duer, R. C. Murray and C. Jaeger, *Journal of Materials Science*, 2007, **42**, 8804–8810.

[100] G. Y. Cho, Y. T. Wu and J. L. Ackerman, *Science*, 2003, **300**, 1123–1127.

[101] C. Jager, T. Welzel, W. Meyer-Zaika and M. Epple, *Magnetic Resonance in Chemistry*, 2006, **44**, 573–580.

[102] M. Ben Osman, S. Diallo-Garcia, V. Herledan, D. Brouri, T. Yoshioka, J. Kubo, Y. Millot and G. Costentin, *Journal of Physical Chemistry C*, 2015, **119**, 23008–23020.

[103] J. V. Bradley, L. N. Bridgland, D. E. Colyer, M. J. Duer, T. Friscic, J. R. Gallagher, D. G. Reid, J. N. Skepper and C. M. Trasler, *Chemistry of Materials*, 2010, **22**, 6109–6116.

[104] L. Pajchel and W. Kolodziejski, *Journal of Nanoparticle Research*, 2013, **15**, year.

[105] Y. Miyamoto, K. Ishikawa, M. Takechi, T. Toh, T. Yuasa, M. Nagayama and K. Suzuki, *Biomaterials*, 1998, **19**, 707–715.

[106] E. Lester, P. Blood, J. Denyer, D. Giddings, B. Azzopardi and M. Poliakoff, *Journal of Supercritical Fluids*, 2006, **37**, 209–214.

[107] T. Isobe, S. Nakamura, R. Nemoto, M. Senna and H. Sfihi, *Journal of Physical Chemistry B*, 2002, **106**, 5169–5176.

[108] J. P. Yesinowski and H. Eckert, *Journal of the American Chemical Society*, 1987, **109**, 6274–6282.

Appendix A

	T_1 - PS aromatic peak	T_1 - PS aliphatic peak	T_1 - PMMA methoxy peak	T_1 - PMMA methyl peak
1A	2.022 (±0.019)	1.784 (±0.033)	1.258 (±0.052)	1.165 (±0.057)
1B	1.826 (±0.029)	1.529 (±0.035)	1.101 (±0.037)	1.079 (±0.044)
1C	1.496 (±0.039)	1.243 (±0.027)	1.051 (±0.023)	1.073 (±0.033)
1D	1.506 (±0.042)	1.210 (±0.030)	1.076 (±0.026)	1.033 (±0.031)
1E	2.048 (±0.027)	1.736 (±0.049)	1.091 (±0.042)	1.130 (±0.054)
1F	1.957 (±0.027)	1.614 (±0.047)	1.089 (±0.037)	1.089 (±0.044)
1G	1.751 (±0.034)	1.462 (±0.036)	1.101 (±0.034)	1.066 (±0.047)
1H	1.303 (±0.041)	1.058 (±0.030)	0.929 (±0.020)	0.918 (±0.026)

Table A.1: Table showing the T_1 values obtained from saturation-recovery experiments of the different proton sites for the eight PMMA-b-PS polymers.

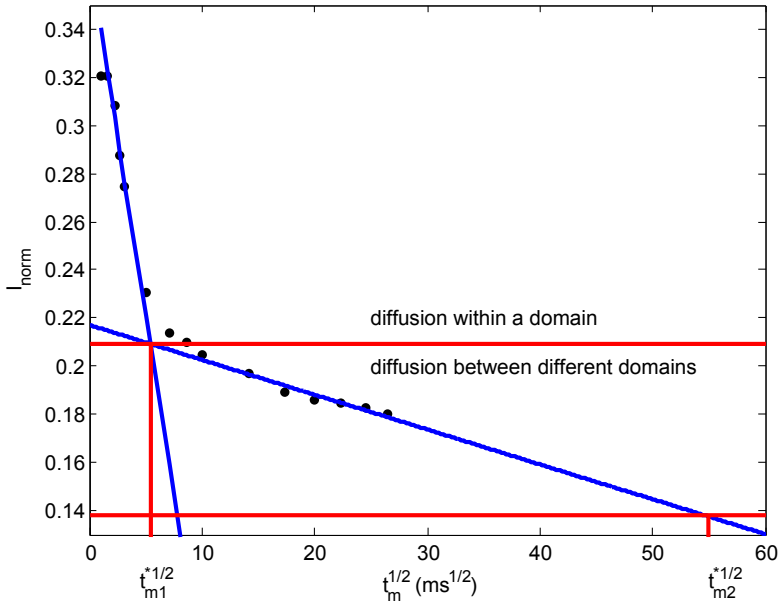


Figure A.1: Decay of intensity of the diagonal aromatic peak of sample 1A with increasing mixing time.

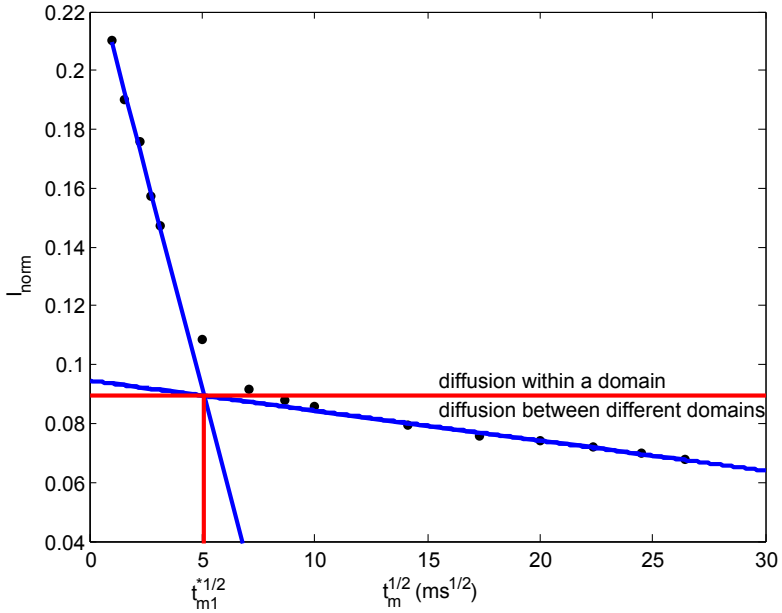


Figure A.2: Decay of intensity of the diagonal methoxy peak of sample 1A with increasing mixing time.

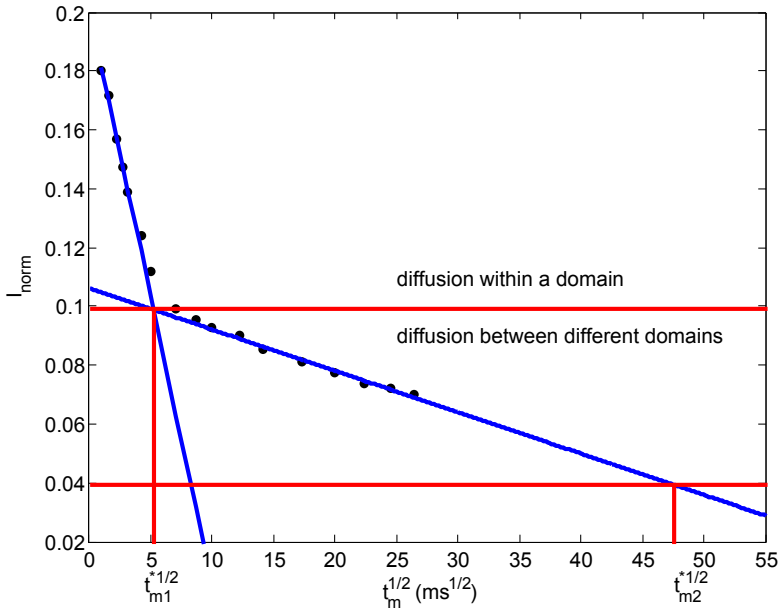


Figure A.3: Decay of intensity of the diagonal aromatic peak of sample 1C with increasing mixing time.

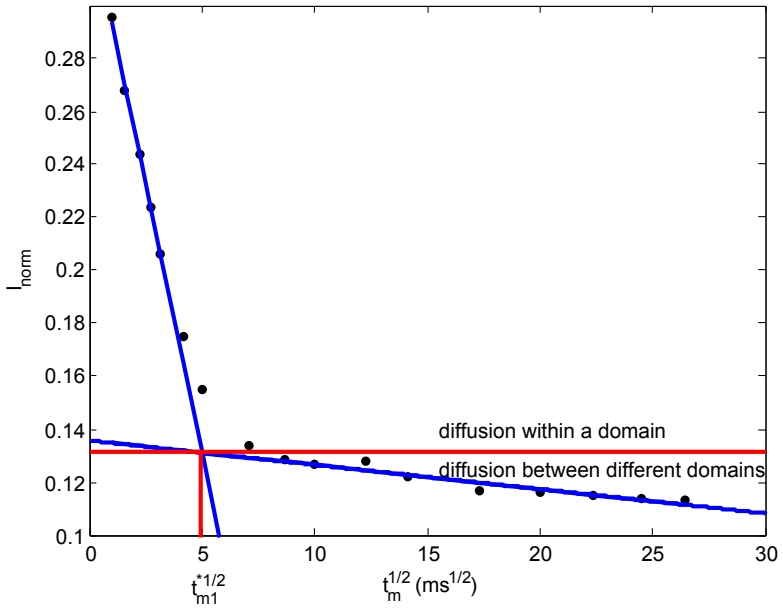


Figure A.4: Decay of intensity of the diagonal methoxy peak of sample 1C with increasing mixing time.

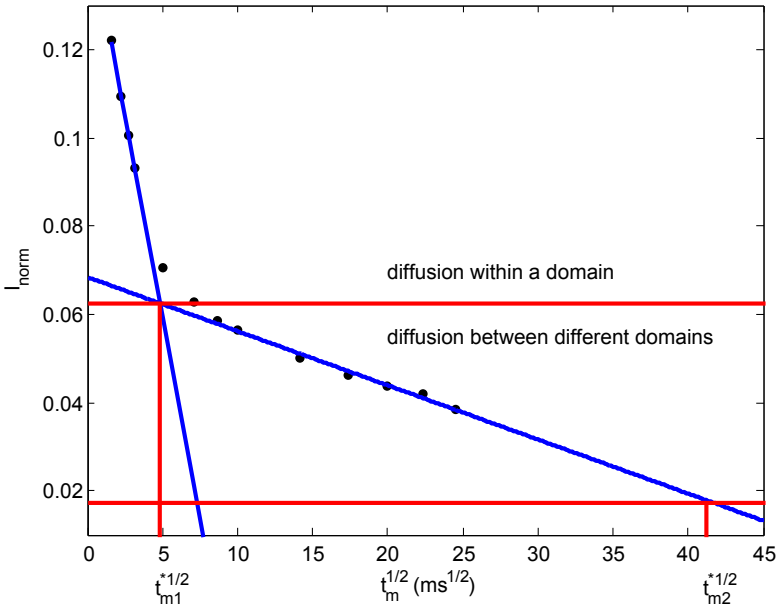


Figure A.5: Decay of intensity of the diagonal aromatic peak of sample 1D with increasing mixing time.

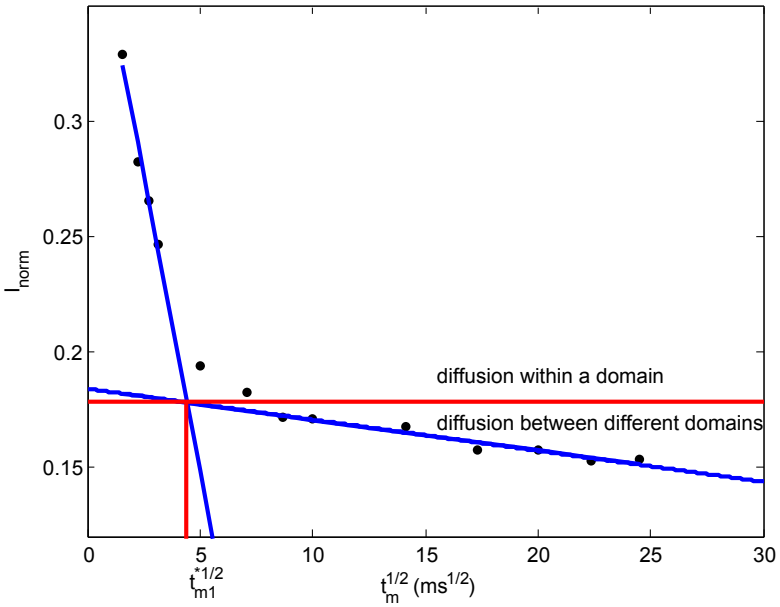


Figure A.6: Decay of intensity of the diagonal methoxy peak of sample 1D with increasing mixing time.

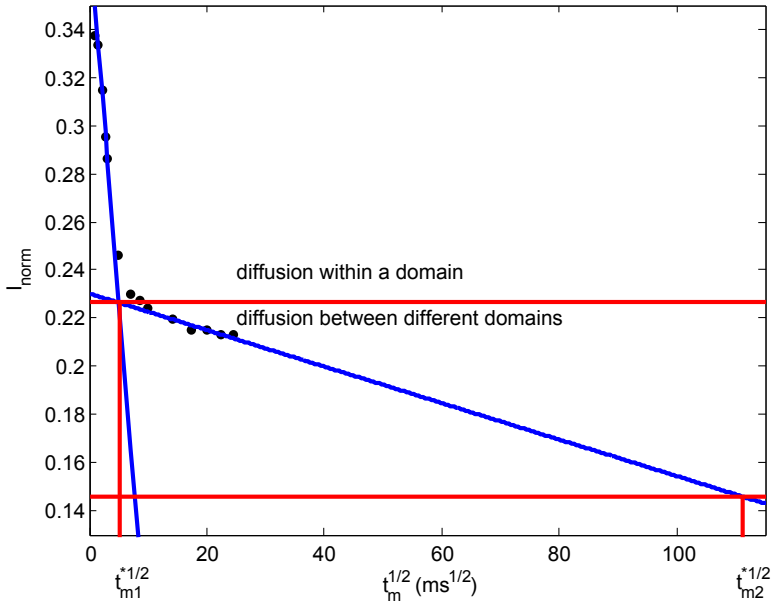


Figure A.7: Decay of intensity of the diagonal aromatic peak of sample 1E with increasing mixing time.

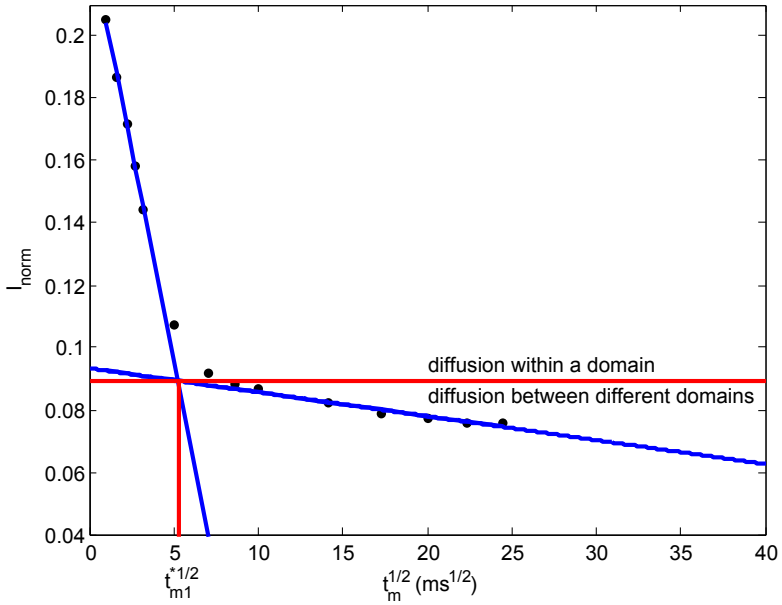


Figure A.8: Decay of intensity of the diagonal methoxy peak of sample 1E with increasing mixing time.

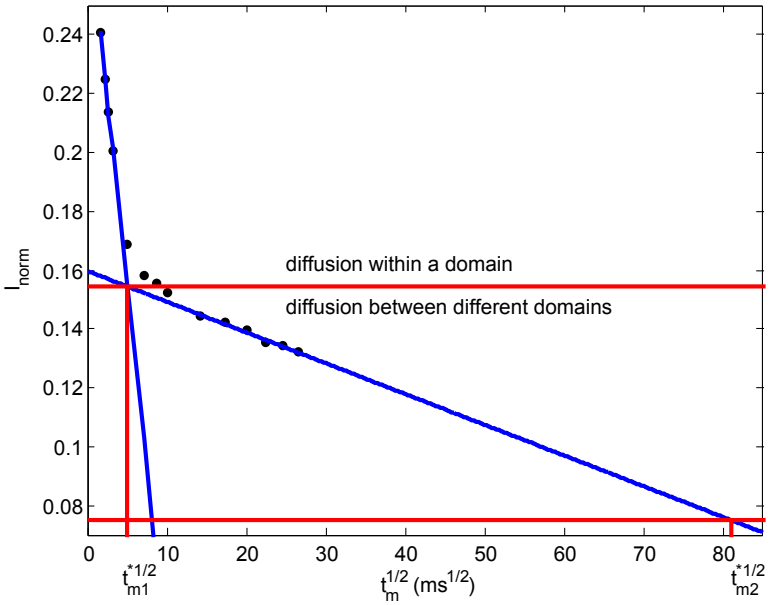


Figure A.9: Decay of intensity of the diagonal aromatic peak of sample 1F with increasing mixing time.

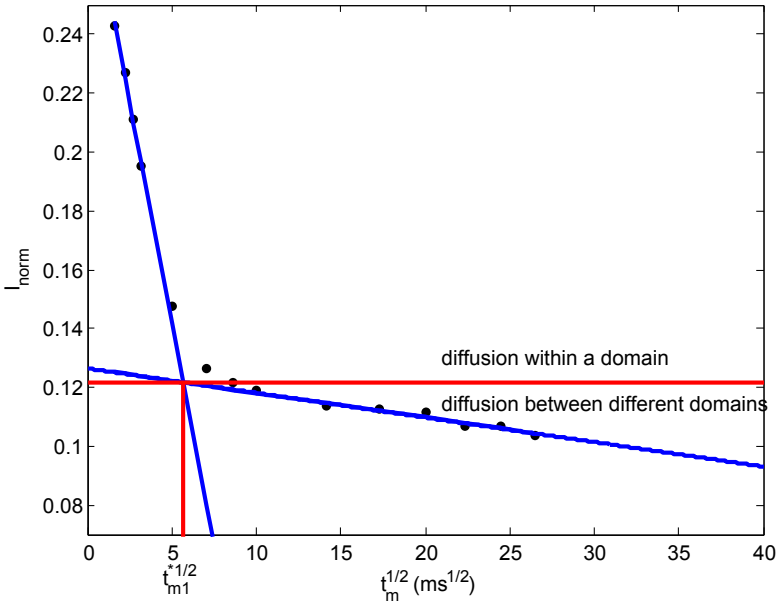


Figure A.10: Decay of intensity of the diagonal methoxy peak of sample 1F with increasing mixing time.

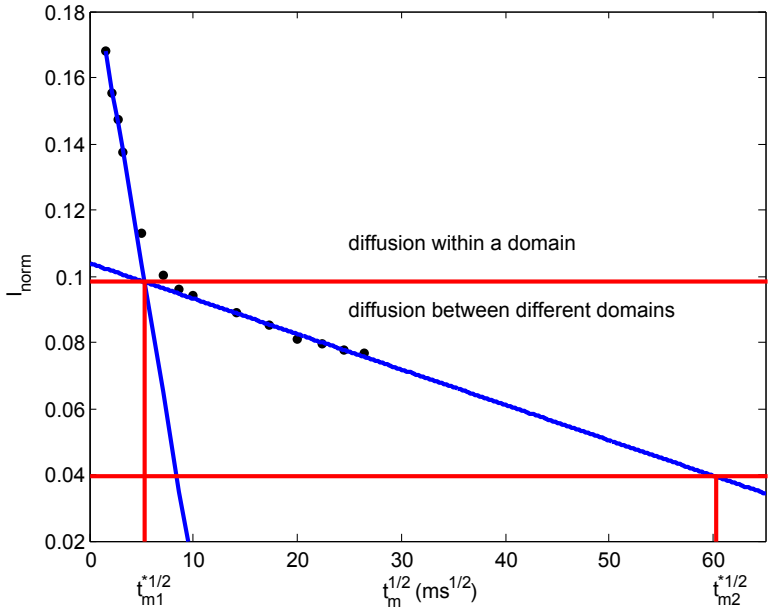


Figure A.11: Decay of intensity of the diagonal aromatic peak of sample 1G with increasing mixing time.

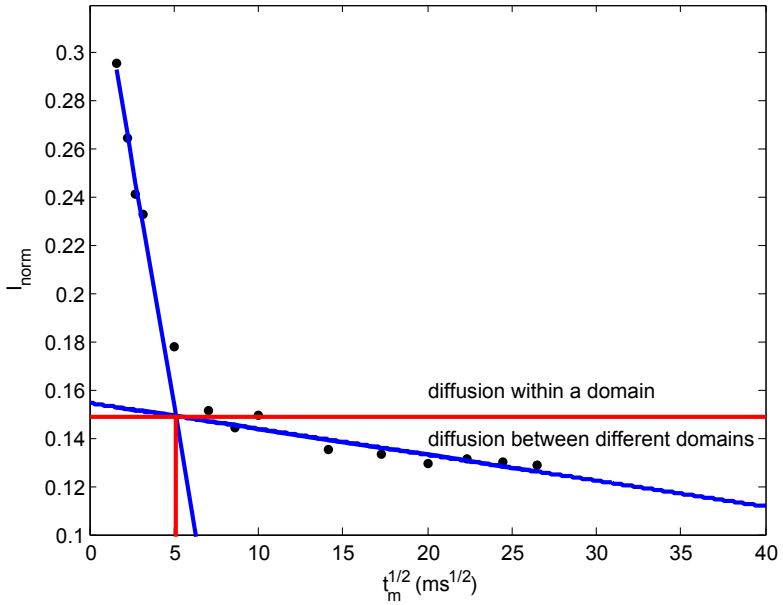


Figure A.12: Decay of intensity of the diagonal methoxy peak of sample 1G with increasing mixing time.

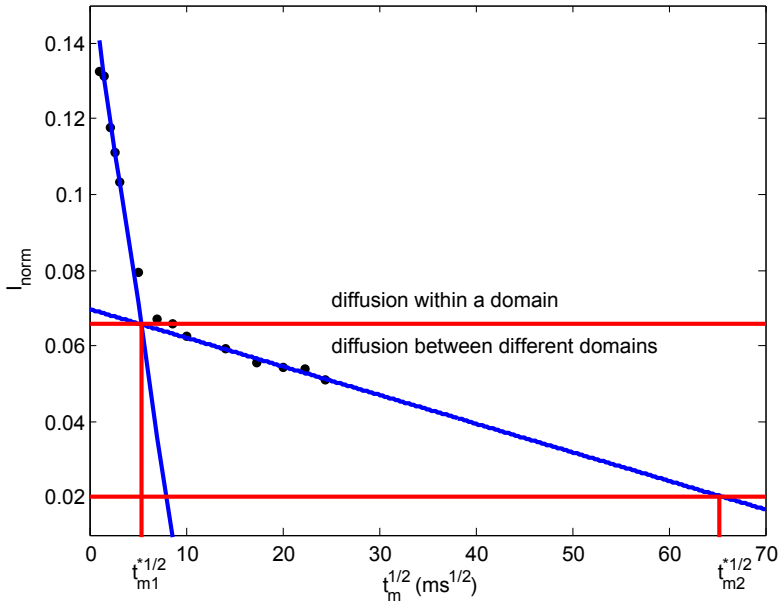


Figure A.13: Decay of intensity of the diagonal aromatic peak of sample 1H with increasing mixing time.

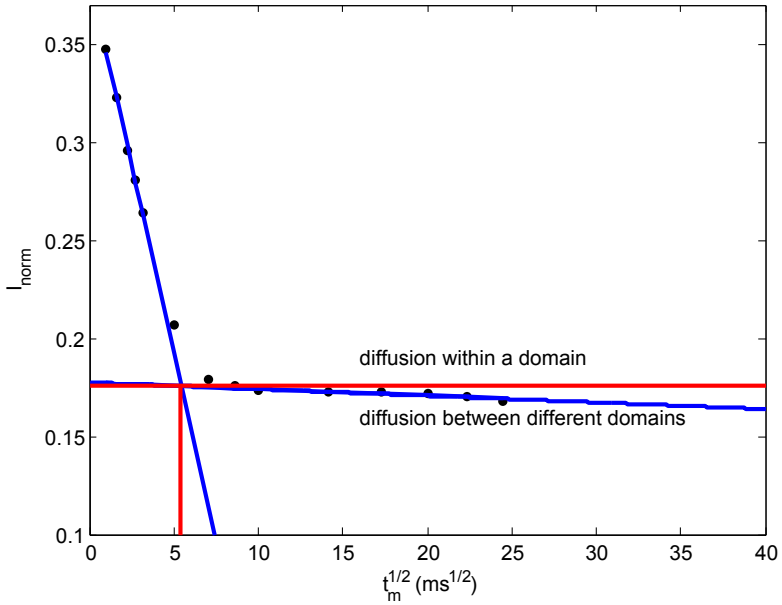


Figure A.14: Decay of intensity of the diagonal methoxy peak of sample 1H with increasing mixing time.

Appendix B

	T_1 - PBzMA aromatic peak	T_1 - methoxy peak	T_1 - aliphatic peak
2A	1.342 (± 0.029)	1.110 (± 0.031)	1.115 (± 0.042)
2B	1.262 (± 0.029)	1.083 (± 0.025)	1.085 (± 0.032)
2C	1.189 (± 0.039)	1.021 (± 0.022)	1.016 (± 0.027)
2D	1.349 (± 0.031)	1.083 (± 0.029)	1.118 (± 0.038)
2E	1.275 (± 0.053)	1.048 (± 0.023)	1.066 (± 0.036)

Table B.1: Table showing the T_1 values obtained from saturation-recovery experiments of the different proton sites for the five PBzMA-b-PMMA polymers

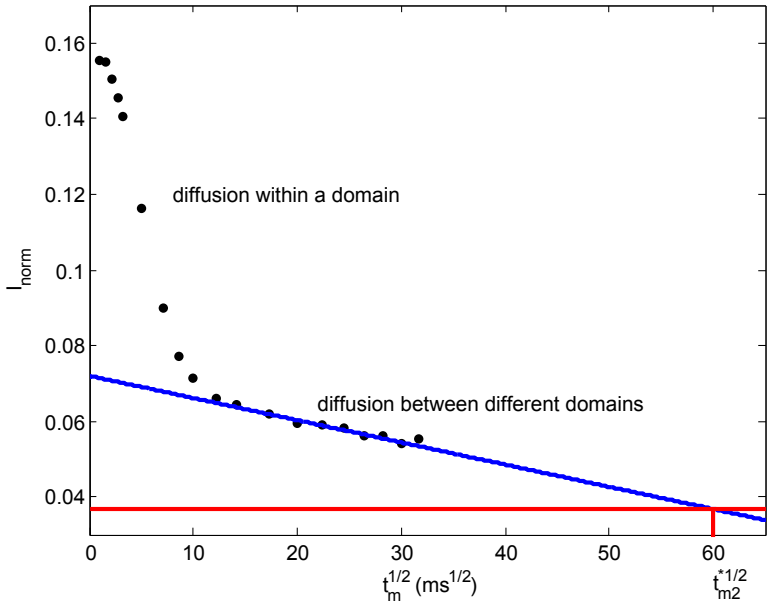


Figure B.1: Decay of intensity of the diagonal aromatic peak of sample 2A with increasing mixing time.

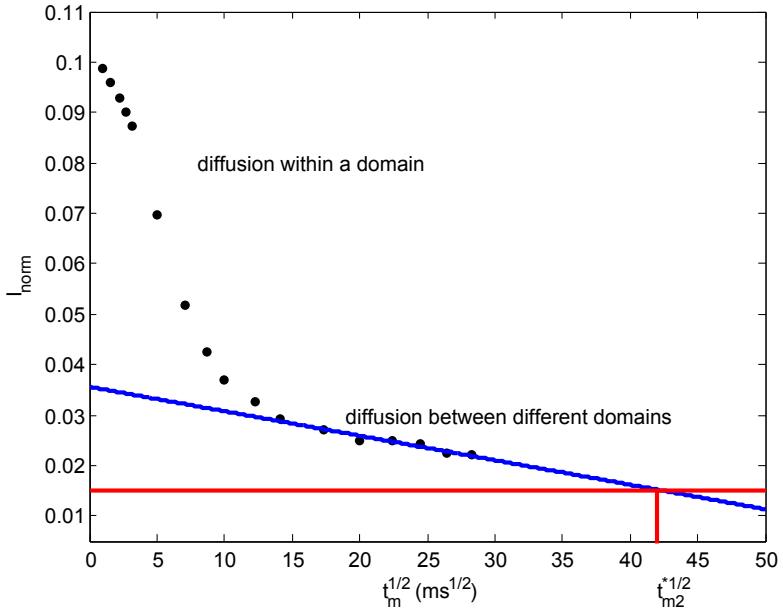


Figure B.2: Decay of intensity of the diagonal aromatic peak of sample 2C with increasing mixing time.

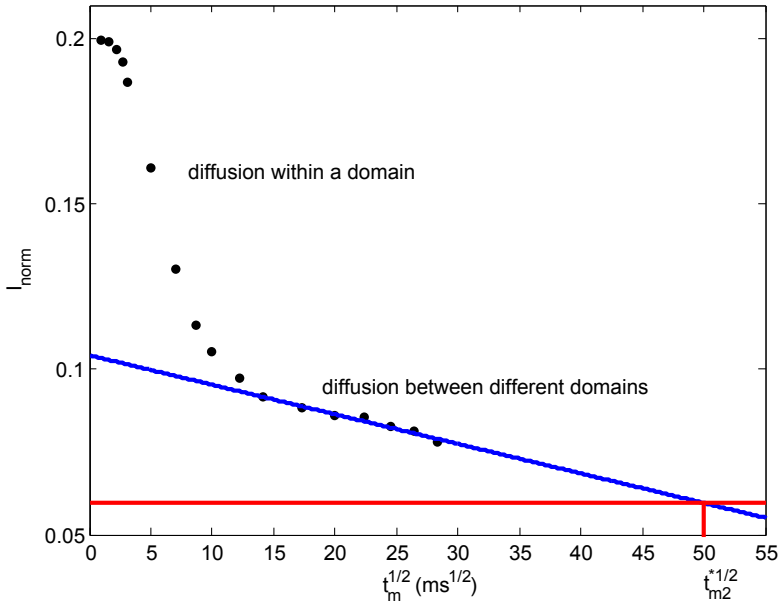


Figure B.3: Decay of intensity of the diagonal aromatic peak of sample 2D with increasing mixing time.

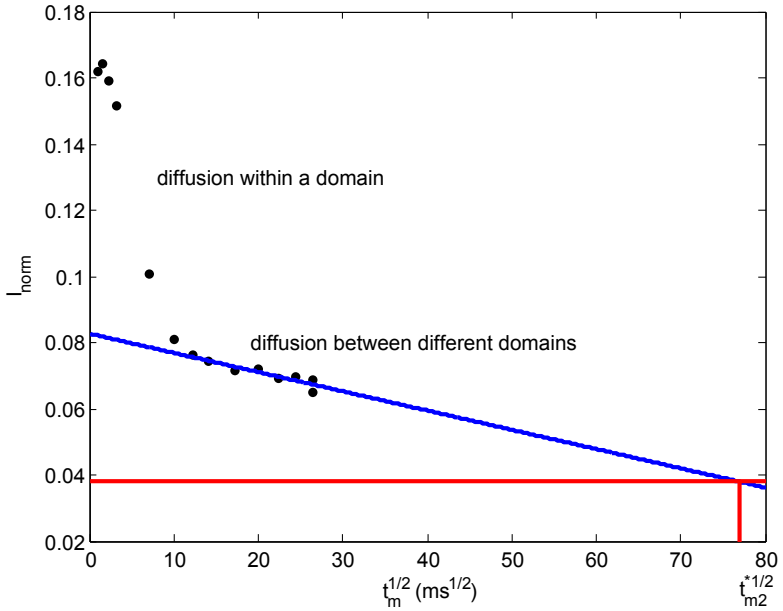


Figure B.4: Decay of intensity of the diagonal aromatic peak of sample 2E with increasing mixing time.